THE FLORIDA STATE UNIVERSITY

FAMU-FSU COLLEGE OF ENGINEERING

INVESTIGATION AND DEVELOPMENT OF THE RESIN INFUSION BETWEEN DOUBLE FLEXIBLE TOOLING (RIDFT) PROCESS FOR COMPOSITE FABRICATION

By

JAMES ROBERT THAGARD

A Dissertation submitted to the
Department of Industrial Engineering & Manufacturing Engineering
in partial fulfillment of the
requirements for the degree of
Doctor of Philosophy

Degree Awarded:
Fall Semester, 2003

The members of this Committee approve the thesis of James Robert Thagard defended on November 10, 2003.

Zhiyong Liang
Professor Directing Dissertation

Ching-Jen Chen
Outside Committee Member

Ben Wang
Committee Member

Chuck Zhang
Committee Member

James Simpson
Committee Member

Approved:

Ben Wang, Chair, Department of Industrial & Manufacturing Engineering

Ching-Jen Chen, Dean, College of Engineering

The Office of Graduate Studies has verified and approved the above named committee members.

ACKNOWLEDGEMENTS

I would like to acknowledge my wife Amy, daughter Kaylee and son Ethan for their love and continued support. I would also like to acknowledge my parents, Dr. and Mrs. Norman Thagard for their continual support throughout my pursuit for an advanced degree. I would like to thank the members of my Ph.D. dissertation committee, Zhiyong Liang, Ching-Jen Chen, Ben Wang, Chuck Zhang and James Simpson. Their guidance and support has helped me to achieve my dreams.

TABLE OF CONTENTS

LIST OF TABLES

LIST OF FIGURES

ABSTRACT

This research presents a study on an innovative composite manufacturing process called Resin Infusion between Double Flexible Tooling (RIDFT). In this process, resin is infused between two flexible tools through fiber reinforcements in a two-dimensional flat shape. The wetted reinforcements and flexible tooling are then formed over a mold into a specified part shape by use of vacuum. The RIDFT process has potentials for rapidly and affordably producing large composite parts. This research details the development of the industrial RIDFT machine from its design to its fabrication and to the demonstration of its use. This new machine uses new techniques, integrating vacuum sealing, dynamic supporting and temporary resin distribution channels to achieve industrial application requirements.

A design of experiment (DOE) approach is used to perform testing and analysis to validate the ability of the RIDFT process to form various geometries and identify limitations in formability and issues with wrinkling. Four specific fiber textile structures were studied in their ability to form over a half sphere of varying radii and a rectangular mold of varying corner radii. The number of fiber layers was also studied to understand the effects on forming. Fiber textile structure and fiber layers were shown to be significant for their influence on formability and wrinkling.

To better understand the forming mechanics within the RIDFT process and to predict the formability of a desired geometry, a simulation model was required. The PAMFORM software was chosen for modeling because it is a general-purpose finite element package for the industrial virtual manufacturing of non-metallic sheet forming. PAMFORM is unique in its ability to model a variety of forming processes.

This research details the development of the simulation model for the RIDFT process based on PAMFORM and describes the validation of the model through experimental methods. This development includes the modeling of multiple layers of resin-wetted reinforcements, silicone

diaphragms and part geometries, as well as the modeling of contact interfaces and forming pressures. The systematic investigation has been done for characterizing fabric drapability, rubber deformation and friction interactions for developing the simulation model. The model results are then compared against experimental results for model validation. This validated model will allow the ability to predict drapability and fiber deformation during the process forming. The results of the simulation reveal mechanisms and influence factors of the drapability and wrinkling of the RIDFT process.

CHAPTER 1

INTRODUCTION

1.1 Introduction

RIDFT is a new process that is a variation of resin infusion under flexible tooling (RIFT), flexible resin transfer molding (FRTM) and resin transfer molding (RTM). The main emphasis for the invention of RIDFT was to improve over RIFT and FRTM to produce parts cheaper and more quickly and to address environmental concerns with the manufacturing of composite parts. Problems such as tool wear, complex resin flow in processing, slow production rate, long process preparation time and applications of expensive preforms will be overcome and understood with the RIDFT process.

The RIDFT process can be divided into six steps as shown in Figure 1.1. In Step 1, the flat fiber layout is placed into the machine and positioned over the mold between the two highly deformable tooling layers. The frame is then sealed in Step 2 to ensure vacuum integrity between the two flexible layers forming a vacuum infusion bag. In Step 3 the fiber is completely vacuum infused with resin. The next step is to create the seal on the vacuum chamber by lowering the sealing frame onto the mold table to form the vacuum chamber. The next step is to apply vacuum to the chamber, thereby forming the shape of the part. The vacuum pulls the flexible tooling with the resin infused fiber around the mold surface. Once the resin has cured the final step is to remove the part from the RIDFT machine. It can be seen that the RIDFT process has both the advantages of resin infusion and diaphragm forming processes and has potential to realize efficient production of large component parts.

An initial RIDFT prototype was successfully constructed and validated for its ability to manufacture composite parts. Although the RIDFT prototype yielded good results, it is

necessary to show the ability to produce parts on a large scale. As a result, there is a need to design and construct a larger industrial RIDFT machine that is capable of manufacturing parts with dimensions of 5 feet wide x 10 feet length x 1 foot height. This new industrial RIDFT machine must be validated for its ability to produce parts on a large scale.

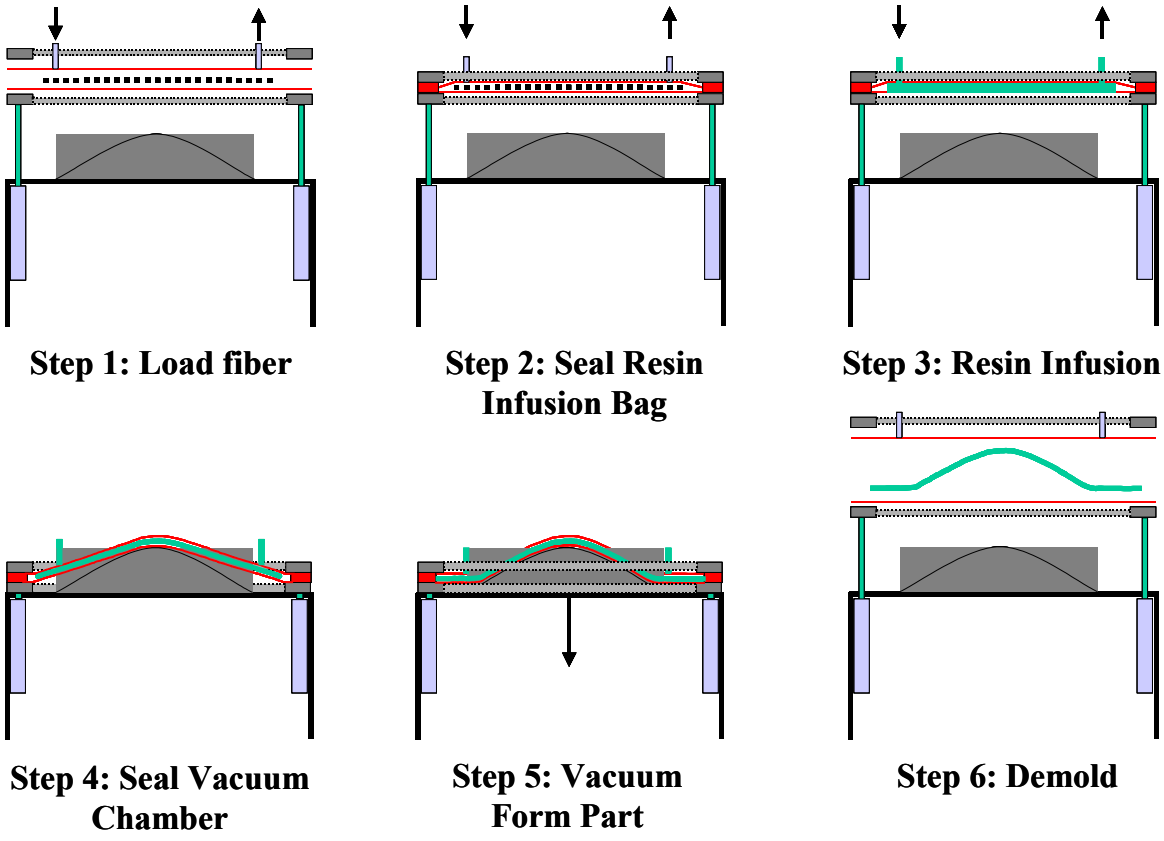

Figure 1.1 Schematic of the RIDFT Process

1.2 Problem Statement

A limitation of the developed RIDFT process is the formability of the fiber during forming. Resin is infused between two flexible tools through fiber reinforcements in a two-dimensional flat shape. The wetted reinforcements and flexible tooling are then formed over a mold into a

specified part shape by use of vacuum. Problems are created in the ability of the fiber to properly drape over shapes will dictate the part intricacies that can be formed. A necessity for the RIDFT process development is the ability to model and predict the forming mechanisms that occur.

It is important to characterize the drapability of different fibers over various shapes to understand the limitations of the RIDFT process. It is also necessary to understand the interaction of the fibers to flexible silicone tooling, fiber-to-fiber, flexible silicone tooling to tool and flexible silicone tooling to flexible silicone tooling during process forming. These interactions will affect the ability of the fiber to properly drape over various shapes and the quality of the final composite parts.

A designed experiment can be used to perform testing to validate the ability of the RIDFT process to form various geometries and identify limitations in formability and issues with wrinkling by using selected material systems. This information should also be used to help validate the simulation model to be developed.

To better understand and model the interactions within the RIDFT process a simulation model must be developed to help predict these interactions and their effects on formability, wrinkling, part thickness consistency, void content, fiber strain, and stress distributions and fiber orientation variation of the finished part. Following the development of the simulation model it should be validated against experimental results. Based upon the accomplishments of these efforts, we could more systematically understand and predict the RIDFT process and significantly enhance its applications.

1.3 Objective

This research addresses six primary tasks that include the following:

Task1: Industrial RIDFT machine

- Design of a larger industrial RIDFT machine
- Construction of a larger industrial RIDFT machine
- Demonstration of the larger industrial RIDFT machine

Task2: Modeling and simulation of RIDFT

- Review of resin infusion and diaphragm forming

- Governing phenomena and models
- Development of RIDFT modeling software
- Material Characterization

Task3: Design of Experiments (DOE) Investigation

- Identify geometries for formability and wrinkling
- Create experimental design
- Perform experiments
- Analyze experimental results

Task4: Demonstration of RIDFT simulation model

- 5 inch sphere case studies
- Mesh independence case studies
- Block case studies
- Update model parameters for improvements

CHAPTER 2

LITERATURE SURVEY

2.1 Introduction

A primary consideration in the development of composite production processes is cost. The marine industry manufacturers have stuck to the validated and cheaper open molding techniques of hand lay-up, even though the U.S. Environmental Protection Agency (EPA) has strict regulations and is forcing the industries to shift to closed mold techniques. The development of the Resin Infusion between Double Flexible Tooling (RIDFT) prototype further advances resin infusion technology and reduces the higher costs of closed mold techniques [1].

In recent years, investigation and development of new closed mold techniques to further reduce cost and VOC emissions were highlighted. For example, Summerscales [2] showed how the RIFT process would reduce worker contact with liquid resin while increasing component mechanical properties and fiber content by reducing total void compared to hand lay-up. Furthermore, RIFT offers the potential for reduced tooling costs where matched tooling (RTM or compression molding) is currently used [2].

As a variation of the RIFT process, RIDFT offers additional advantages. With the bottom flexible tooling surface, the cleanup and pre-manufacturing prep work is reduced. With RIDFT, resin contact with the mold surface does not occur and eliminates the need to prepare the mold before each cycle. In addition to reducing a manufacturing step, RIDFT does not lend itself to tool wear experienced from continuous use as seen in the RTM process. More important, RIDFT dies not need expensive preforms and handling complex resin flow problems in the RIDFT process.

With traditional RTM processes the problems of high tooling costs and long cycle times are of concern. The RTM process requires that two mold halves be used, which contributes to high

tooling costs. In comparison, the RIDFT process requires only one mold halve to be used during manufacturing.

2.2 Current Processes

Traditionally, RTM has been used as the choice for the manufacturing of composite parts. RTM offers many advantages over other processes for the manufacturing of fiber-reinforced thermosetting polymer composites. These advantages include better component thickness tolerances and surface finish, and reduced emissions of volatiles. However, tooling costs can be prohibitively large for parts of more than a few meters in dimension, particularly for one-off or small production runs [3]. Figure 2.1 illustrates a schematic of the RTM process.

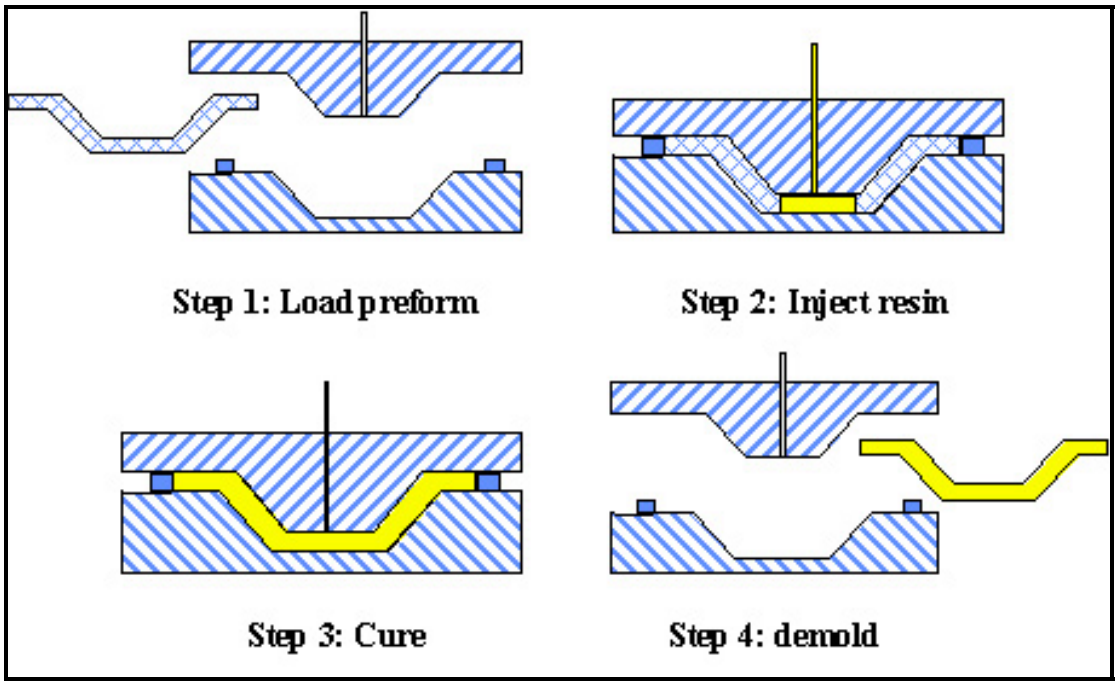

Figure 2.1 Schematic of the RTM Process

In order to further reduce the tooling costs, resin infusion under flexible tooling RIFT and Flexible Resin Transfer Molding (FRTM) were introduced in the 1980's as variations of the traditional RTM. A version of RIFT dates back to the 1950's when it was used in the production of boat hulls. Figure 2.2 illustrates the RIFT process developed by Ciba and Geigy [2]. A flexible female splash tool was the basis behind this process. During the 1980s, the use of a rubber bag as the flexible tool was investigated and several patents were filed [3]. The process was rediscovered during the 1990's and found applications particularly in the marine and automotive industries. A version of RIFT is used to strengthen offshore structures with carbon fiber [3].

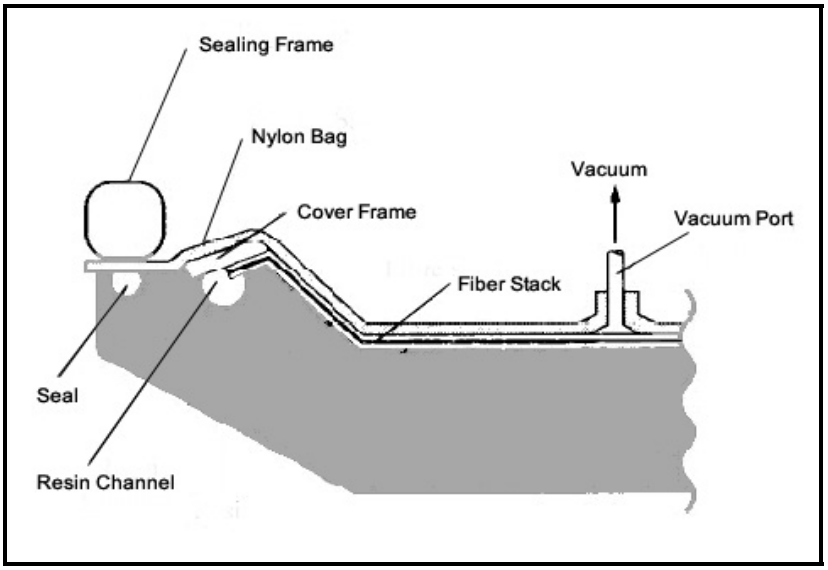

Figure 2.2 Schematic of the Ciba-Geigy RIFT Method [2]

RIFT retains many of the environmental advantages of RTM, but at a much lower tooling cost, since half of the conventional rigid closed mold is replaced by a bag. It may be feasible to adapt existing contact molds for the RIFT process. This becomes very important in mass production, as there is a potential for millions of dollars to be saved from reduced tooling and manufacturing costs.

RIFT has other advantages over the traditional RTM process. These advantages include [4]:

- Use of existing hand lay-up molds with only minor alterations
- Low investment in additional equipment
- Improved mechanical properties
- Ability to produce very large components

It has been noted that RIFT has some disadvantages over the RTM process. One disadvantage being there is no direct control over the thickness or fiber content of the final composite laminate in the RIFT process. These parameters depend on the compressibility and relaxation of the reinforcement under pressure, and interactions with bagging film breather and other ancillary materials [3].

The compressibility of dry fabrics was reviewed by Pearce and Summerscales [5]. They noted that the response of a dry preform was dynamic. Time dependent compression and relaxation were observed, and higher compaction at a given pressure was achieved by repeatedly loading and unloading the reinforcement. This repeatedly loading and unloading of the reinforcement is known as a debulking process. The compression of the reinforcement during RIFT is further complicated by the arrival of the flowing resin, providing lubrication for the fibers and may hence affect the deformation of the laminate under the vacuum bag. Furthermore, the effective compressive force acting on the reinforcement is not constant during the process.

Before the arrival of the resin at a given point, the dry laminate is subject to approximately atmospheric pressure. As the resin flows further past this point, the pressure in the resin rises, so the new compression on the reinforcement reduces. A theoretical and practical understanding of these compaction mechanisms is required in order to assess whether molded laminates can be produced with a consistent, reproducible and predictable fiber content and quality. There is also a need to quantify any interaction between the laminate and the ancillary materials during the process [3].

Flexible resin transfer molding (FRTM) is an innovative composite manufacturing process, developed based on detailed cost analysis, which is intended to be cost effective by design. FRTM is a hybrid process, which combines the technical characteristics and respective favorable economics of diaphragm forming and resin transfer molding. Separate sheets of dry fiber and solid resin are placed between elastomeric diaphragms and heated so that the resin liquefies. The

fiber and resin are then compacted by drawing a vacuum between the diaphragms, and formed to shape by drawing the diaphragm assembly over hard tooling [6]. Figure 2.3 illustrates s a schematic of the FRTM process [6]. The FRTM process was optimized to produce high quality parts with low thickness variation, low void content and high fiber volume. Finally, the cost effectiveness of the FRTM process was verified through a mini-production run [6].

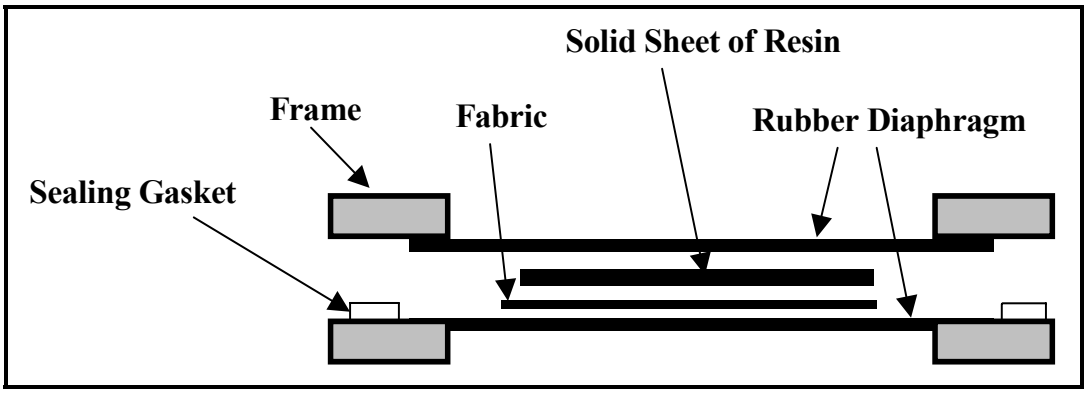

Figure 2.3 Schematic of the FRTM Process [6]

FRTM was designed and developed to allow for parts to be made cheaper and faster than traditional methods such as RTM. A need for new cost effective means of production is often a starting point for the development of a new process such as FRTM from the classical RTM process. The comparative advantages and disadvantages of the vacuum forming version of FRTM and several other currently available processes such as RIFT are shown in Table 2.1.

Conceptually, FRTM is a hybrid process, which combines favorable characteristics of RTM and forming. Like RTM, FRTM uses the lowest cost constitutive raw materials possible (dry fiber and resin), but eliminates the labor intensity typically associated with preparation of the three-dimensional fibrous preform used in RTM. In FRTM, fabric is formed in a one step double diaphragm forming process. This reduces labor intensity and decreases cycle time. FRTM can also reduce tooling costs typically associated with RTM because there is no requirement for heavy matched tooling [6].

Table 2.1 Process Comparison Chart [6]

Process	Advantages	Disadvantages
Hand Layup	Can Produce Complex Shapes Well Understood	Raw Material Expensive Extremely Labor Intensive Not Cost Effective at High Volumes
RTM	Uses Lowest Cost Raw Material Produce Complex/Highly Integrated Parts	Labor Intensive Preform Prep. Tooling Cost Typically High 3D Resin Flow Difficult to Control
Forming	Labor Cost is Reduced One-Step Bulk Deformation	Raw Material Cost Very High Geometry Complexity "Formable" Shapes
FRTM & RIFT	Uses Low Cost Raw Materials Less Labor Content, Bulk Deformation 2D Impregnation easier to control	Geometry Complexity "Formable" Shapes Potential for Thickness Variation Limits in Fiber Volumes Achievable.

The second advantage of the FRTM process arises from the fact that the diaphragm system is, by nature, deformable, and provides a low cost reconfigurable tooling surface. Through the use of various forming methods it is possible to reduce the tooling costs associated with dedicated matched tooling in the traditional RTM process. Reduced tooling costs can come from lighter weight tooling, one-sided tools, or through the economic advantages of a flexible, reconfigurable forming mechanism. FRTM also reduces or eliminates tool cleaning, typically a labor-intensive operation [6].

The third advantage of the FRTM process is that because resin impregnation occurs in the flat, the impregnation process is more repeatable, quicker, and more easily controlled. By impregnating in the flat, placement of sprues and vents is independent of final part geometry. The traditional costly experimentation necessary to optimize processing variables and redesign tooling to achieve void-free uniform wet-out is eliminated, and development time for new parts is greatly reduced since no new learning is required. Given that the resin begins in a position very close to its final location, the process is inherently quicker and more controllable than the complicated flow pattern associated with RTM [6].

Table 2.1 shows the disadvantages of the FRTM process. Many forming processes have limitations in the geometries that can be formed. Undercuts are features that cannot be produced with the vacuum forming mechanism. There are potential limits in the control of thickness variation and in the fiber volumes achievable with the FRTM process. Control of thickness

variation was optimized through the use of close loop process control and through judicious selection of resins whose properties were best suited for the unique requirements of the FRTM process. Fiber volume is closely related to the compaction pressure applied to the fabric during cure and therefore, varies depending on the forming method employed [6].

2.3 Resin Infusion Between Double Flexible Tooling (RIDFT)

As previously mentioned, the RIDFT process can be divided into six steps as illustrated in Figure 1. In step 1 the fiber is placed into the machine and positioned over the mold between two flexible tooling layers. The frame is then sealed in step 2 to ensure vacuum integrity between the flexible layers. In step 3 the fiber is completely vacuum infused with resin. The next step is to create the seal on the vacuum chamber between the flexible tooling, impregnated fabric layers and the mold by lowering the sealing frame onto the mold table. The next step is to apply vacuum to the chamber, thereby forming the shape of the part. The vacuum pulls the flexible tooling with the infused fiber tightly against the mold surface. Once the resin has cured the final step is to remove the part from the RIDFT machine.

RIDFT intends to solve problems associated with RIFT and FRTM. These problems include manufacturing cycle time, process complexity and associated costs. Although not all problems have been currently addressed, it is the intent of this research to use RIDFT to overcome the shortcomings and limitations of RIFT and FRTM. Unlike the FRTM process, the RIDFT process does not use dry solid sheets of resin, but uses a room temperature thermoset. This does not require the use of heat lamps or ovens in order to cure the resin as in the FRTM process. The room temperature thermosets can vary hardener content to allow for partial curing within 10 minutes of completed infusion and allows for the partially cured part to be removed.

FRTM is limited in the fiber volumes achievable. RIDFT does not use dry sheets of resin and because low viscosity resin is infused through the fibers it is hoped this will allow for much higher fiber volume fractions. Other advantages of the RIDFT process are that the flow of resin is two-dimensional, without the complexity of a three-dimensional flow front as experienced with RTM.

2.4 Resin Infusion and Darcy's Law

The initial step for the RIDFT process is the infusion of resin through a two-dimensional flow front. Resin is vacuum infused between two layers of flexible tooling in a flat position. It is important to understand this step, as the infusion of resin into the fiber will determine the capability of the system and the characteristics of the finished part. The resin flow rate, j_r, depends on the gradient of the hydrostatic pressure, ∇P, in the resin and it can be written according to Darcy's law as follows in Equation 2.1 [7]:

$$j_r = \frac{-D}{\eta} \nabla P \qquad \text{Equation (2.1)}$$

where,

D = permeability of the preform and η is the viscosity of the resin.

The permeability of the matrix material can generally change during the vacuum infusion process. It is has been proposed that permeability is not constant but can be defined as a product $D = D_i D_r$, where D_i is the intrinsic permeability and D_r the relative permeability, which varies from 0 to 1, depending on the preform's saturation [7]. However, the RIDFT process is pressure driven so as not to assume varying fiber permeability.

2.4.1 One-Dimensional (1-D) Darcy's Law

For a finite 1-D flow, as shown in Figure 2.4, Darcy's Law can be stated as follows in Equation 2.2 [8]:

$$Q = A \times K \times \Delta h \times L^{-1} \qquad \text{Equation (2.2)}$$

where,

Q = volumetric flow rate (m^3/s or ft^3/s),

A = flow area perpendicular to L (m^2 or ft^2),

K = hydraulic conductivity (m/s or ft/s),

L = flow path length (m or ft),

h = hydraulic head (m or ft) and

D = denotes the change in h over the path L.

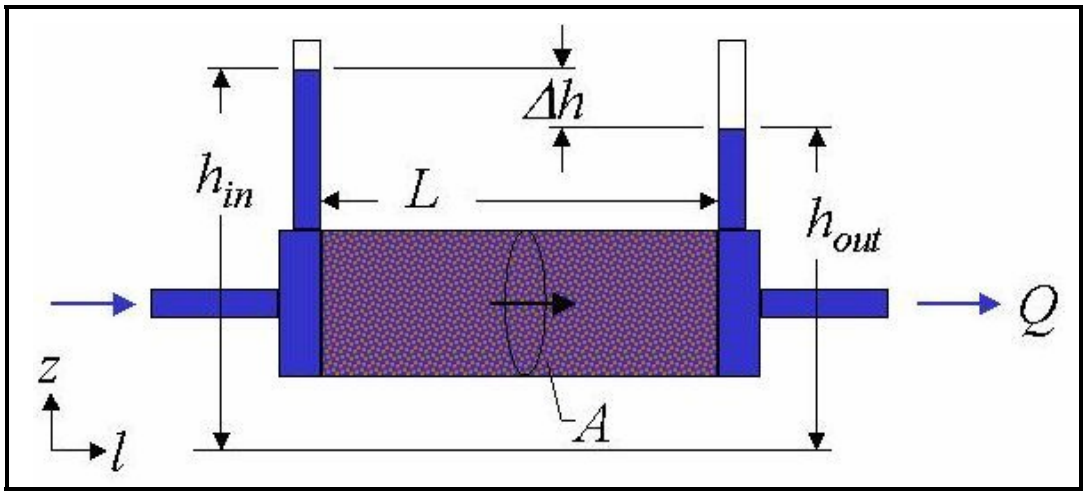

Figure 2.4 1-D Illustration of Darcy's Law [8]

When the fluid is other than water at standard conditions, the conductivity is replaced by the permeability of the media. The two properties are related as follows in Equation 2.3 [8]:

$K = k\rho g / \mu = kg / \nu$ Equation (2.3)

where,

k = permeability, (m^2 or ft^2),

μ = fluid absolute viscosity, (N s/m^2 or lb s/ft^2) and

ν = fluid kinematic viscosity, (m^2/s or ft^2/s).

This understanding of the forces that affect the infusion of resin into fiber during infusion is the basis for 2D flow front models that have previously been developed. These models are used to quantitatively analyze the influences of permeability, viscosity and vacuum degree on filling time for a flat part. For a finite 1-D flow, as the length, L, increases the volumetric flow rate of the resin decreases [8]. According to Darcy's Law, if you want to increase the resin flow rate, one can decrease the viscosity of the resin or increase the permeability of the fiber system.

The current resin system used in the RIDFT process is a vinyl ester resin with a viscosity of approximately 150cps. This is a very low viscosity resin while at room temperature, 22°C and has the desired viscosity necessary for vacuum infusion. There is the ability to further reduce the viscosity of the resin by heating it up in the range of 100°C. However, if the resin is kept at 22°C, the other alternative to increasing flow would be to increase the permeability.

There are several ways to increase the permeability of the fiber system through the addition of permeable layers, distribution channels or with various high-permeable fiber alternatives. Proper fiber selection can increase the resin flow rate by choosing a fiber that is less dense and of various fiber orientations.

Flow mediums provide a high-permeability layer for the distribution of resin within a low-permeability fiber system. The contribution of the flow in the high-permeable medium to the resin infusion into the fiber preform has been studied [9]. It was found that the high-permeable medium played an important role in determining the mold filling time. A peel ply lay between the high-permeable medium and the fiber perform cannot only help de-molding, but also speed up mold filling. A 3D finite element model was applied to simulate the mold filling process, which elucidates the influences of the flow properties of the high-permeable medium, the fiber perform and the peel ply on the mold filling time. The simulation results indicate that mold filling time is a strong function of the permeability of the high-permeable medium, but is not sensitive to the permeability of the fiber perform [9].

Fibers can also play an important role in addressing the issue of adequate resin flow through the enclosure. The density of the fiber preform will have a direct relationship to the permeability of the fiber when comparing like fibers. Therefore, to increase fiber permeability one can choose a fiber preform with a lower density. However, lower density preforms affect the fiber volume, V_f, of the finished part by reducing V_f.

2.4.2 Applying One-Dimensional (1-D) Darcy's Law

Using the unidirectional (1-D) flow modeling in this report will quantitatively analyze the influences of permeability, viscosity and vacuum degree on filling time for a flat part. The part dimensions are 10ft x 5ft x 0.5in with the injection port along the 5ft edge. The equation for 1-D flow will be used as follows to account for permeability, pressure gradient and resin viscosity changes as follows in Equation 2.4:

$$v = \frac{-k' * \Delta P}{\eta * L} \qquad \text{Equation (2.4)}$$

where,

v = flow rate (meter/second),

$-k'$ = fiber permeability (meter^2),

ΔP = hydrostatic pressure difference (Newton/meter^2),

L = flow path length (meter) and

η = resin viscosity (Newton*second/meter^2).

To determine flow time the equation for flow rate, v, must be integrated with respect to time. The equation can be integrated as follows in Equation 2.5:

$$v = \frac{k' * \Delta P}{\eta * L} \Rightarrow \frac{dx}{dt} = \frac{k'*\Delta P}{\eta * x} \Rightarrow T = \int dt = \frac{\eta}{k'*\Delta P}\int_0^L L\, dL = \frac{\eta}{k'*\Delta P}\left[\frac{L^2}{2}\right]_0^L \qquad \text{Equation (2.5)}$$

$$Filling\ Time = \left[\frac{\eta * L^2}{k'*\Delta P * 2}\right]$$

2.4.3 Results of Permeability, Viscosity and Vacuum Degree on Fill Time

To show the effects of permeability, viscosity and vacuum degree on filling time, the ranges for these were given low, medium and high values. Table 2.2 lists the values used to show effects on fill times. From the low, medium and high value listed in Table 2.2, the influences of permeability, viscosity and vacuum degree on the filling time is obtained. Table 2.3 shows the effects of fiber permeability, resin viscosity and vacuum degree on fill time.

Table 2.2 Values for Variation in Fill Times

	Low Value	Med Value	High Value
v = flow rate (m/s)			
A = flow area perpendicular to L (m^2),	0.0194	0.0194	0.0194
dP = hydrostatic pressure difference (N/m^2),	34473.0000	68947.0000	101358.0000
L = flow path length (m),	3.0480	3.0480	3.0480
η = viscosity (N*s/m^2),	0.1000	0.1500	0.2000
k' = fiber permeability (m^2),	1.00E-09	3.00E-09	6.00E-09

Table 2.3 Effects Variation on Fill Times

	Low Value	Med Value	High Value
permeability effects on filling time (hrs)	3.74	1.25	0.62
viscosity effects on filling time (hrs)	3.74	5.61	7.49
vacuum degree effects on filling time (hrs)	3.74	1.87	1.27

From results listed in Table 2.3, it is seen that, as the permeability is changed from 1.00E-09 m^2 to 6.00E-09 m^2, the resulting fill time is lowered from 3.74 hrs to 0.62 hrs respectively. This result is expected as increasing the permeability for a given resin viscosity allows the resin to flow more easily through the fiber. Changing the viscosity from 100 cps to 200 cps has increased fill times from 3.74 hours to 7.49 hours respectively. This result is also expected as the increase in resin viscosity makes it more difficult for the resin to flow through the fiber, thereby increasing fill times. Lastly, increasing the vacuum degree from 34,473 Pa to 101,358 Pa has decreased fill times from 3.74 hours to 1.27 hours respectively. This result is expected because decreasing the infusion pressure will not allow the resin to flow as quickly, thereby decreasing fill times.

2.5 Forming Modeling

The RIDFT diaphragm system is complicated and requires the drapability of resin infused fiber, flexible tooling and their interactions to be simultaneously modeled for forming simulation. Rozant *et al.* [10] reported that studies have been conducted to investigate the drapability of dry textile fabrics. These studies on drapability tests were performed on several woven and knitted fabrics in order to relate the forming energy to the preform architecture [10]. This investigation is important as it provides a baseline for the evaluation of the drapability of dry fibers.

In the RIDFT process, a more complex problem results due to the dynamics of the system with fiber being draped after being infused with resin. Additionally, the infused fiber is formed while placed between two layers of flexible tooling. This diaphragm forming system requires the fiber-resin interactions, flexible tooling-mold interactions, fiber-flexible tooling interactions and resin-flexible tooling interactions be understood in order for a formal model of the RIDFT process to be developed. Furthermore, investigations of resin flow are necessary for improved part quality for the manufacturing of large-scale components.

2.5.1 Drapability of Dry Fiber

The ability of a dry fiber to drape over a given object is determined by several basic factors. The fibers tensile properties will determine the ability of the fiber to stretch over a particular part when a given force is applied. In the case of RIDFT, the flexible diaphragms are used to force

the fiber over the mold surface. Another important aspect of the dry fiber is its response to shearing forces. Shearing forces will decrease the angle between woven fibers until it reaches a critical point called the locking angle. By definition, the locking angle is the smallest angle reached between two adjacent yarns before the onset of buckling [10]. Figure 2.5 illustrates how shearing of the woven fiber affects the angle and wrinkling of the weaves.

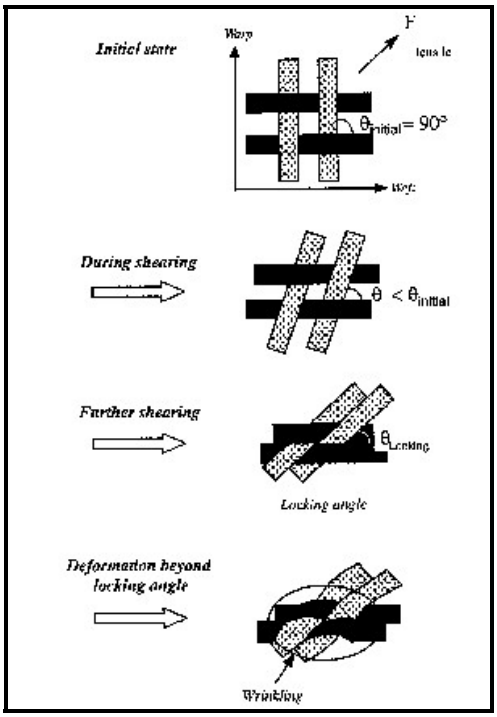

Figure 2.5 Occurrence of Wrinkling During the Shearing of Weaves [10]

It is possible to determine experimentally the locking angle, θ_L. Since the initial angle θ_i is equal to $\pi/2$. This is shown as follows in Equation 2.6 [10]:

$$\theta_L = \theta_i - 2\left[\frac{\pi}{4} - \cos^{-1}\left(\frac{\sqrt{2}\in_L + \sqrt{2}}{2}\right)\right] \qquad \text{Equation (2.6)}$$

where,

$\in_L$ = measured strain in the loading direction at the corresponding locking angle.

Another factor affecting a fiber's ability to drape is the fiber architecture. In the composite field, the two dominant textile fabrics are woven and knitted structures. The fundamental difference between woven fabrics and knitted fabrics is in the way the fibers are interconnected. While woven fabrics are produced by the weaving of straight fibers, knitted fabrics have a structure formed by the intermeshing of yarn loops. Two types of knitted structures can be found: warp knitted and weft-knitted fabrics [10]. Figure 2.6 illustrates the different types of fiber architectures.

The knitted fibers allow for lower locking angles to occur before wrinkling is initiated. This ability of knitted fibers makes them more advantageous for draping over complex shapes. It is important to quantify the ability of the fiber's architecture to drape over various shapes, however, this quantification is for comparative purposes only.

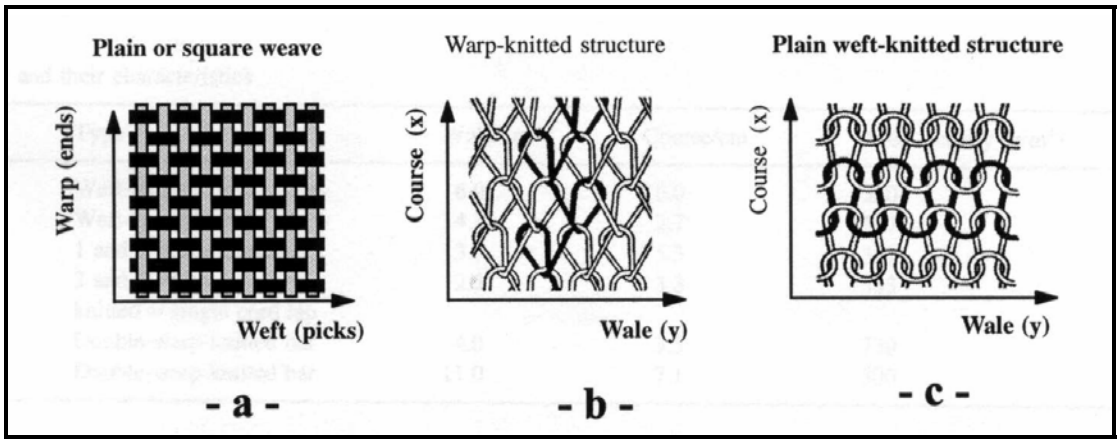

Figure 2.6 Fabric Architecture: (a) Plain Weave Structure; (b) Warp-Knitted Structure; (c) Weft-Knitted Structure [10]

2.5.2 Deformation Mechanisms of Woven Fabric

The deformation mechanisms of fiber within the RIDFT process are key in understanding and predicting the simulation model. The development of such a model will rely on work developed for diaphragm forming of resin pre-impregnated woven carbon fiber materials [11]. This double diaphragm forming process is similar to RIDFT except pre-impregnated woven

sheets are used instead of vacuum infusion of the fiber. The RIDFT process can be considered static after the initial two-dimensional infusion and thus very similar to the double diaphragm forming immediately before part forming begins.

Glass and carbon fibers in tension and compression deform elastically until failure. Therefore, no isotropic plastic deformation is possible. However, although no forming mechanism that requires more than a tiny amount of fiber elongation will be successful, there are a number of deformation modes that are possible. Woven fabric prepreg stacks have three main deformation modes, with a number of others that have a minor effect or that occur mainly when further deformation by the three main modes requires higher forces [11]. Figure 2.7 illustrates the main modes of deformation for woven fabric prepreg materials. Inter-ply slip is slippage occurring between layers of fiber. Fiber buckling is the deformation of fiber caused by compressive forces, whereas fiber extension is the deformation of fiber caused by tensile forces.

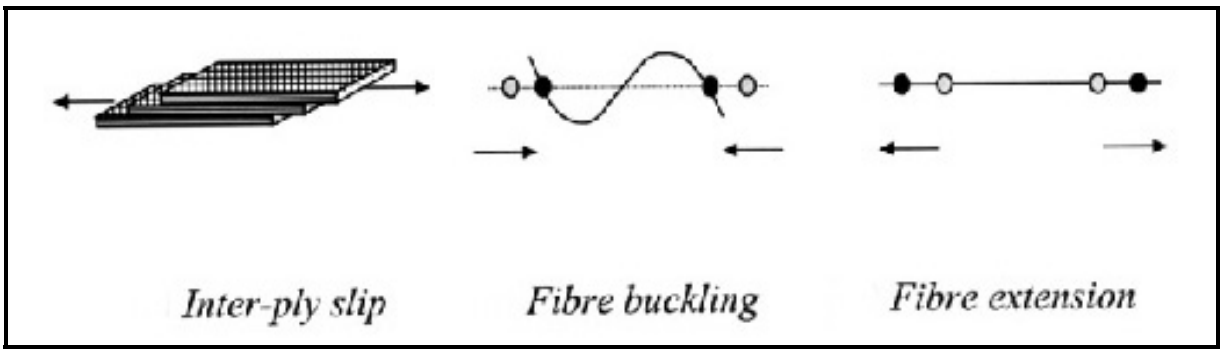

Figure 2.7 Deformation Mechanisms for Textile Composites [11]

The main deformation mechanism available for woven prepreg stacks is intraply shear of the fabric. Figure 2.8a illustrates this type of deformation where the tow crossover acts as the pivot locations. The force displacement curve for this form of deformation is shown in Figure 2.8b [11]. There are three regions to this curve. As load is first applied there is some fiber straightening and slippage between the tows, as well as fabric shear. In the second region of the

curve, shear occurs at a steadily increasing load. In the third region there is an accelerating increase in load caused by the locking angle [11].

The stress-strain curve for this type of behavior can be measured using a "bias extension" test as shown in Figure 2.9 [11]. In the bias extension test, a fiber sample is stretched using a fixture and the deformation is recorded.

Another important deformation mechanism is the slippage or shear between plies, generally known as interply slip. Interply slip occurs for two reasons. The first is that high tensile strains would otherwise occur in the outermost plies when a flat stack is formed over a singly curved surface. The second is that when a flat stack is formed over a double-curved surface, the interply shear at a particular point may be different in plies of different orientations, and thus interply slip must occur to avoid tensile or compressive stress along fiber directions [11]. Inter-ply slippage can be measured by performing slippage tests. Young and Paton [11] performed slippage tests by constructing special fixtures to obtain a plot of the pulling force vs. the pullout distance as shown in Figure 2.10.

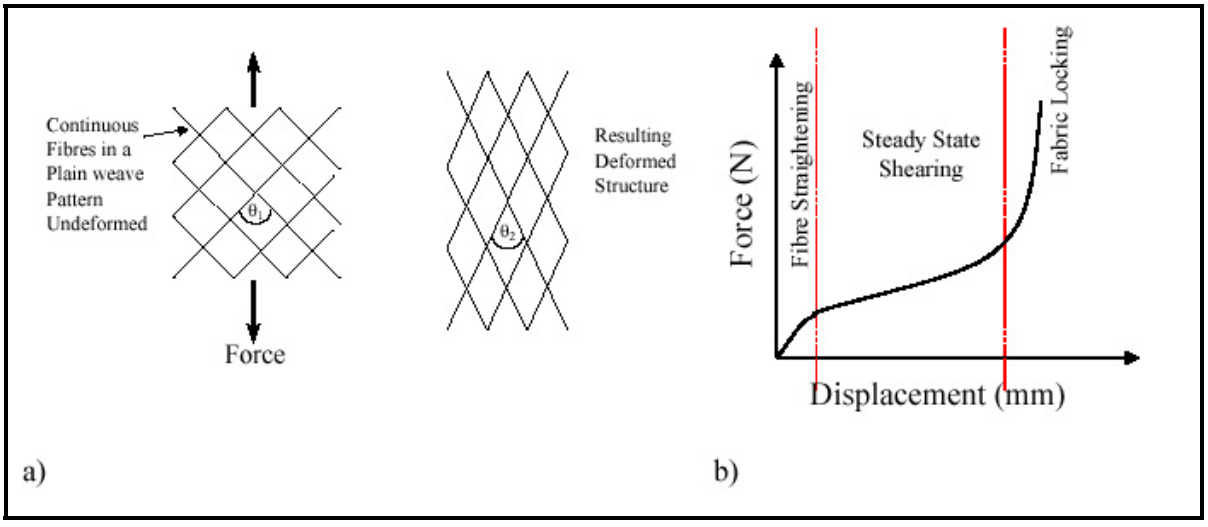

Figure 2.8 Schematic Drawing of: (a) Intra-ply Shear of Woven Fabric; (b) the Force vs. Displacement Relationship [11]

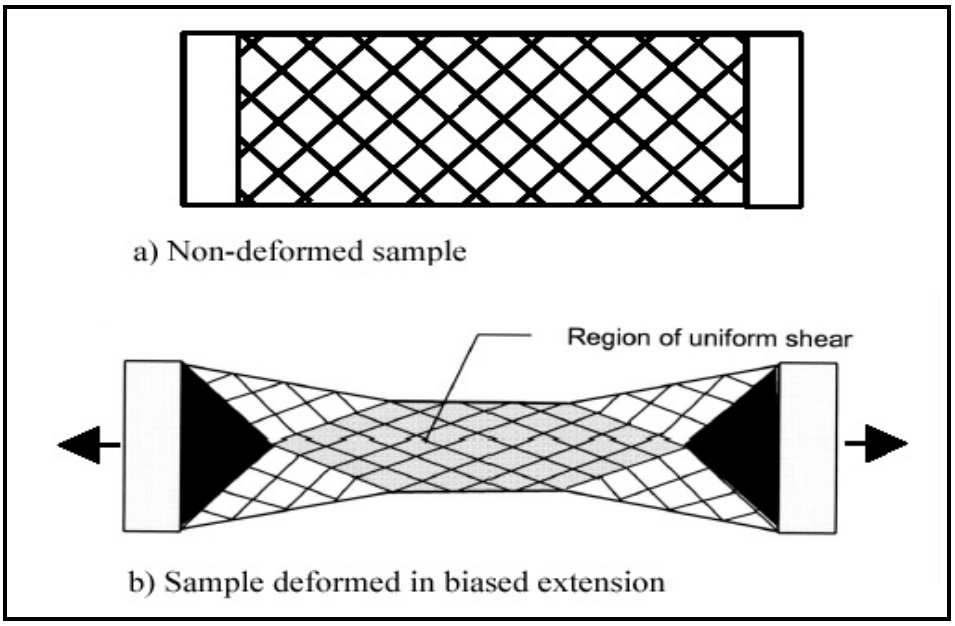

Figure 2.9 Schematic Representation of a Fabric Bias Extension Test [11]

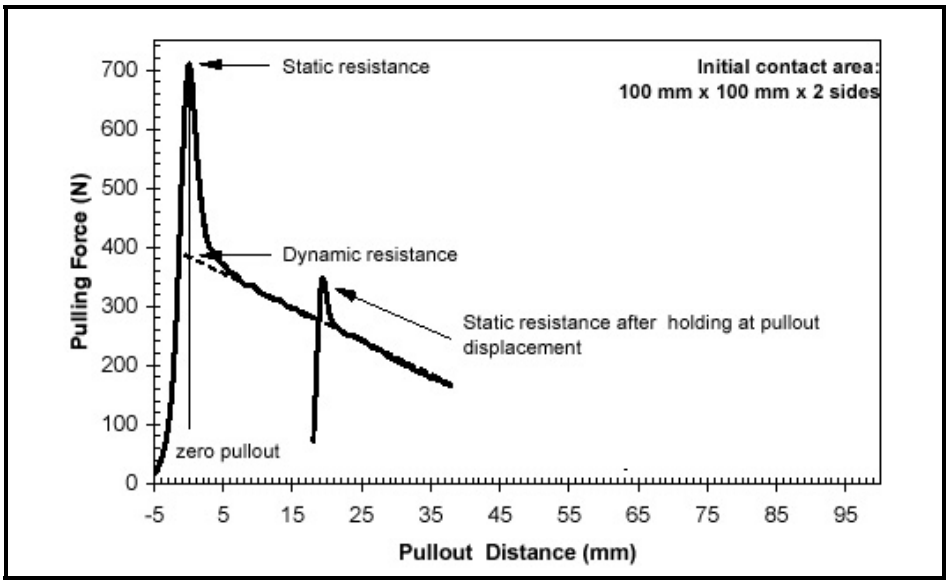

Figure 2.10 A Typical Plot From an Interply Slip Test on Prepreg [11]

The third important deformation mode is ply bending. The bending stiffness of woven prepreg is generally very low in comparison to its in-plane tensile strength, which allows the

prepreg to be formed around tight radii, but makes buckling a significant problem during forming. Bending stiffness is dependent on at least five factors: fiber stiffness, fiber size and distribution within the tows, resin viscosity and fabric geometry [11].

2.6 Fiber Wetting

The quantification of wetting for the RIDFT process can be handled in several different ways. The first approach is the use of the short beam shearing test. A second approach is by measuring the contact angle. Another approach is to measure the void content by burn-off tests or Scanning Electron Microscope (SEM).

2.6.1 Short beam shear

Short beam shear is used to determine interlaminar shear strength of parallel fibers. It is applicable to all types of parallel fiber reinforced plastics and composites. The data can be used for research and development purposes concerned with interply strength, or prove useful in comparing composite materials. Equation 2.7 defines calculation of shear strength from the short beam shear test.

$$\text{Shear strength} = \frac{0.75 * breaking\ load}{width * thickness} \qquad \text{Equation (2.7)}$$

Figure 2.11 illustrates the setup for the short beam shear test.

2.6.2 Contact angle method

The contact angle method is used to determine the wetting ability between the resin and fiber. For a contact angle, $\theta > 90°$, the contact angle is said to be nonwetting [12]. For a contact angle, $\theta < 90°$, wetting is said to occur [12]. For a contact angle, $\theta < 45°$, wetting is said to be very good. However, it is not easy to predict the contact angle, which is related to the interfacial tensions as defined in Equation 2.8.

$$\cos\Theta = \frac{\gamma_{SV} - \gamma_{SL}}{\gamma} \qquad \text{Equation (2.8)}$$

where,

γ_{SV} and γ_{SL} indicate the tensions at the solid-vapor and solid-liquid interfaces, respectively.

Figure 2.12 illustrates the contact angle Θ of a liquid on a solid surface.

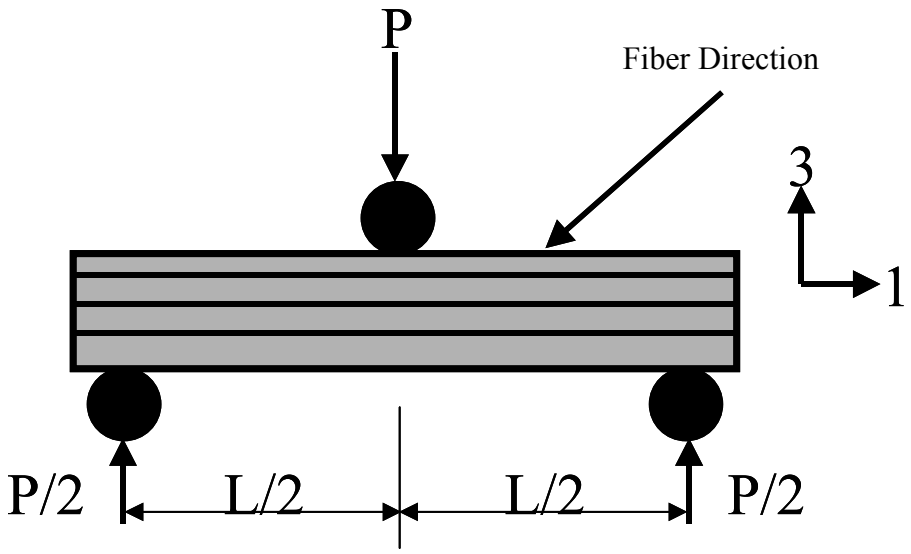

Figure 2.11 Short Beam Shear Test Setup

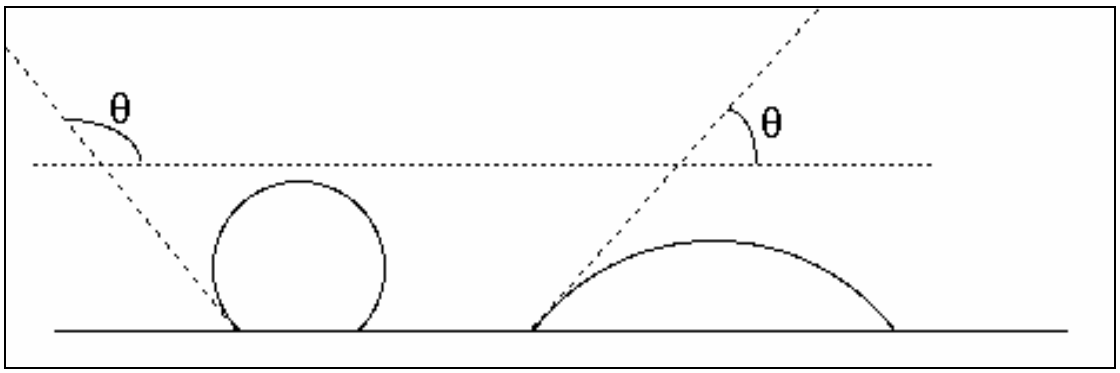

Figure 2.12 Contact Angle θ of a Liquid on a Solid Surface

2.6.3 Burn-off Test

Although this test is not a direct representation of the wetting of the fiber, it will show if the desired V_f are being achieved. It can be said there is a direct relationship between the V_f and the wetting of fibers. If proper wetting occurs the V_f will be higher than if proper wetting did not occur. Having a known target value for V_f will help in defining proper fiber wetting [13].

The burn-off test is defined in Equation 2.9, and the burn-off, B, is calculate from

$$B = \frac{100(W_O - w)}{W_O}(\%)$$ Equation (2.9)

where,

W_O and w are the weights before and after oxidation, respectively.

2.6.4 Scanning Electron Microscope (SEM)

SEM examines specimens to visually determine if proper wetting has occurred. This approach is somewhat subjective based on expert opinion and practical experience. For the RIDFT process the SEM will be heavily utilized as it is a quick and effective method to determine, within a specimen, whether proper wetting of the fiber has occurred.

The quantification of surface quality can be accomplished in several ways. As with aerospace applications, the quantification of surface quality is subjective. However, in many automotive applications the quantification of surface quality is based on Class A finish. For the RIDFT process, the quantification of the surface quality will be looking for resin starved areas on the surface and to compare surface quality with conventional surfaces of parts made from RTM. Unless finishes needed are of Class A nature, this crude, but effective, means of determining part surface finish will be used.

It is necessary to understand how one can visually determine the part surface quality. Figure 2.13 illustrates the surface texture of a woven fiber with a lows surface quality, and the incorporation of a surface vein and good surface quality and an illustration of excellent surface quality.

Initial results from parts produced have yielded good wetting as verified through SEM analysis. With the use of a surface vein, the RIDFT process has gone from producing parts of low surface quality to parts that yield a good surface quality. It is believed that the incorporation of gel coats to the process prior to infusion may allow for parts to yield excellent surface quality. If this type of quality is necessary, the incorporation of a gel coating to the silicone bag before infusion will further reduce thickness variation between weaves and fiber bundles that cause a reduction of surface quality.

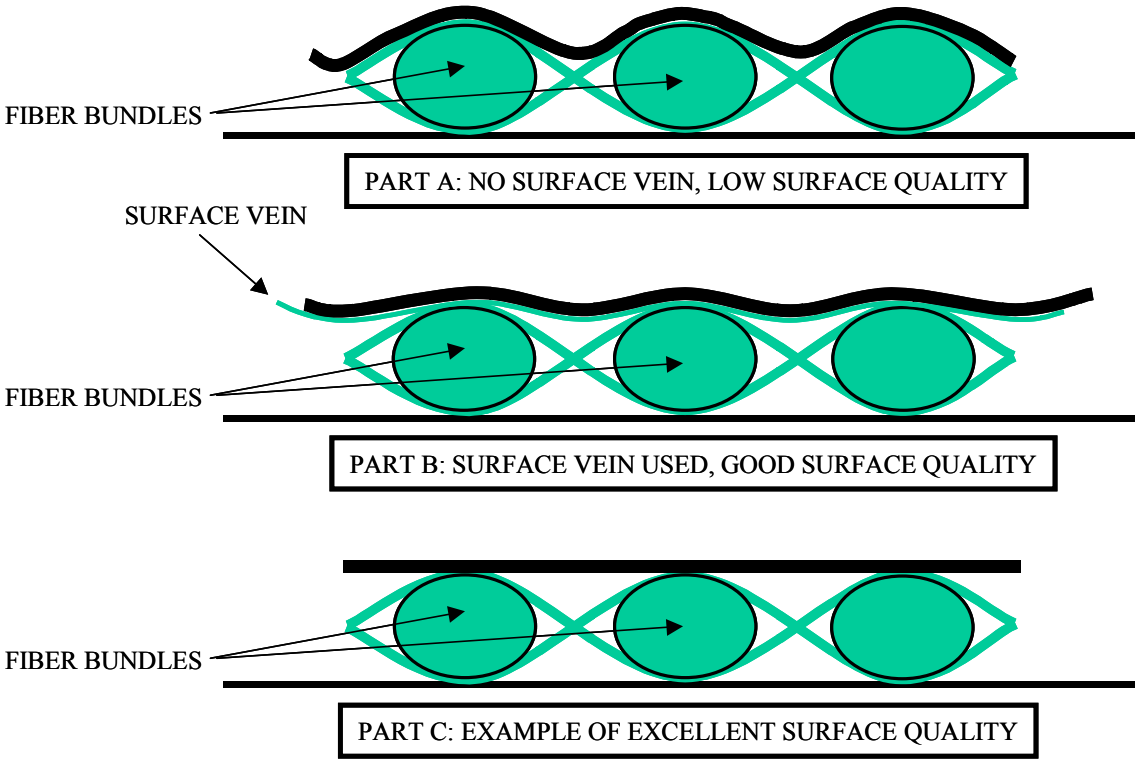

Figure 2.13 Illustration of Surface Quality

2.7 Simulation Modeling

The deformation mechanisms of fiber within the RIDFT process are key in understanding and predicting the simulation model. The development of such a model will rely on work developed for diaphragm forming of resin pre-impregnated woven carbon fiber materials [11]. This double diaphragm forming process is similar to RIDFT for the sake of modeling except pre-impregnated woven sheets are used instead of vacuum infusion of the fiber. After the initial two-dimensional infusion the RIDFT process is very similar to the double diaphragm forming (DDF) immediately before part forming begins.

2.7.1 Fiber-Resin Interactions

For the DDF process, the PAMFORM software was used to simulate the fiber –resin interaction for the prepreg. PAMFORM software describes the prepreg using a thermo-visco-elastic material model. This material model was developed to simulate the forming behavior of

dry or pre-impregnated fabric (uni-direction, woven or non-woven). The material model effectively describes the behavior of three material phases loaded in parallel: a linear elastic phase (corresponding to the reinforcement fiber), a thermo-visco-elastic phase (corresponding to the resin) and a elasto-plastic phase which is necessary to help describe the shear deformation in the fabric. Large strains in the forming process can be simulated [11].

The similarities between DDF and RIDFT are such that the modeling to describe the fiber-resin interactions are quite the same. The thermo-visco-elastic phase will be the only phase of the thermo-visco-elastic material model that will require tailoring. Differences of resin between a prepreg and infused fiber can be defined as rheological in nature.

2.7.2 Diaphragm Modeling

Work performed by Young & Paton [11] on the development of the PAMFORM software for the modeling of the DDF process did not necessitate the need for modeling the diaphragm characteristics outside of their interactions with the fiber and mold surface. The top and bottom diaphragms were discretized individually and described by shell elements [11]. However, the diaphragm properties are modeled with the fiber-diaphragm interaction and the mold-diaphragm interaction and are described below.

2.7.3 Fiber-Diaphragm Interaction

For the fiber to diaphragm interfaces, bilateral segment-to-segment contact was used for the simulations. Coulomb friction was assumed for all contact interfaces [11].

2.7.4 Mold-Diaphragm Interaction

For the tooling, including the forming box (mold), discretization was applied to the surface geometry only and shell elements with null material were used. The diaphragm to mold interface was simulated by node-to-node segment contact. Coulomb friction was assumed for all contact interfaces [11].

2.7.5 Part Thickness Consistency

The modeling of part thickness consistency for the RIDFT process can also be achieved by using the PAMFORM modeling software. The interactions affecting drapability will also affect part thickness consistency and will be used in its determination. The ability of the software to model drapability based on the models also enables it to determine part thickness with the no addition of input variables.

2.7.6 Model Output

Forming simulations for two cases were performed by Young & Paton [11]. They were identical in every aspect except the vacuum levels between the diaphragms were conducted by Young and Paton [11]. The Case 1 simulation had full vacuum applied between two diaphragms. The pressure-time history for top and bottom diaphragms is plotted in Figure 2.14a. Note that the pressure in the plot is actually the pressure difference across the diaphragm [11].

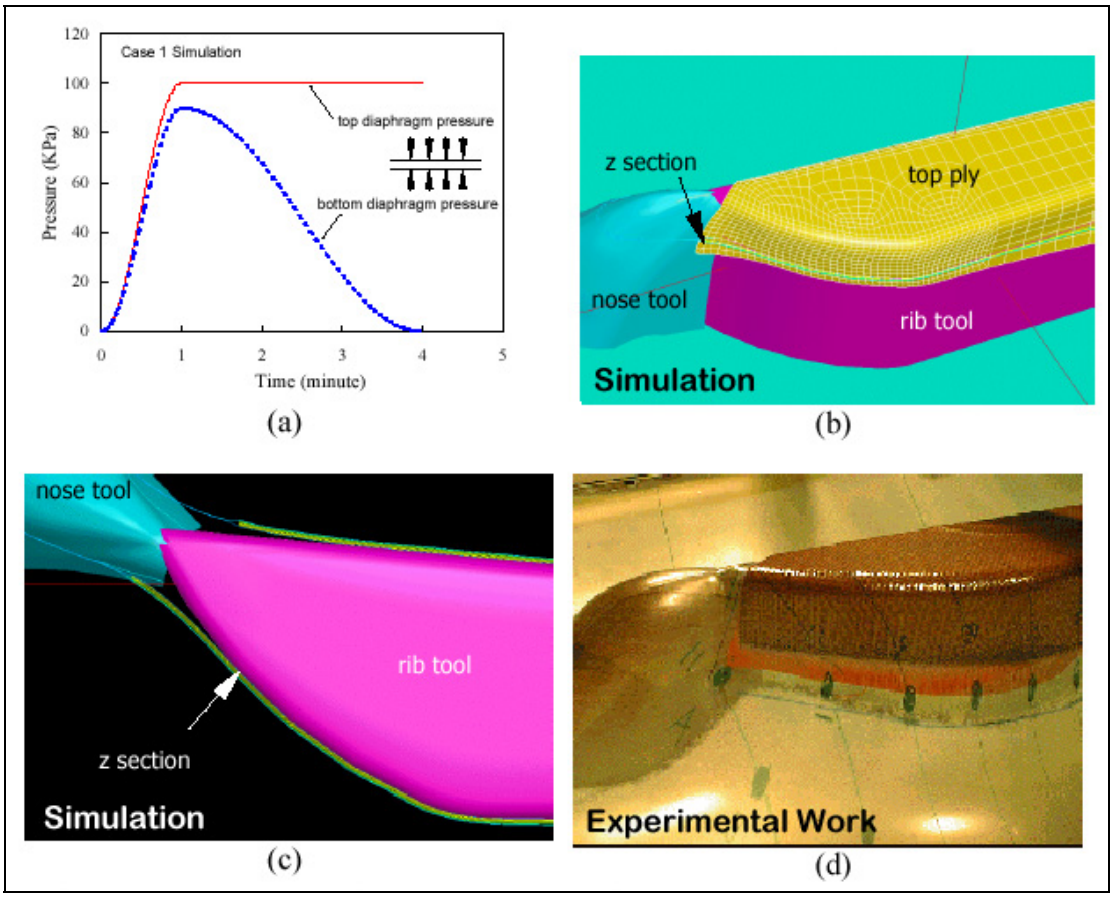

Figure 2.14 Simulation with Full Vacuum Between Diaphragms [11]

Figures 2.14b and 2.14c illustrate the deformation profile at the end of the forming process for the Case 1 simulation. The simulation predicts that the stack will be formed fully with no wrinkles. Experimental work shown in Figure 2.14d verifies this [11].

The Case 2 simulation had only partial vacuum applied between the diaphragms. The pressure-time history for this simulation is plotted in Figure 2.15a. Figure 2.15b and 2.15c demonstrate the deformation profile at the end of forming process in the Case 2 simulation. The simulation predicts that the flange will be wrinkled. Experimental work shown in Figure 2.15d verifies this [11].

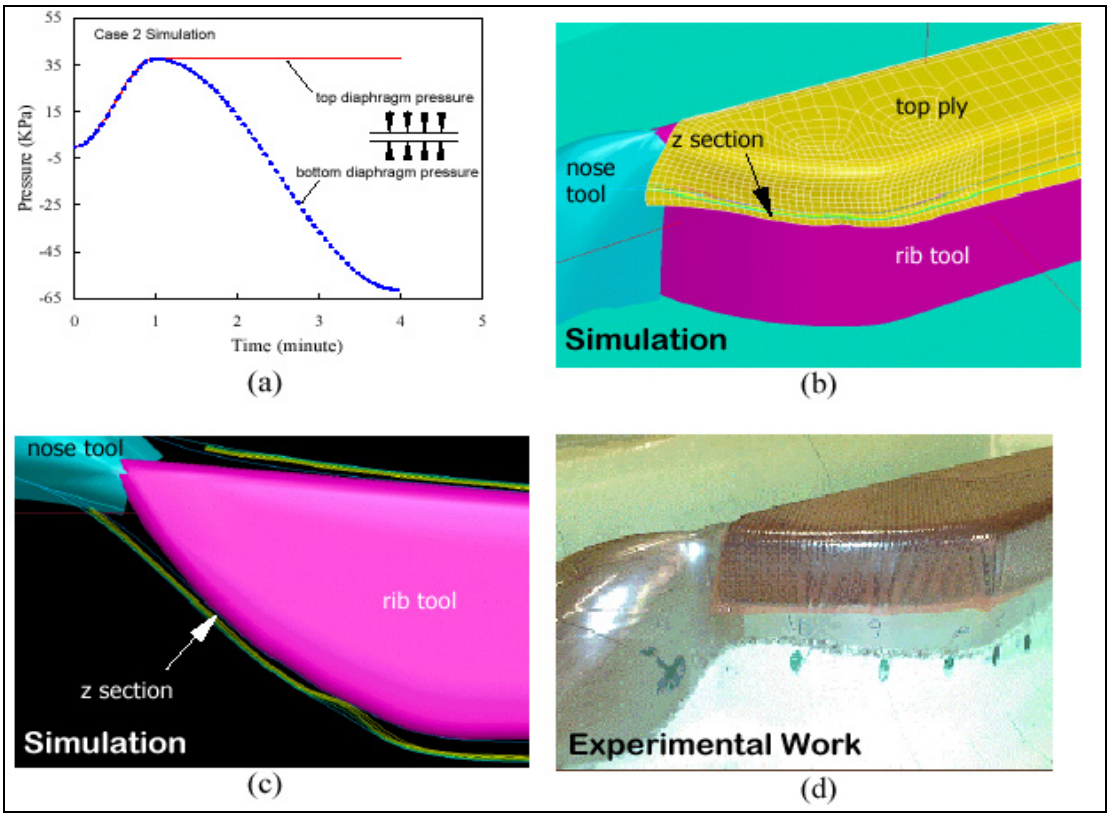

Figure 2.15 Simulation with Partial Vacuum Between Diaphragms [11]

2.8 Conclusions

Comparing to other liquid composite molding (LCM) techniques, the RIDFT process has many advantages. With the bottom flexible tooling surface, the cleanup and pre-manufacturing prep work is reduced. Resin contact with the mold surface does not occur and eliminates the

need to prepare the mold before each cycle. In addition to reducing a manufacturing step, this does not lend itself to tool wear experienced from continuous use as seen in the RTM process. More important, RIDFT does not require expensive preforms and handling complex resin flow problems. With traditional RTM processes the problems of high tooling costs and long cycle times are of concern. The RIDFT process requires only one mold halve to be used during manufacturing.

However, the nature of the RIDFT process is also complex due to the forming process. It involves many aspects of drapability of reinforcement fabrics and interactions of fiber-fiber, fiber-silicone, silicon-silicone and silicone-tooling. In order to fully investigate and understand the nature of the RIDFT process it is necessary to systematically characterize the formability of fiber preforms and multiple interactions existing during process forming.

PAMFORM was successfully used to model the DDF process, which is very similar to the RIDFT process. RIDFT is a novel manufacturing technique of affordable LCM processes. It is also a challenge to fully understand the process due to the complex nature for drapability of fiber reinforcements and multiple interactions of fiber-fiber, fiber-silicone, silicon-silicone and silicone-tooling during process operations.

CHAPTER 3

EXPERIMENTAL METHODOLOGY OF INDUSTRIAL RIDFT MACHINE BUILDING AND SIMULATION OF RIDFT FORMING

3.1 Design, Construction and Demonstration of Industrial RIDFT Machine

The industry grade RIDFT machine was produced with the knowledge gained from a thorough understanding of the RIDFT process, information gathered from the design and use of the initial RIDFT prototype and the desired results the research hoped to achieve. The RIDFT machine needed to utilize a large vacuum chamber, reliable and easy operation of vacuum sealing and reducing flexible tooling stretch during forming so that it is suitable for the size of the largest desired part to be made. From this, all other aspects of the machine were built. A suitable size for the vacuum chamber was determined by the sponsored research. For the sponsored research, a part dimension no larger than 5 ft. (width) x 10 ft. (length) x 1 ft. (height) was required.

3.1.1 Vacuum Chamber Design Calculations

An important issue in the chamber design is its ability to limit the stretching of the silicone during part forming. The maximum elongation of the Bondline[1] silicone is 650 percent before failure occurs. From this information, this research decided for a worst case scenario the elongation of the silicone was not to exceed 350 percent. The worst case scenario was determined to be a rectangular box with dimensions 5 ft. (width) x 10 ft. (length) x 1 ft. (height). Figure 3.1 illustrates how the determination of the chamber design was derived based on the desired 350 percent elongation of the flexible silicone tooling.

In order for the fiber to completely drape over the sides of the part, the fiber needs to extend past the mold edge by the maximum distance as defined by the height of the mold, which is 1 ft.

[1] Bondline Products, Norwalk, CA

It is also known the least elongation of the silicone would occur if the distance from the silicone edge to the base of the mold edge was minimized. This was achieved by angling the vacuum wall, at an angle of θ, from the base of the mold to the silicone edge as illustrated in Figure 3.1.

To determine the amount of silicone required past the fiber edge so as not to exceed 350% elongation, a calculation was performed. Equation 3.1 defines the calculation of distance, d, from the fiber edge to the silicone edge as illustrated in Figure 3.1. Equation 3.2 defines the angle, θ, representing the angle of the vacuum chamber wall from the silicone edge to the base of the mold as illustrated in Figure 3.1.

$$3.5d = h, \text{ where } h = \sqrt{(d+1)^2 + 1^2}$$

$$3.5d = \sqrt{(d+1)^2 + 1^2}$$

$$11.25d^2 - 2d - 2 = 0$$

$$d = .52\,ft$$

Equation (3.1)

$$\theta = \tan^{-1}\frac{1}{1+.52}$$

$$\theta = 33.3^o$$

Equation (3.2)

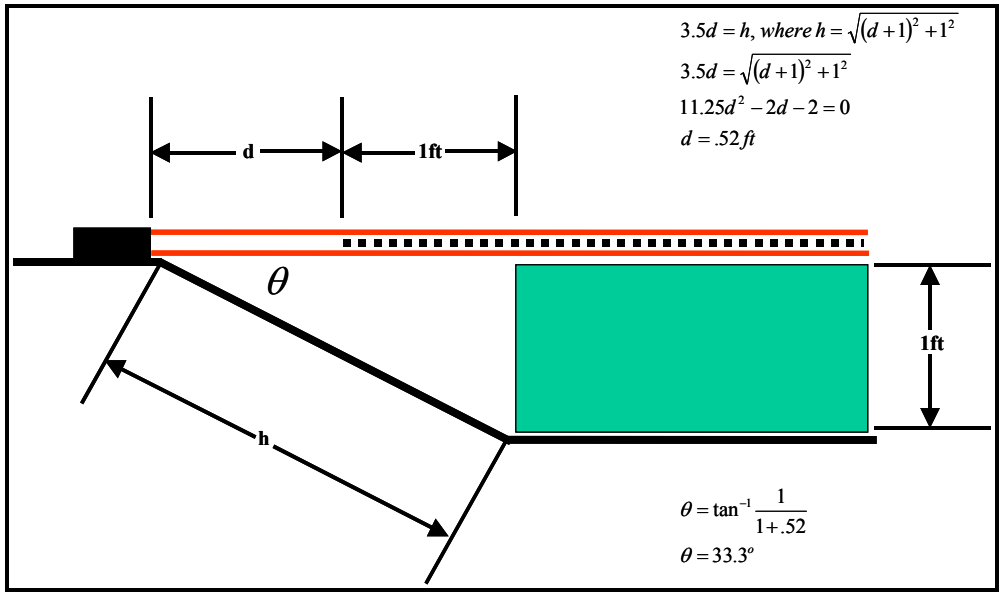

Figure 3.1 Chamber Design

3.1.2 Vacuum Chamber Design

From the design calculations the vacuum chamber for the RIDFT machine was then designed. The material selected for the chamber frame was 1.5 in. x 0.125 in. box tubing. This material was selected for its high strength and low cost. Figure 3.2 illustrates the design of the vacuum chamber. The material selected for the chamber walls was 0.125 in. sheet metal. It was selected for its strength and ability to resist warping and denting during welding and fabrication of the chamber. The vacuum chamber frame was gas-metal-arc-welded (MIG) welded by a certified welder and the vacuum chamber walls were MIG welded with two separate passes on each seam to assure no vacuum leakage would occur.

3.1.3 Leg Support Design

The next aspect of the RIDFT machine design was the leg supports used to hold the chamber to working height. The leg supports were also constructed from 1.5 in. x 0.125 in. box tubing for its strength in supporting the vacuum chamber, sealing frames and the weight of the mold. The leg supports were MIG welded by a certified welder. There are four rows of leg supports below the vacuum chamber. Figure 3.3 illustrates one of the leg supports for the RIDFT machine.

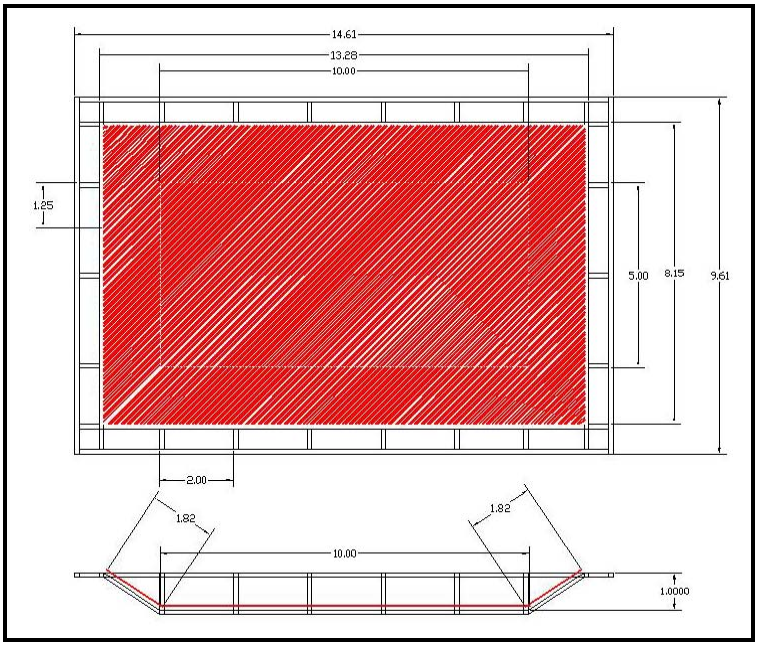

Figure 3.2 Vacuum Chamber Design.

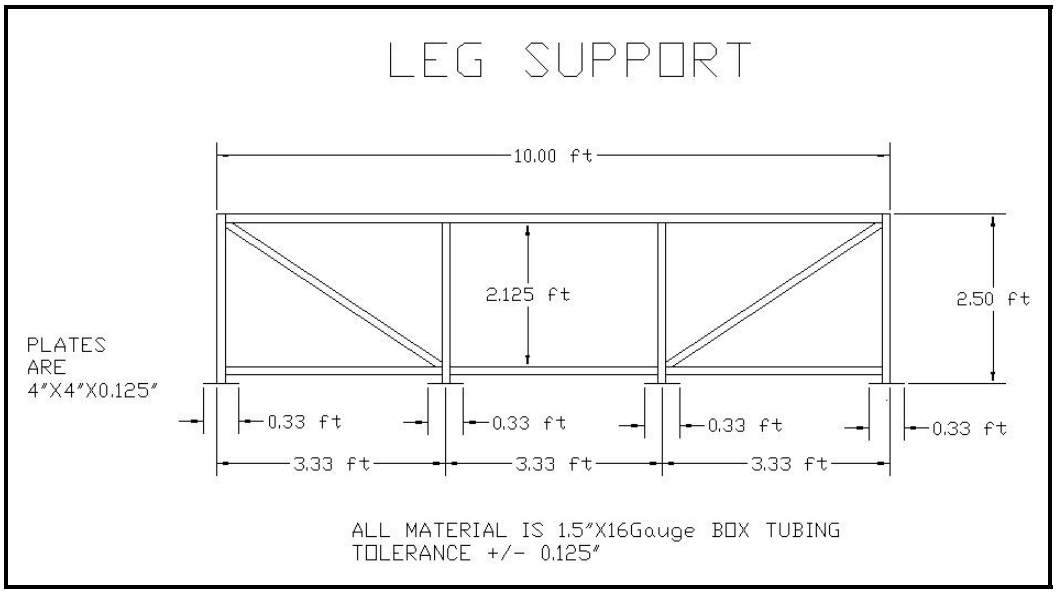

Figure 3.3 Leg Support Design

3.1.4 Sealing Frame Design

The sealing frame design is a critical aspect of the RIDFT process. It is important for the sealing frame to maintain vacuum integrity during the RIDFT process. It is also important for the sealing frame to be quickly and easily used so the process is more robust in nature. The sealing from design used for the industrial RIDFT machine is taken from the original RIDFT prototype. After four iterations of sealing frame designs, a design was established that has yielded excellent sealing and clamping characteristics while being quickly and easily used. Figure 3.4 illustrates the sealing frame designed developed from the RIDFT prototype.

3.1.5 Vacuum Control Panel

The final phase for the completion of the industrial RIDFT machine was the design, fabrication and assembly of the RIDFT pressure control panel. Because the RIDFT machine is a vacuum and pressure driven process it is important for precise control of the vacuum chamber pressure, sealing frame pressure and fiber infusion pressure. From the requirements of the RIDFT process and its need to control various pressures the vacuum control panel was developed.

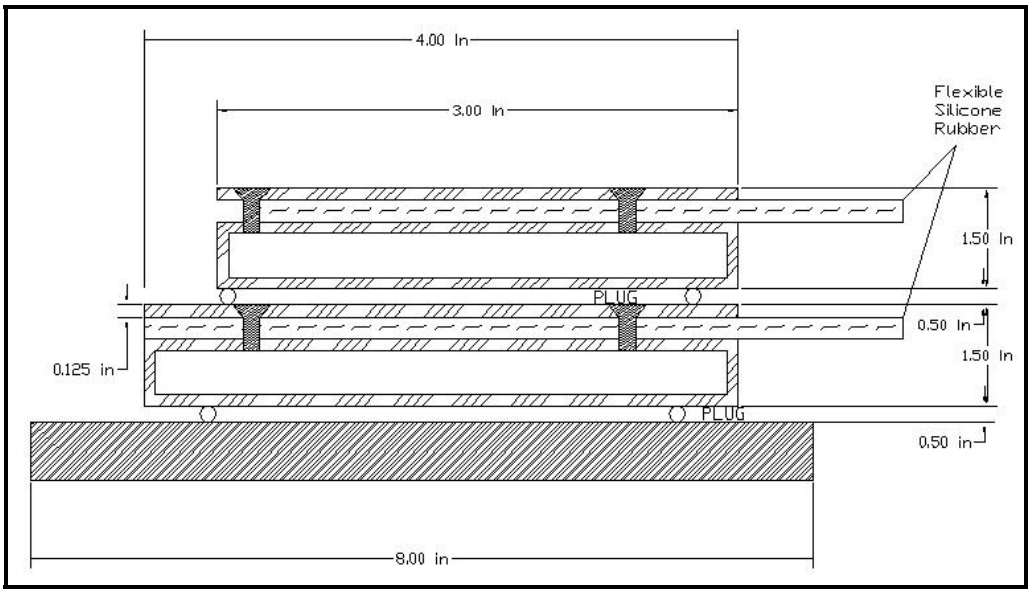

Figure 3.4 Sealing Frame Design

3.2 Modeling and Simulation of the RIDFT Process

In order to better understand the forming mechanics within the RIDFT process and to predict the formability of a desired geometry, a simulation model must be created. The RIDFT process is dynamic and simulation software must be chosen that can account for various materials used within the process, interactions of these materials and the forces applied during the RIDFT forming process.

The PAMFORM software was chosen because it is a general purpose finite element package for the industrial virtual manufacturing of non-metallic sheet forming. It is unique in its ability to model a variety of forming processes. These processes include the following:

- Blow forming
- Diaphragm forming
- Stretch forming
- Press forming with rigid and flexible tooling
- Thermoplastic and thermosetting based polymers
- Hand lay-up

Other unique features of the PAMFORM software are the material models for reinforced and unreinforced polymers [14]. These material models include the following:

- Hyper-Elastic models for unreinforced plastics (Mooney-Rivlin and Ogden)
- Thermo-visco-elastic models (G'Sell)
- Models for dry fabrics (Uni-directional, woven and NCF)
- Models for Thermo-set and Thermoplastic based continuous fiber reinforced composites

Typical applications of the PAMFORM software include carpet and fabric forming, automotive interior plastic and fabric panels, automotive fuel tanks, plastic containers, food packaging and advanced aerospace and automotive fiber reinforced components. The PAMFORM software is ideal for modeling the RIDFT process because of its flexibility in modeling various processes and because of the information that can be obtained from simulation model results [14]. These results include the following:

- Animation of the forming process
- Visualization of any wrinkles
- Fiber direction (or angle) at any time step during the process
- Thickness distribution of any ply at any time step during the process
- Strains and stresses distributions of any ply at any time step during the process
- Void content (to visualize consolidation) in between any two plies at any time step during the process
- Temperature distribution of any ply at any time step during the process

In order to model the RIDFT process, part geometry, material characteristics and multiple interactions should be included. Figure 3.5 illustrates the flow chart for the process by using the PAMFORM software.

3.2.1 Creation of Part Geometry and Vacuum Chamber Mesh

The initial step in the development and use of the RIDFT simulation model is to develop the mesh for both part geometry and RIDFT vacuum chamber. The PAMFORM software is unique in its ability to create the required mesh specific to the requirements of the software with its Deltamesh module.

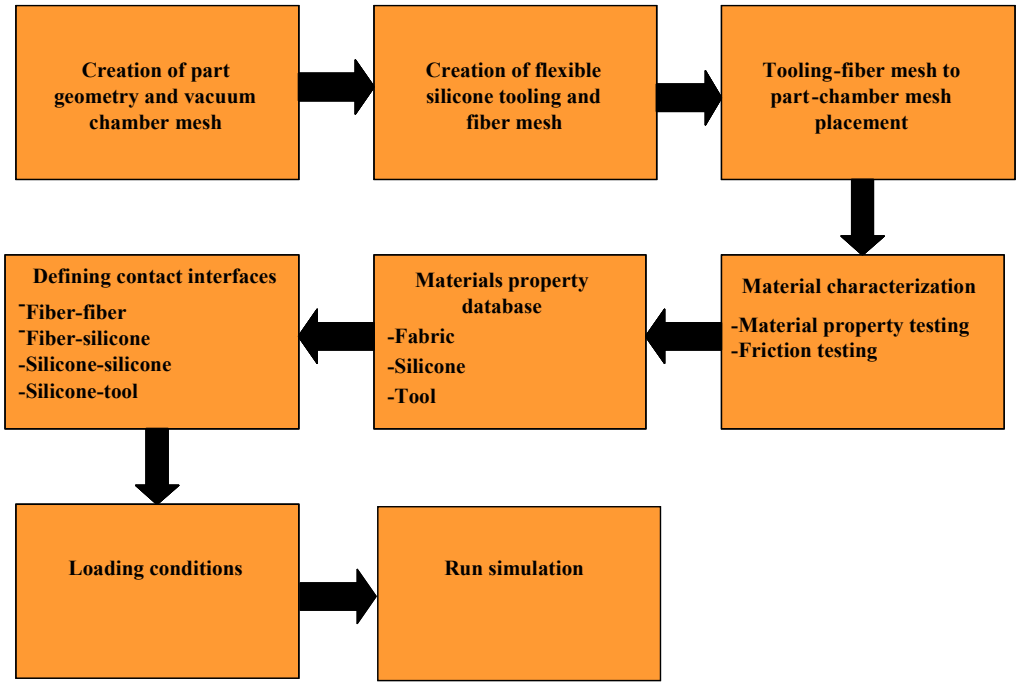

Figure 3.5 Flow Chart for PAMFORM Software Use

The process begins by creating an Initial Graphics Exchange Specification (IGES) file within PRO Engineering[2] of the desired part geometry to be simulated and the vacuum chamber used within the RIDFT process. In this step the two features are merged together into a single drawing for the creation of the IGES file. This merging is necessary because both part geometry and vacuum chamber are treated as rigid bodies with no displacement or rotation during the simulation process.

Several important criteria must be defined before the IGES file is imported into the Deltamesh module for the creation of the part geometry and vacuum chamber mesh [14]. These factors include:

- Drawing tolerances=0.1mm
- Gap-overlap tolerances=0.5mm
- Maximum ratio between gap and surface=0.8mm

After the IGES file has been successfully imported into Deltamesh, the mesh parameters are then required for the mesh creation. These parameters include the following [14]:

[2] PRO Engineering

- Minimum and maximum elements size
  - Minimum of six elements within the smallest radius
  - Minimum= 0.0039 in.
  - Maximum= 1.18 in.
- Chordal error= 0.0059 in.
- Maximum angle between two consecutive angles= 15 degrees
- Aspect ratio (length to width) ≤ 10
- Quad surface detection
- Mesh algorithm type (parametric for tool and uniform for silicone/fiber blank)

Following the creation of the RIDFT mesh the file is then saved into a *.dsy file format. The *.dsy file format is for use with the PAM Generis module of the PAMFORM software. Figure 3.6 illustrates a mesh created within Deltamesh for both part geometry and vacuum chamber.

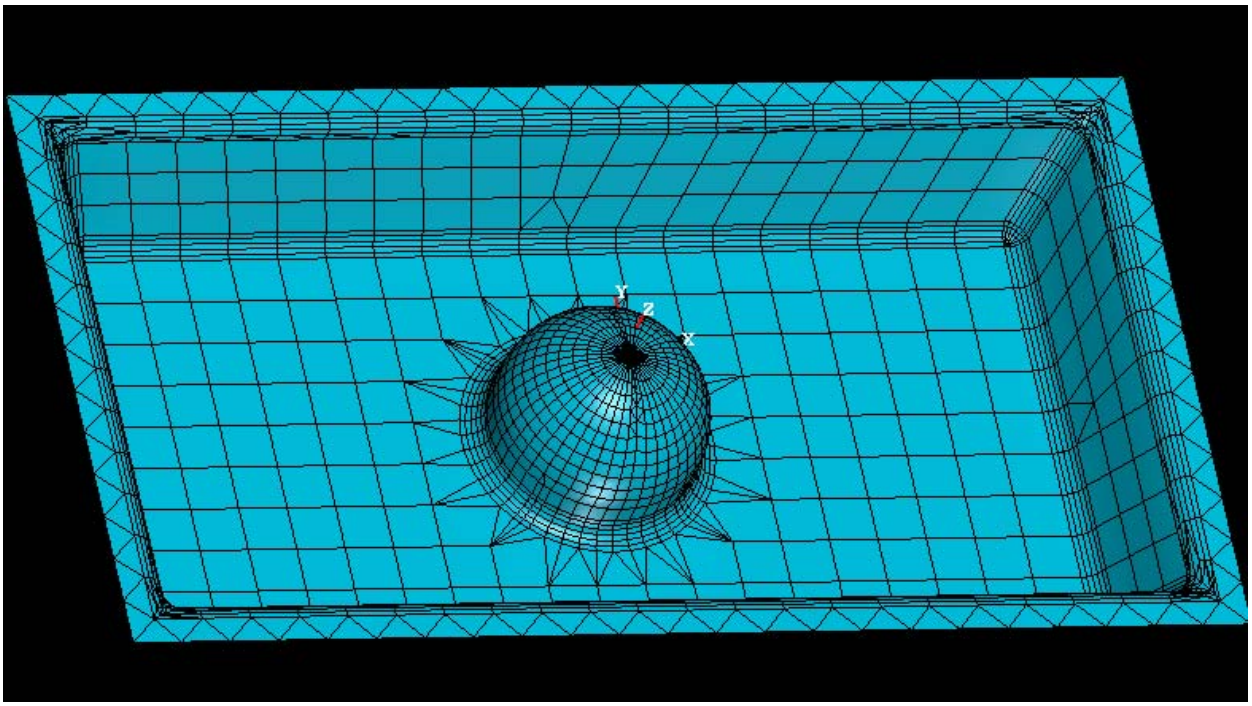

Figure 3.6 Part Geometry and Vacuum Chamber Mesh

3.2.2 Creation of Flexible Silicone Tooling and Fiber Mesh

The next step in the development and use of the RIDFT simulation model is to create the mesh for both flexible silicone tooling and fabric layers. The PAMFORM software is unique in its ability to create the required mesh specific to the requirements of the software using either the Deltamesh module or PAM Generis.

When using the Deltamesh module for the creation of both flexible silicone tooling and fiber mesh the same procedures to generate the mesh for the part geometry and RIDFT vacuum chamber are used. An easier alternative for the creation of the blank mesh for both flexible silicone tooling and the fiber is to use the stamping/blanking option within PAM Generis. With this feature of PAM Generis a simply pattern is selected with the mesh being created by the Quadrilateral method. This method allows for four points to be defined representing the four corners of the fiber or flexible silicone tooling. After the corners are defined the element size is selected and the mesh is created. Additional fiber layers are created by use of a duplicating feature for the initial fiber layer generated.

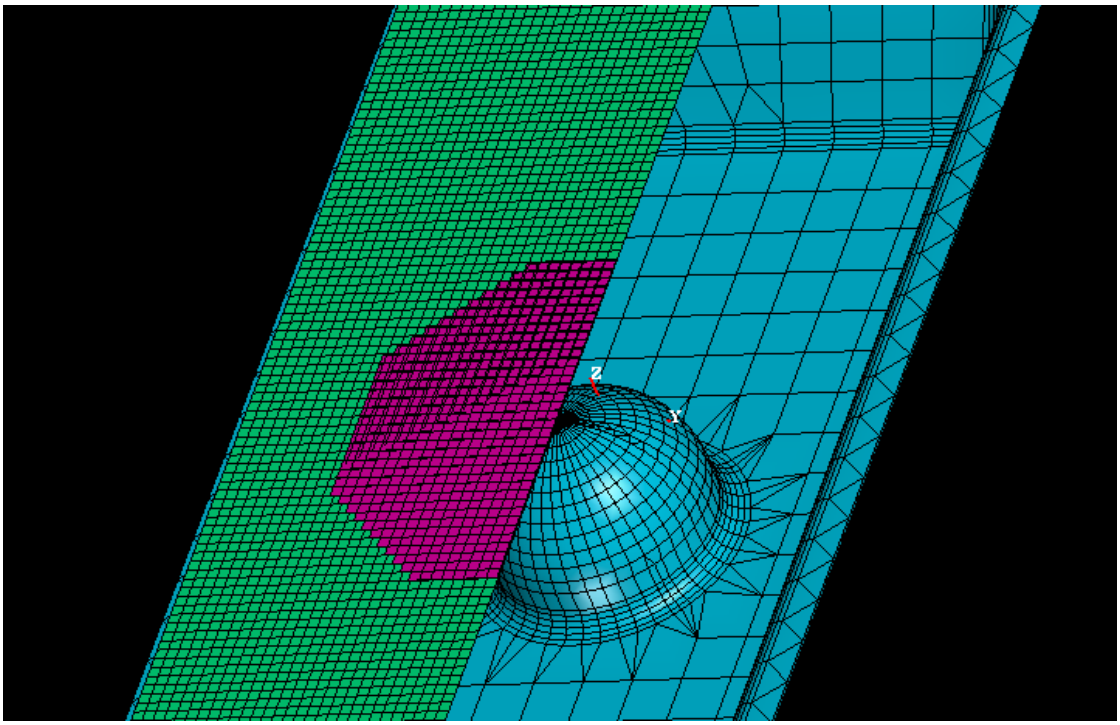

Figure 3.7 Orientation of RIDFT Components during RIDFT Simulation

3.2.3 Tooling-Fiber Mesh to Part-Chamber Mesh Placement

The next step in the development of the RIDFT simulation model is the merging and placement of the part geometry and vacuum chamber rigid body with the flexible silicone tooling and fiber layers. This step orients the different component meshes within the RIDFT simulation model as they are oriented on the actual RIDFT machine. Figure 3.7 illustrates the flexible silicone sheet over the part geometry and vacuum chamber rigid body as the simulation is being performed.

3.2.4 Materials Property Database

Following the mesh placement for the part geometry and vacuum chamber rigid body with the flexible silicone tooling and fiber, the materials characteristics are then defined. Within the RIDFT simulation model three distinct material types are used and defined.

3.2.4.1 Material type 121 for the flexible silicone sheets. The material model is characterized as nonlinear thermo-visco-elastic for shell elements (G'Sell Model). Inputs for this material model include initial thickness, Young's Modulus and mass density. The governing equation used within the PAMFORM software is listed in Equation 3.3 [14].

$$\sigma = k(1-\exp(-\omega\varepsilon)) \times (\exp(h\varepsilon^2))\varepsilon^m \qquad \text{Equation (3.3)}$$

where,

σ = stress,

ε = strain,

k = scaling factor (162.496psi),

m = strain rate hardening exp (0.095),

h = strain hardening coefficient (1.669) and

ω = visco-elastic coefficient (3.691).

The forming diaphragms used with RIDFT consist of silicone rubber sheets where deformation is characterized as primarily elastic. Silicone rubber diaphragms are more expensive than nylon sheets, but can be re-used which saves costs in the long term. One drawback is silicone rubber can exhibit some permanent set due to the Mullins effect [11]. In this research, testing to validate the properties of the flexible silicone tooling material was performed

3.2.4.2 Material type 140 for the fiber reinforcement. The material model is characterized as thermo-visco-elastic matrix with elastic fibers for shell elements. Inputs for this material model include the following [14]:

- Material density
- Locking angle from a picture frame test
- Young's Modulus in 0° and 90°
  - Stress vs. strain curves in 0° and 90° at different strain rates
- Shear modulus using picture frame test or stress vs. strain in 45°
  - Stress vs. strain curves in 45° at different strain rates
  - Perform picture frame test to calculate shear modulus (G)
- Effective viscosity using picture frame test, Equation 3.4

$$\vec{F} = S \times \mu \times \frac{dE}{dt} \qquad \text{Equation (3.4)}$$

where,

S = fabric surface area,

$\frac{dE}{dt}$ = shear strain rate and

μ = effective viscosity.

- Bending factor
  - Stiffness of fabric
  - Determined experimentally using ASTM 1388

3.2.4.3 Material type 100 for the tooling and vacuum chamber. The material model is characterized as null material for shell elements. The null material for shells is a convenient and economic tool for the modeling of contact surfaces when internal forces and deformations of these surfaces are not of interest [14].

3.2.5 Defining Contact Interfaces

Contact interfaces within the PAMFORM software are used to define the interactions that occur within the simulation model. For the RIDFT simulation model there are four contact interfaces that occur and are listed as follows:

- Fiber layer-to-fiber layer interface
- Fiber layer-to-silicone interface

- Silicone-to-silicone interface
- Silicone-to-tooling interface

These interfaces can be characterized within the modeling software by use of two primary contact interface types and two secondary contact interface types. The interface types chosen are predefined by the PAMFORM users manual for the different contact treatments. The interface types include the following [14]:

- Type 16 Lagrangian contact – silicone-to-tooling interface
- Type 15 Contact blank/tool – silicone-to-tooling interface
- Type 33 Surface/surface – fiber-to-fiber, fiber-to-silicone, silicone-to-silicone interfaces
- Type 13 Bilateral contact - fiber-to-fiber, fiber-to-silicone, silicone-to-silicone interfaces

The interface contact frictions are characterized and defined in Chapter 4, Material Characterization.

3.2.5.1 Type 16 Lagrangian contact for flexible silicone to tooling surface interface. Critical input parameters for this contact interface include friction and search frequency. The search frequency refers to how often the model searches for the contact between the flexible silicone sheet and the tooling surface. The contact treatment used for this interface is a bucket search. The bucket search is the type of search method used to determine when contact between the flexible silicone sheet and the tooling surface has occurred. This search is performed according to the search frequency calculating whether nodes of the flexible silicone sheet have contacted the tool surface. Figure 3.8 illustrates the bucket search approach.

The contact enforcement used for this interface is Lagrangian. For the Lagrangian enforcement, if the silicone passes the tool, the silicone is displaced back away from the tool equal to the distance the tool was violated. This enforcement keeps the silicone from passing the tool within the simulation model.

3.2.5.2 Type 15 contact blank/tool for flexible silicone to tooling surface interface. Critical input parameters for this contact interface include friction, penalty, search frequency and contact damping. The search frequency refers to how often the model searches for the contact between the flexible silicone sheet and the tooling surface.

The contact treatment used for this interface is a bucket search. The bucket search is the type of search method used to determine when contact between the flexible silicone sheet and the tooling surface has occurred. This search is performed according to the search frequency

calculating whether nodes of the flexible silicone sheet have contacted the tool surface. Figure 3.8 illustrates the bucket search approach.

The contact enforcement used for this interface is a penalty contact. The contact enforcement addresses how, if the silicone passes the tool surface, the silicone is moved back away from the tool. This may occur if the movement of the flexible silicone sheet between time steps and search frequency allows it to travel past the tool. The penalty contact works by assessing a penalty value within the contact interface. This penalty value is used to apply a force normal to the tool to force the silicone back from the tool surface. Equation 3.5 defines the contact penalty, while figure 3.9 illustrates the contact penalty force.

$$\vec{F} = p \times \vec{\delta} \qquad \text{Equation (3.5)}$$

where,

p = penalty value and

δ = distance silicone has violated the tool.

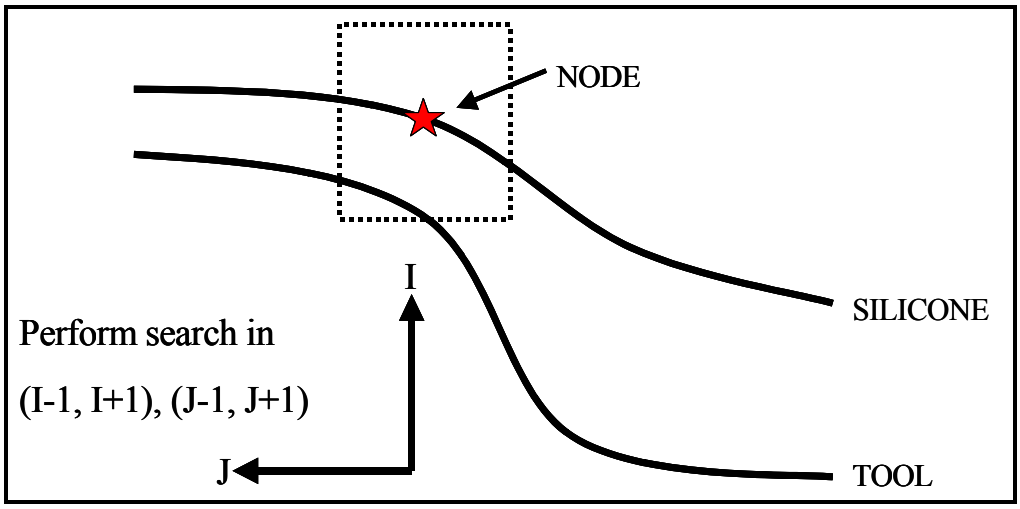

Figure 3.8 Bucket Search Approach [15]

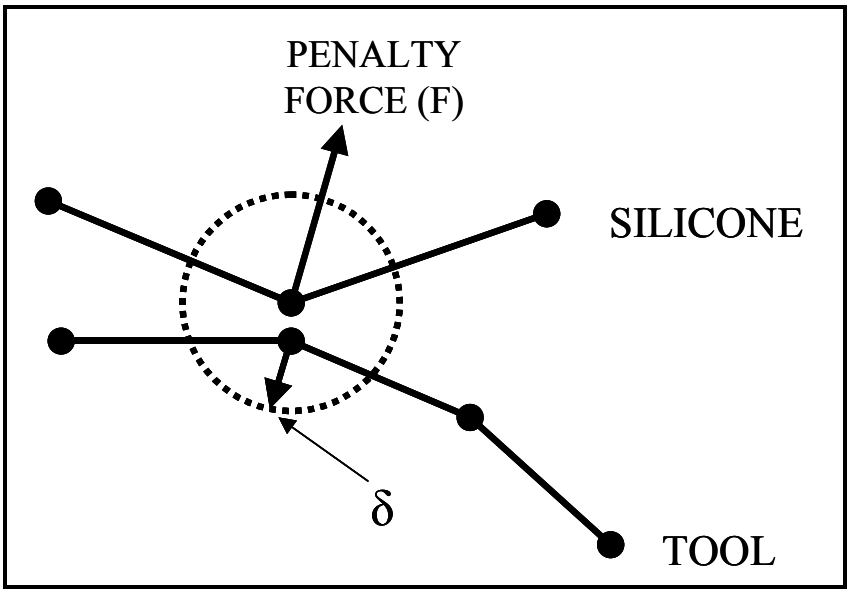

Figure 3.9 Contact Penalty [15]

3.2.5.3 Type 33 surface/surface and type 13 bilateral contact. These contact interface models are used to describe the interface between the fiber-to-fiber, fiber-to-silicone and silicone-to-silicone surfaces. Critical input parameters for these contact interfaces include friction, thickness, penalty, search frequency and stiffness damping. The search frequency refers to how often the model searches for the contact between the specified surfaces.

The contact treatment used for these interfaces is a connectivity search. The connectivity search is the type of search method used to determine when contact between fiber-to-fiber, fiber-to-silicone and silicone-to-silicone surfaces has occurred. This search is performed according to the search frequency calculating whether nodes of the flexible silicone sheet have contacted the tool surface. According to the connectivity search, contact will happen when the node is half the thickness of the silicone away from the tool surface. Figure 3.10 illustrates the connectivity search.

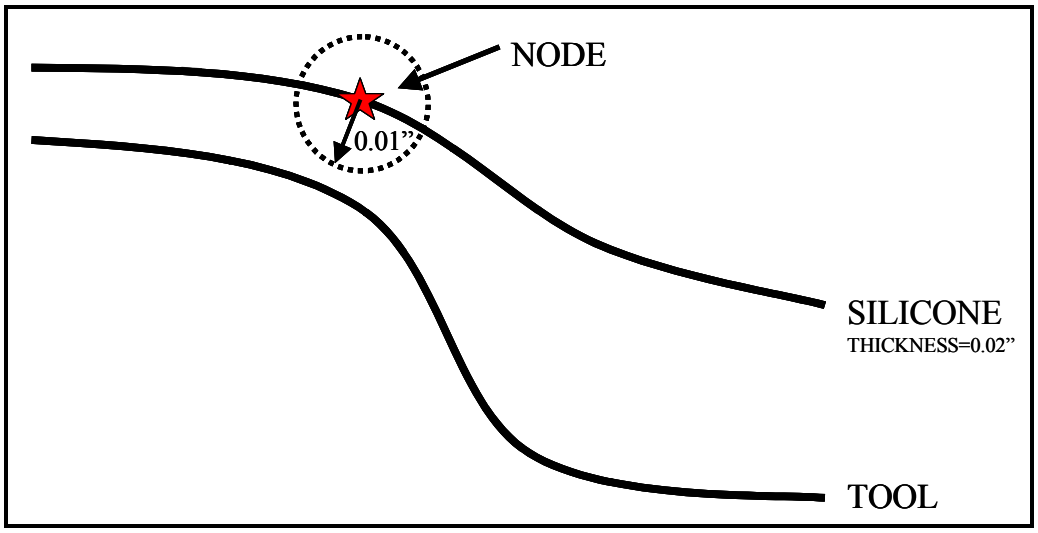

Figure 3.10 Connectivity Search Approach [15]

The contact enforcement used for these interfaces is a penalty contact. The contact enforcement addresses how, if the silicone passes the tool surface, the silicone is moved back away from the tool. This may occur if the movement of the flexible silicone sheet between time steps and search frequency allows it to travel past the tool. The penalty contact works by assessing a penalty value within the contact interface. This penalty value is used to apply a force normal to the tool to force the silicone back from the tool surface.

3.2.6 Loading Conditions

Loading conditions within the RIDFT simulation model are used to apply pressure to the RIDFT model based on a predefined pressure curve to simulate vacuum forming. This loading creates pressure on the fiber compacting it between the two layers of flexible diaphragms and also forces the fiber-silicone assembly over the shape of the tool. The pressure is initially equal and opposite to create fiber compaction, and the bottom pressure is slowly decreased to initiate forming. Figure 3.11 illustrates the pressure curves used for fiber compaction and forming. Following the described steps, a simulation model of the RIDFT process can be developed using the PAMFORM software.

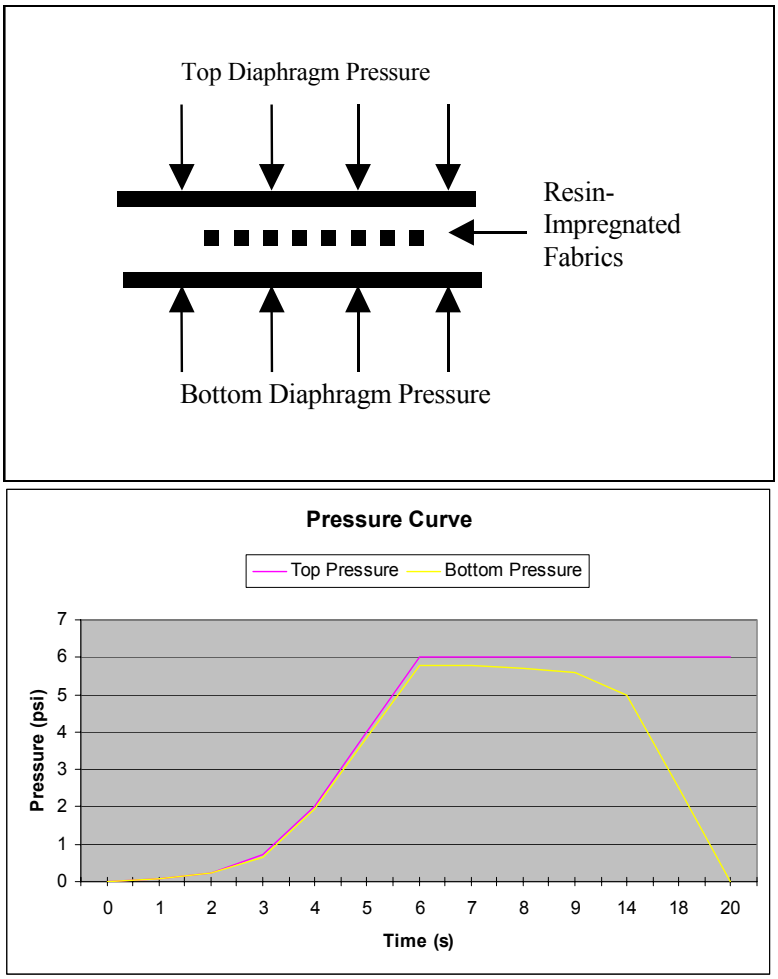

Figure 3.11 Pressure Curves

CHAPTER 4

MATERIAL CHARACTERIZATION

4.1 Friction Testing

The friction testing consists of testing the fabric specimens dry and some of the specimens wet. Within the RIDFT process, the fiber-to-fiber frictions and the fiber-to silicone frictions are derived from wet fiber as the fiber has been infused with resin immediately before forming begins. The silicone-to-silicone and silicone-to-tooling frictions are done dry as resin does not come in contact with the mold surface nor between the silicone layers where fiber is not present. The friction tests for the wet specimens utilize the Derakane 441-440 epoxy vinyl-ester resin system which is actually used in the RIDFT process. Four friction interactions were tested and include the following:

- Silicone to Silicone Contact (dry only).
- Fiber to Fiber Contact (wet only).
- Fiber to Silicone Contact (wet only).
- Silicone to Tool Contact (dry only).

Figure 4.1 illustrates the interactions within the RIDFT process.

The specifications for the four fabrics and the silicone rubber used within the RIDFT process are listed below:

- Saint-Gobain BTI, Inc., CBX400 (0º, 90º), 400g/m^2, non-crimp carbon fiber
- U.S. Composites, Inc., 10oz x 50” fiberglass cloth, 2-FG-c1050, woven glass fiber
- Cofab A1118 (0º, 90º) BIAXIAL, 626 grams/m2, non-crimp glass fiber
- MI-1012, 5.7 oz/yd2, woven carbon fiber
- Bondline Products, Federal Spec ZZ-R-765E/GEN, 0.020” thick, grade 50 class 3B silicone rubber

The specimens were prepared and tested in accordance to the following ASTM standards:

- G115-98 –Standard Guide for Measuring and Reporting Friction Coefficients [16]
- D1894-01 –Standard Test Method for Static and Kinetic Coefficients of Friction of Plastic Film and Sheeting [17]

Although many tests were conducted at various pull rates for the four interactions, friction values derived from a pull rate of 2 inches per minute are used, as this best resembles the friction speeds within the RIDFT process. The coefficient of dynamic friction is calculated by dividing the average friction force, Fr, by the weight of the sled, Fn, for a given stroke interval [20]. Fn for the sled was approximately 7.57 pounds. The stroke interval will begin when the curve becomes stable immediately following the peak force achieved. The initial peak of the force vs. stroke curve is used to calculate the value of static friction. All tests were performed on a SIMAZU ASJ-1 tensile testing machine.

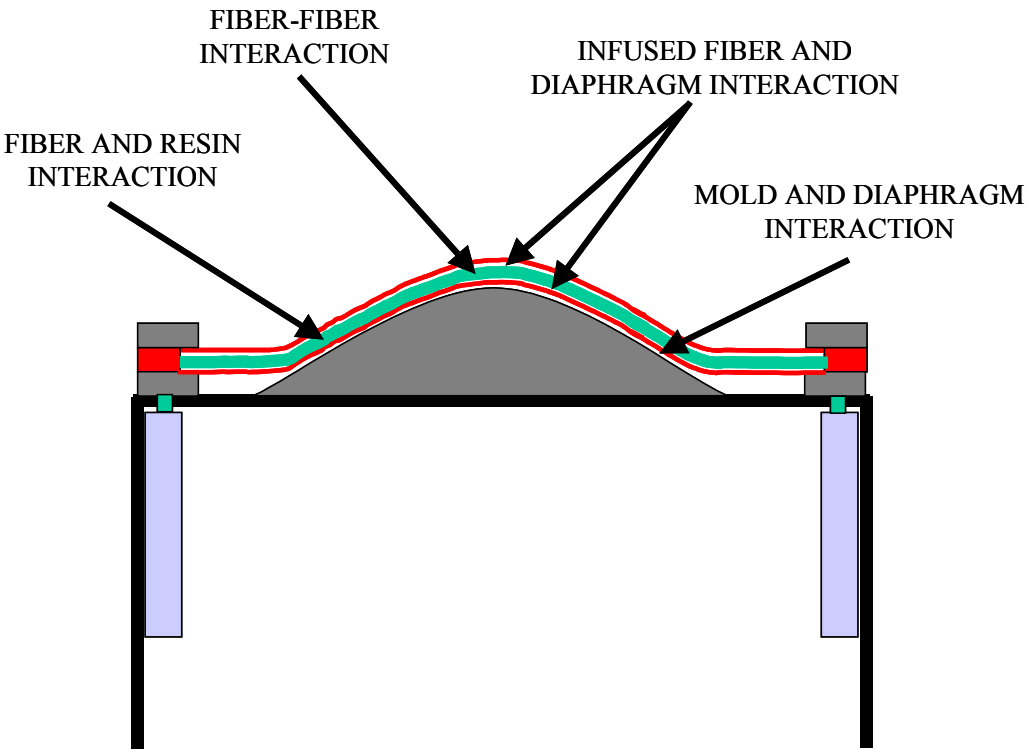

Figure 4.1 RIDFT Friction interactions

4.1.1 Friction Test Rig

The standard governing the friction testing of fibers is D3334-80 (Methods of Testing Fabrics Woven from Polyolefin Monofilament) and was withdrawn in 1990. This friction test method was used for the calculation of coefficient of static friction, whereas the desired friction information used within PAMFORM is the dynamic friction or kinetic friction value.

ASTM D1894-01 used a test rig capable of measuring both static and kinetic friction. This rig consists of a metallic sled of a particular weight, a supporting base, driving device for sled, low friction pulley and steel cable. Figure 4.2 illustrates the design of the test rig. This research has designed and built the test rig for the testing of kinetic friction values used within the RIDFT simulation model. Figure 4.3 illustrates the actual test rig used.

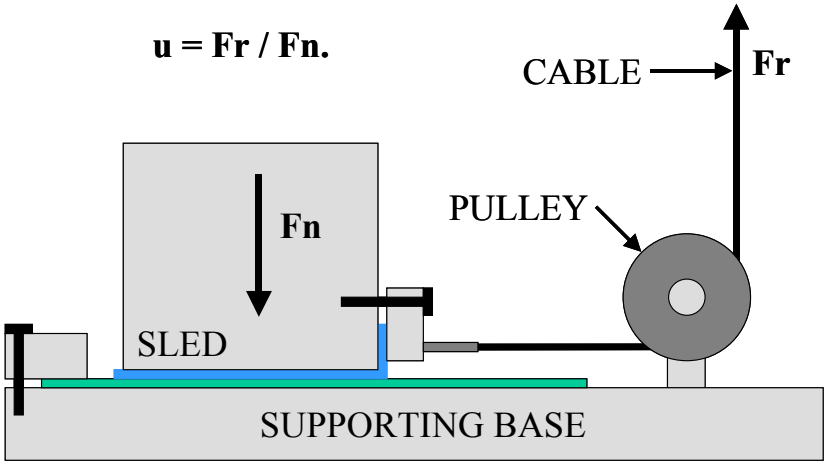

Figure 4.2 Friction Test Rig Design

Figure 4.3 Actual Friction Test Rig

4.1.2 Silicone to Silicone Contact Friction (Dry Only)

The silicone-silicone contact was performed at four different pull rates of 1 inch per minute, 2 inches per minute, 10 inches per minute and 20 inches per minute. Figures 4.4 through 4.7 illustrate the friction curves for the silicone-silicone contact for the various pull rates. For the silicone-to-silicone contact, a value of 1.93 is calculated for the coefficient of kinetic friction from the pull rate of 2 inches per minute. This high value is consistent with the properties of rubber. Rubber exhibits unusual sliding behavior, which is derived from the fact that it is elastically very soft. Furthermore, the area of real contact between rubber and a rough hard substrate is strongly affected by adhesion [20].

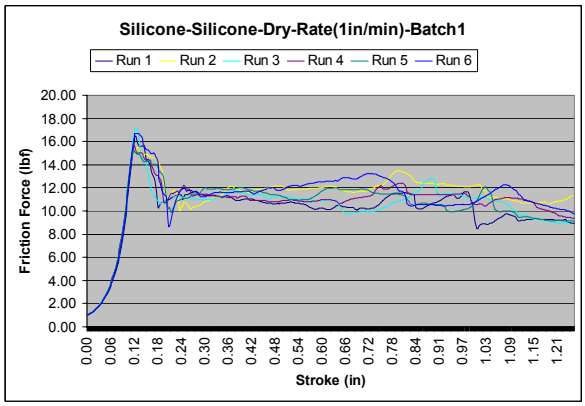

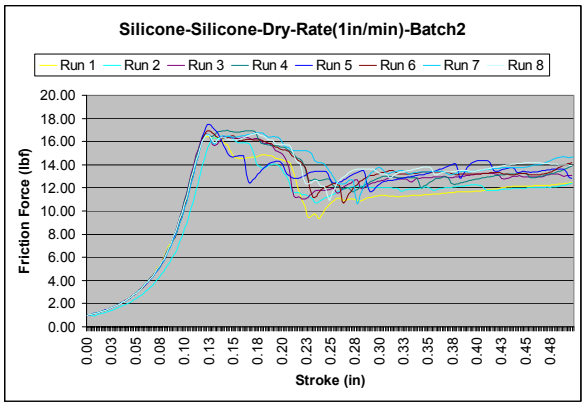

Name	Max_Force			
Parameter			Average Friction Force	
Units	lbf	Coefficient of Static Friction	stroke(.25in - .5in)	Coefficient of Kinetic Friction
1 - 1	16.516	2.182	11.088	1.465
2 - 1	15.499	2.048	11.487	1.518
3 - 1	17.201	2.273	11.272	1.489
4 - 1	15.656	2.069	11.168	1.476
5 - 1	15.195	2.008	11.684	1.544
6 - 1	16.712	2.208	11.662	1.541
Average		2.131	11.394	1.505

Name	Max_Force			
Parameter			Average Friction Force	
Units	lbf	Coefficient of Static Friction	stroke(.3in - .5in)	Coefficient of Kinetic Friction
1 - 1	16.426	2.170	11.775	1.556
2 - 1	16.476	2.177	12.006	1.586
3 - 1	16.662	2.202	12.961	1.713
4 - 1	16.965	2.242	12.924	1.708
5 - 1	17.493	2.311	13.419	1.773
6 - 1	16.915	2.235	13.313	1.759
7 - 1	16.757	2.214	13.678	1.807
8 - 1	16.684	2.205	13.679	1.807
Average		2.220	12.969	1.714

Figure 4.4 Silicone-Silicone Friction (Rate 1 in/min)

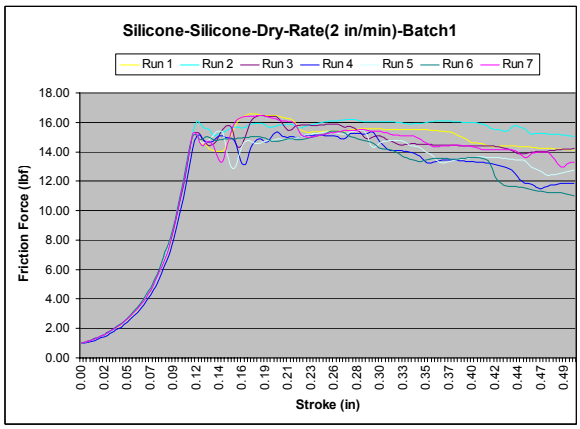

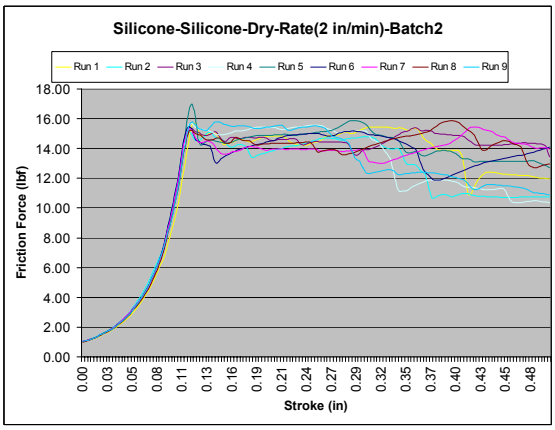

Name Parameter Units	Max_Force lbf	Coefficient of Static Friction	Average Friction Force stroke(.25in - .4in)	Coefficient of Kinetic Friction
1 - 1	16.589	2.192	15.353	2.029
2 - 1	16.212	2.142	16.041	2.120
3 - 1	16.465	2.176	14.846	1.962
4 - 1	15.341	2.027	14.148	1.870
5 - 1	15.470	2.044	14.372	1.899
6 - 1	15.431	2.039	14.104	1.864
7 - 1	16.443	2.173	14.937	1.974
Average		2.113	14.829	1.959

Name Parameter Units	Max_Force lbf	Coefficient of Static Friction	Average Friction Force stroke(.15in - .3in)	Coefficient of Kinetic Friction
1 - 1	15.684	2.072	14.699	1.942
2 - 1	15.167	2.004	14.286	1.888
3 - 1	15.403	2.035	14.449	1.909
4 - 1	15.712	2.076	15.292	2.021
5 - 1	16.988	2.245	15.060	1.990
6 - 1	15.504	2.049	14.640	1.934
7 - 1	15.459	2.043	13.876	1.834
8 - 1	15.875	2.098	14.190	1.875
9 - 1	15.802	2.088	15.002	1.982
Average		2.079	14.611	1.931

Figure 4.5 Silicone-Silicone Friction (Rate 2 in/min)

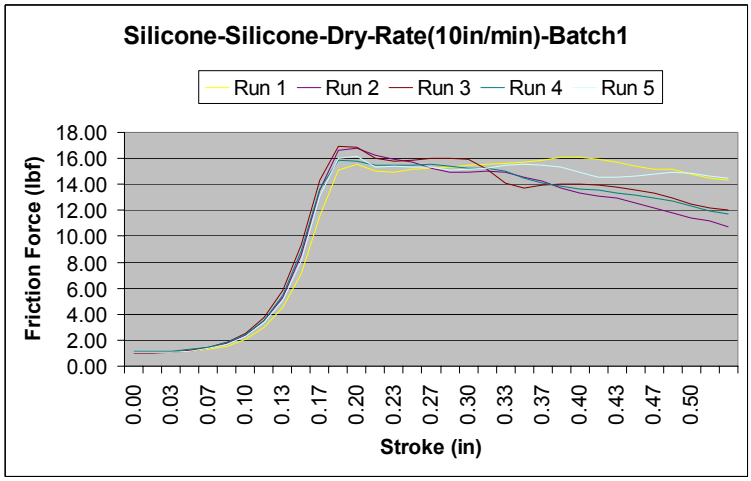

Name Parameter Units	Max_Force lbf	Coefficient of Static Friction	Average Friction Force stroke(.25in - .35in)	Coefficient of Kinetic Friction
1 - 1	16.072	2.124	15.723	2.078
2 - 1	16.774	2.216	14.616	1.931
3 - 1	16.920	2.236	14.693	1.942
4 - 1	15.841	2.093	14.657	1.937
5 - 1	16.150	2.134	15.369	2.031
Average		2.161	15.012	1.984

Figure 4.6 Silicone-Silicone Friction (Rate 10 in/min)

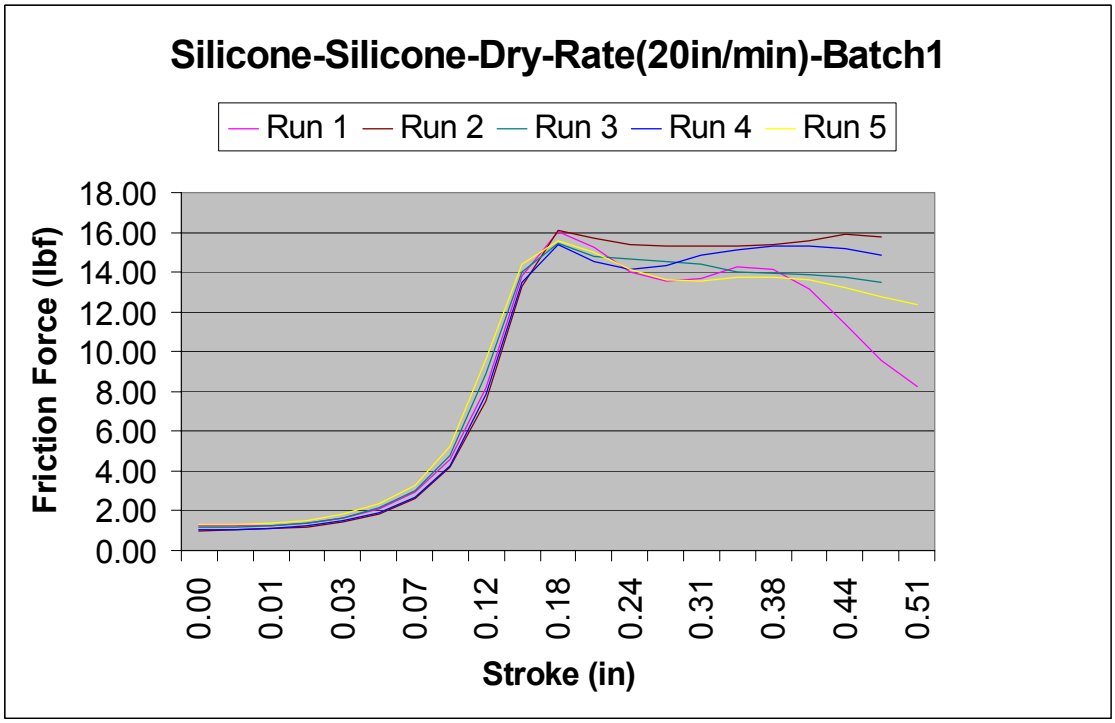

Name	Max_Force			
Parameter			Average Friction Force	
Units	lbf	Coefficient of Static Friction	Stroke(.25in - .4in)	Coefficient of Kinetic Friction
1 - 1	16.049	2.121	13.798	1.823
2 - 1	16.083	2.125	15.334	2.026
3 - 1	15.454	2.042	14.246	1.882
4 - 1	15.352	2.029	14.863	1.964
5 - 1	15.555	2.055	13.720	1.813
Average		2.074	14.392	1.902

Figure 4.7 Silicone-Silicone Friction (Rate 20 in/min)

4.1.3 Fiber to Fiber Contact Friction (Wet Only)

The fiber-fiber contact was performed at two different pull rates of either 2 inch per minute or 20 inches per minute for the plain weave carbon and a rate of 2 inches per minute for the non-crimp carbon. Figures 4.8 and 4.9 illustrate the friction curves for the plain weave carbon to plain weave carbon contact for pull rates of 2 inches per minute and 20 inches per minute. Figure 4.10 illustrates the friction curves for the non-crimp carbon. For the plain weave carbon fabric a coefficient of kinetic friction value of 0.261 is obtain and a value of 0.365 is obtained for the non-crimp carbon fabric. Figure 4.11 illustrates the friction curves for the non-crimp glass to non-crimp glass interface.

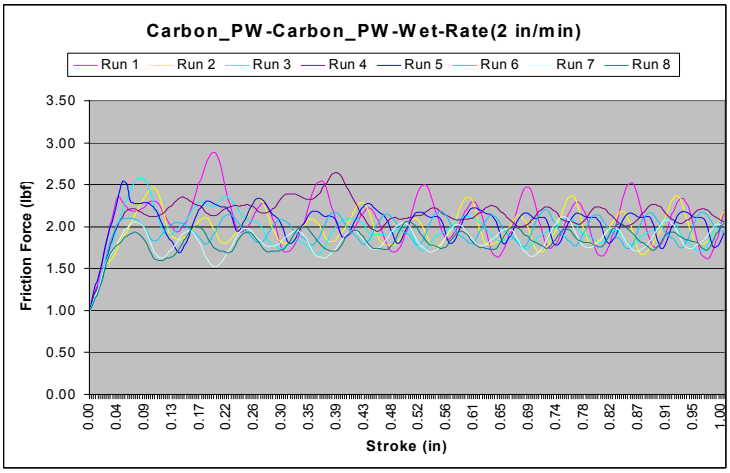

Name	Max_Force			
Parameter			Average Friction Force	
Units	lbf	Coefficient of Static Friction	stroke(.5in - 1in)	Coefficient of Kinetic Friction
1 - 1	2.885	0.381	2.050	0.271
2 - 1	2.466	0.326	1.987	0.262
3 - 1	2.578	0.341	1.916	0.253
4 - 1	2.643	0.349	2.131	0.282
5 - 1	2.201	0.291	1.966	0.260
6 - 1	2.119	0.280	1.873	0.247
7 - 1	2.062	0.273	1.858	0.246
8 - 1	2.545	0.336	2.034	0.269
Average		0.322	1.977	0.261

Figure 4.8 Plain Weave Carbon to Plain Weave Carbon Friction (Rate 2 in/min)

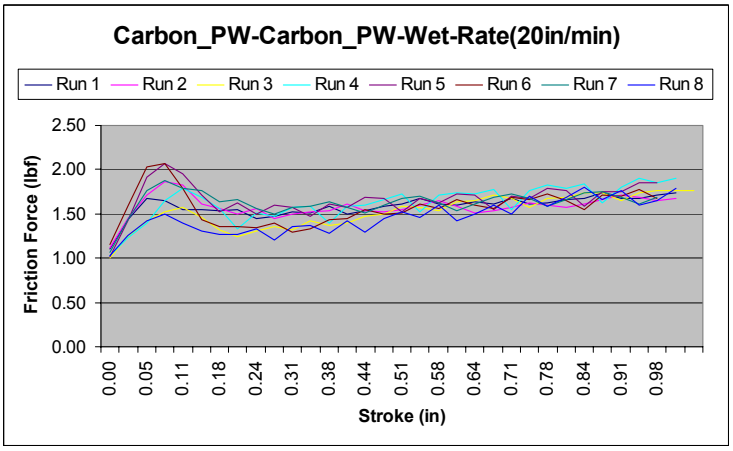

Name				
Parameter	Max_Force		Average Friction Force	
Units	lbf	Coefficient of Static Friction	stroke(.5in - 1in)	Coefficient of Kinetic Friction
1 - 1	1.742	0.230	1.659	0.219
2 - 1	1.869	0.247	1.617	0.214
3 - 1	1.770	0.234	1.681	0.222
4 - 1	1.907	0.252	1.754	0.232
5 - 1	2.071	0.274	1.703	0.225
6 - 1	2.064	0.273	1.645	0.217
7 - 1	1.872	0.247	1.664	0.220
8 - 1	1.797	0.237	1.614	0.213
Average		0.249	1.667	0.220

Figure 4.9 Plain Weave Carbon to Plain Weave Carbon Friction (Rate 20 in/min)

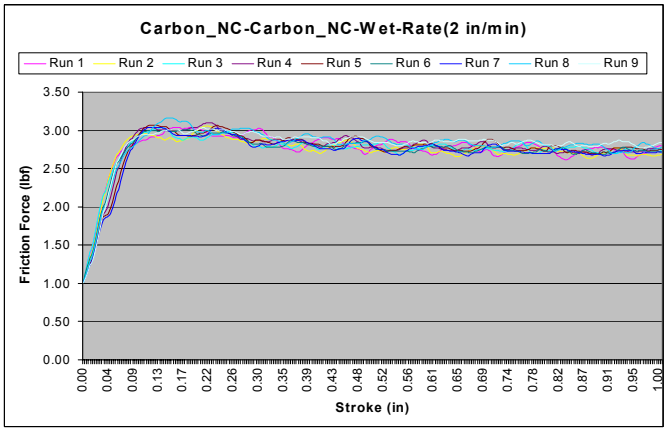

Name	Max_Force			
Parameter			Average Friction Force	
Units	lbf	Coefficient of Static Friction	stroke(.5in - 1in)	Coefficient of Kinetic Friction
1 - 1	3.040	0.402	2.752	0.364
2 - 1	3.056	0.404	2.723	0.360
3 - 1	3.035	0.401	2.754	0.364
4 - 1	3.101	0.410	2.756	0.364
5 - 1	3.072	0.406	2.761	0.365
6 - 1	3.008	0.397	2.738	0.362
7 - 1	3.040	0.402	2.728	0.361
8 - 1	3.162	0.418	2.809	0.371
9 - 1	3.032	0.401	2.833	0.374
Average		0.404	2.762	0.365

Figure 4.10 Non-Crimp Carbon to Non-Crimp Carbon Friction (Rate 2 in/min)

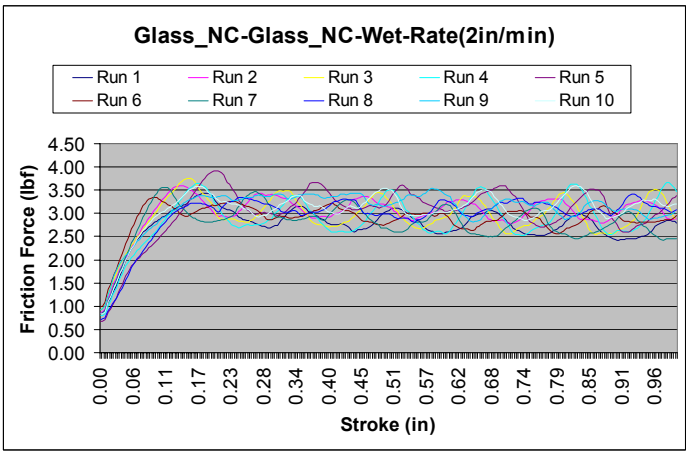

Name	Max_Force			
Parameter			Average Friction Force	
Units	lbf	Coefficient of Static Friction	stroke(.5in - 1in)	Coefficient of Kinetic Friction
1 - 1	3.438	0.454	2.737	0.362
2 - 1	3.587	0.474	3.046	0.403
3 - 1	3.759	0.497	2.964	0.392
4 - 1	3.657	0.483	2.992	0.395
5 - 1	3.917	0.518	3.146	0.416
6 - 1	3.347	0.442	2.871	0.379
7 - 1	3.564	0.471	2.734	0.361
8 - 1	3.422	0.452	3.104	0.410
9 - 1	3.535	0.467	3.144	0.415
10 - 1	3.592	0.475	3.160	0.418
Average		0.473	2.990	0.395

Figure 4.11 Non-Crimp Glass to Non-Crimp Glass Friction (Rate 2 in/min)

4.1.4 Silicone-to-Fiber Contact Friction (Wet Only)

The silicone-fiber contact was performed at two different pull rates of either 2 inch per minute or 10 inches per minute for the plain weave carbon and a rate of 2 inches per minute for the non-crimp carbon for both the parallel and perpendicular fiber orientation. Figures 4.12 and 4.13 illustrate the friction curves for the silicone to plain weave carbon contact and silicone to non-crimp glass contact, respectively for pull rates of 2 inches per minute. Figures 4.14 and 4.15 illustrate the friction curves for the non-crimp carbon at a rate of 2 inches per minute for the parallel and perpendicular orientations.

For the silicone to plain weave carbon contact interface a coefficient of kinetic friction value of 0.215 is calculated. For the silicone to non-crimp carbon (perpendicular) and silicone to non-crimp carbon (parallel) contact interfaces the coefficient of kinetic friction values of 0.299 and 0.244 respectively, are calculated. The parallel and perpendicular orientation of the fiber is with respect to the sled pulling direction.

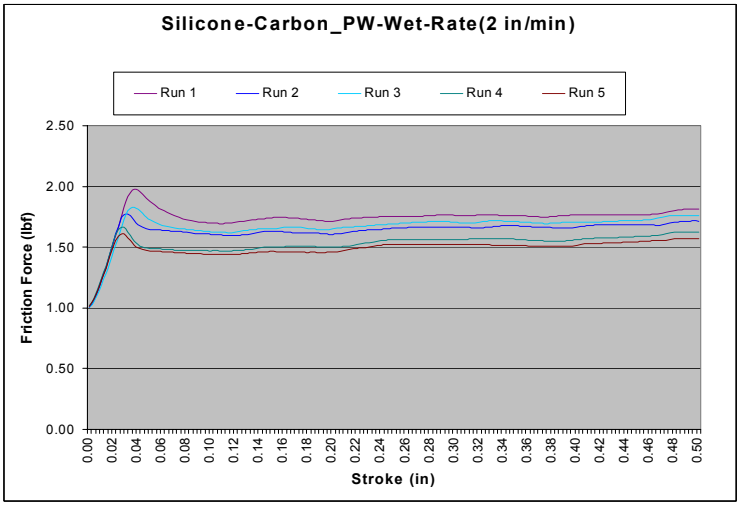

Name	Max_Force		Average Friction Force	
Parameter				
Units	lbf	Coefficient of Static Friction	Stroke(.1in - .5in)	Coefficient of Kinetic Friction
1 - 1	1.975	0.261	1.752	0.231
2 - 1	1.775	0.234	1.654	0.219
3 - 1	1.829	0.242	1.692	0.224
4 - 1	1.664	0.220	1.548	0.205
5 - 1	1.607	0.212	1.506	0.199
Average		0.234	1.630	0.215

Figure 4.12 Silicone to Plain Weave Carbon Friction (Rate 2 in/min)

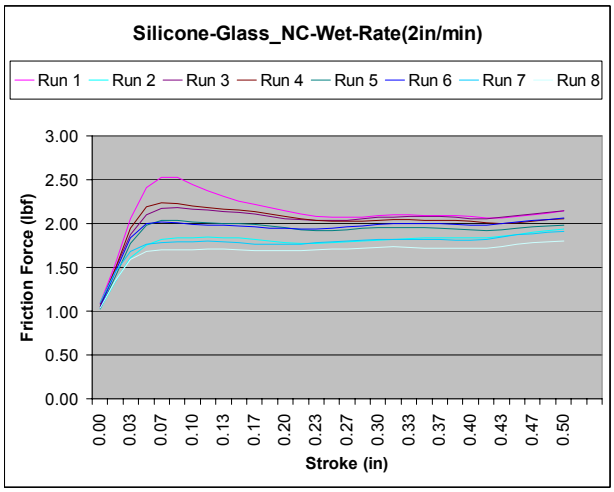

Name	Max_Force			
Parameter			Average Friction Force	
Units	lbf	Coefficient of Static Friction	stroke(.25in - .5in)	Coefficient of Kinetic Friction
1 - 1	2.530	0.334	2.089	0.276
2 - 1	1.935	0.256	1.843	0.244
3 - 1	2.179	0.288	2.078	0.275
4 - 1	2.233	0.295	2.030	0.268
5 - 1	2.035	0.269	1.945	0.257
6 - 1	2.061	0.272	1.999	0.264
7 - 1	1.909	0.252	1.834	0.242
8 - 1	1.802	0.238	1.737	0.230
Average		0.276	1.944	0.257

Figure 4.13 Silicone to Non-Crimp Glass Friction (Rate 2 in/min)

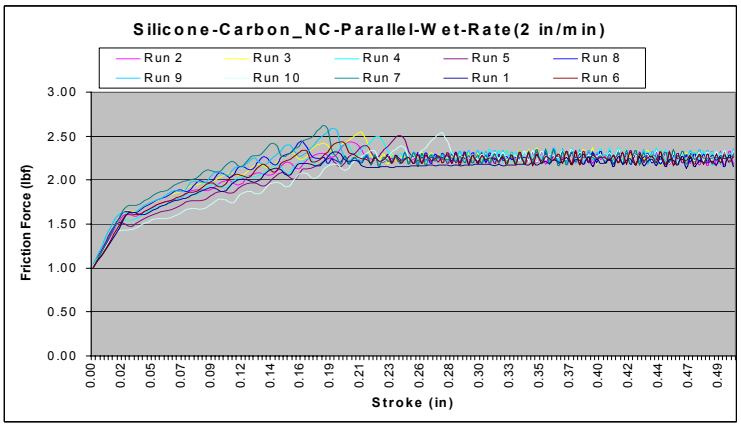

Name	Max_Force			
Parameter			Average Friction Force	
Units	lbf	Coefficient of Static Friction	Stroke(.3in - .5in)	Coefficient of Kinetic Friction
1 - 1	2.319	0.306	2.200	0.291
2 - 1	2.431	0.321	2.251	0.297
3 - 1	2.542	0.336	2.269	0.300
4 - 1	2.494	0.330	2.279	0.301
5 - 1	2.505	0.331	2.254	0.298
6 - 1	2.437	0.322	2.244	0.296
7 - 1	2.624	0.347	2.255	0.298
8 - 1	2.444	0.323	2.256	0.298
9 - 1	2.588	0.342	2.270	0.300
10 - 1	2.533	0.335	2.271	0.300
Average		0.329	2.255	0.299

Figure 4.14 Silicone to Non-Crimp Carbon (Parallel) Friction (Rate 2 in/min)

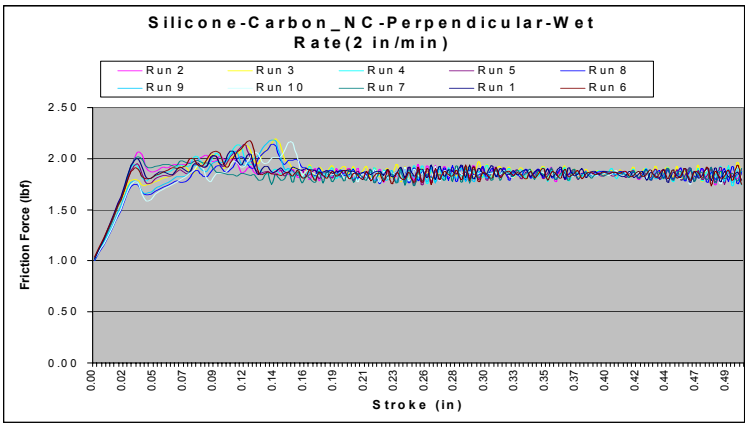

Name Parameter Units	Max_Force lbf	Coefficient of Static Friction	Average Friction Force Stroke(.2in - .5in)	Coefficient of Kinetic Friction
1 - 1	2.072	0.274	1.857	0.245
2 - 1	2.070	0.273	1.852	0.245
3 - 1	2.198	0.290	1.866	0.247
4 - 1	2.132	0.282	1.849	0.244
5 - 1	2.135	0.282	1.843	0.244
6 - 1	2.176	0.288	1.843	0.244
7 - 1	2.020	0.267	1.838	0.243
8 - 1	2.142	0.283	1.847	0.244
9 - 1	2.180	0.288	1.841	0.243
10 - 1	2.164	0.286	1.842	0.243
Average		**0.281**	**1.848**	**0.244**

Figure 4.15 Silicone to Non-Crimp Carbon (Perpendicular) Friction (Rate 2in/min)

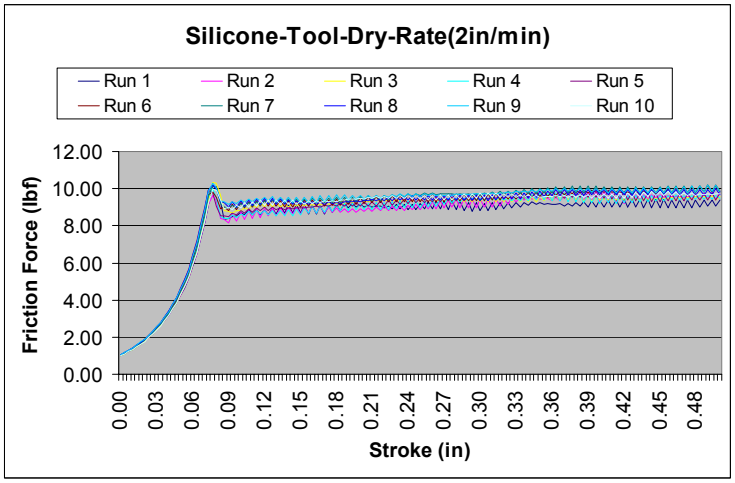

Name Parameter Units	Max_Force lbf	Coefficient of Static Friction	Average Friction Force stroke(.25in - .5in)	Coefficient of Kinetic Friction
1 - 1	10.127	1.338	9.156	1.210
2 - 1	9.855	1.302	9.425	1.245
3 - 1	10.336	1.366	9.450	1.249
4 - 1	9.989	1.320	9.454	1.249
5 - 1	9.919	1.311	9.559	1.263
6 - 1	10.221	1.351	9.734	1.286
7 - 1	10.186	1.346	9.864	1.303
8 - 1	10.213	1.349	9.697	1.281
9 - 1	10.275	1.358	9.855	1.302
10 - 1	9.945	1.314	9.627	1.272
Average		**1.335**	**9.582**	**1.266**

Figure 4.16 Silicone to Tool Friction (Rate 2in/min)

4.1.5 Silicone-Tool Contact Friction (Dry Only)

The silicone-tool contact was performed at a single pull rate of 2 inches per minute. Figure 4.16 illustrates the friction curves for the silicone to tool contact for a pull rate of 2 inches per minute. For this test a coefficient of static friction was calculated to be 1.335 and the coefficient of dynamic friction was calculated to be 1.266.

4.1.6 Friction Test Summary

The data obtained for the coefficients of kinetic friction will be used as a direct input for the contact interface within the simulation model. The results for the various test showed repeatability and a clearly defined sustaining force used to define the kinetic friction. The silicone-to-silicone results show high friction values that coincide with the friction properties of rubber [20].

The initial peak force within the graph is used to calculate the coefficient of static friction. The initial force to begin the sled in motion is higher than the force required to sustain that motion. However, the simulation model only requires the coefficient of kinetic friction to be used. The variations of the sled rate were used to understand the effects of forming speeds on the coefficient of kinetic friction. Although small variations exist between the various rates for the friction coefficient value, a rate of 2 inches per minute best reflects conditions within the RIDFT process.

The plain weave carbon to plain weave carbon contact showed a much lower coefficient of kinetic friction as compared to the non-crimp carbon to non-crimp carbon contact, 0.261 and 0.365 respectively. These results are consistent with the fabric surface structure. The woven carbon fiber has a much smoother surface as compared to the course surface of the non-crimp carbon fabric. It is also believe the stitching used within the non-crimp carbon fabric may cause additional surface agitation. The non-crimp glass fabric to non-crimp glass fabric friction was shown to be higher than that of the non-crimp carbon fabric to non-crimp carbon fabric friction, 0.395 and 0.365, respectively. Table 4.1 defines the results of the friction testing.

Table 4.1 Friction Results Summary

Contact Interface	Rate (in/min)	Coefficient of Static Friction DRY	Coefficient of Static Friction WET	Coefficient of Dynamic Friction DRY	Coefficient of Dynamic Friction WET
Carbon(NC)-Carbon(NC)	2	NO DATA	0.404	NO DATA	0.365
Carbon(PW)-Carbon(PW)	2	0.410	0.322	0.303	0.261
Carbon(PW)-Carbon(PW)	10	0.401	NO DATA	0.299	NO DATA
Carbon(PW)-Carbon(PW)	20	0.360	0.249	0.314	0.220
Silicone-Carbon(NC)-Parallel	2	NO DATA	0.329	NO DATA	0.299
Silicone-Carbon(NC)-Perpendicular	2	NO DATA	0.281	NO DATA	0.244
Silicone-Carbon(PW)	2	0.682	0.234	0.662	0.215
Silicone-Carbon(PW)	20	0.879	NO DATA	0.871	NO DATA
Silicone-Glass(NC)	2	0.734	0.276	0.711	0.257
Silicone-Silicone-Batch1	1	2.131	NO DATA	1.505	NO DATA
Silicone-Silicone-Batch2	1	2.220	NO DATA	1.714	NO DATA
Silicone-Silicone-Batch1	2	2.120	NO DATA	1.914	NO DATA
Silicone-Silicone-Batch2	2	2.079	NO DATA	1.931	NO DATA
Silicone-Silicone	10	2.161	NO DATA	1.984	NO DATA
Silicone-Silicone	20	2.074	NO DATA	1.902	NO DATA
Silicone-Tooling	2	1.355	NO DATA	1.266	NO DATA
Glass(NC)-Glass(NC)	2	NO DATA	0.473	NO DATA	0.395

4.2 Silicone Testing

The material model *Type 121 for the Flexible Silicone Sheets* is characterized as nonlinear thermo-visco-elastic for shell elements (G'Sell Model). Inputs for this material model include initial thickness, Young's Modulus, Poisson's Ratio and mass density. The governing equation used within the PAMFORM software is listed in Equation 4.1 [14].

$$\sigma = k(1-\exp(-\omega\varepsilon)) \times (\exp(h\varepsilon^2))\varepsilon^m \qquad \text{Equation (4.1)}$$

where,

σ = stress,

ε = strain,

k = scaling factor (162.496psi),

m = strain rate hardening exp (0.095),

h = strain hardening coefficient (1.669) and

ω = visco-elastic coefficient (3.691).

The silicone testing consists of tensile measurements taken at three different strain rates. The silicone specimens are prepared and tested in accordance to the following ASTM standards:

- D412-98a(2002)e1 –Standard Test Methods for Vulcanized Rubber and Thermoplastic Elastomers—Tension [18]
- D3183-02 –Standard Practice for Rubber—Preparation of Pieces for Test Purposes from Products [19]

The initial strain rate is selected based on the approximate strain rate used within the RIDFT process. This was determined by taking two points on the silicone of the RIDFT machine and the strain rate measured during the forming process. For the RIDFT process, a strain rate of 2 inches/minute is approximated. The other two strain rates are based on 25 percent (.5 inches/minute) of the optimal strain rate and 250 percent (5 inches/minute) of the optimal strain rate. Figure 4.17 illustrates the silicone specimen being tested and the stress vs. strain curves for the three strain rates tested. From Figure 4.17, the silicone appears to be strain rate independent. For the optimal strain rate of 2 inches/minute, the data is fit to Equation 4.1 using nonlinear curve fitting. This allows for the desired material parameters to be obtained for use within the RIDFT simulation model.

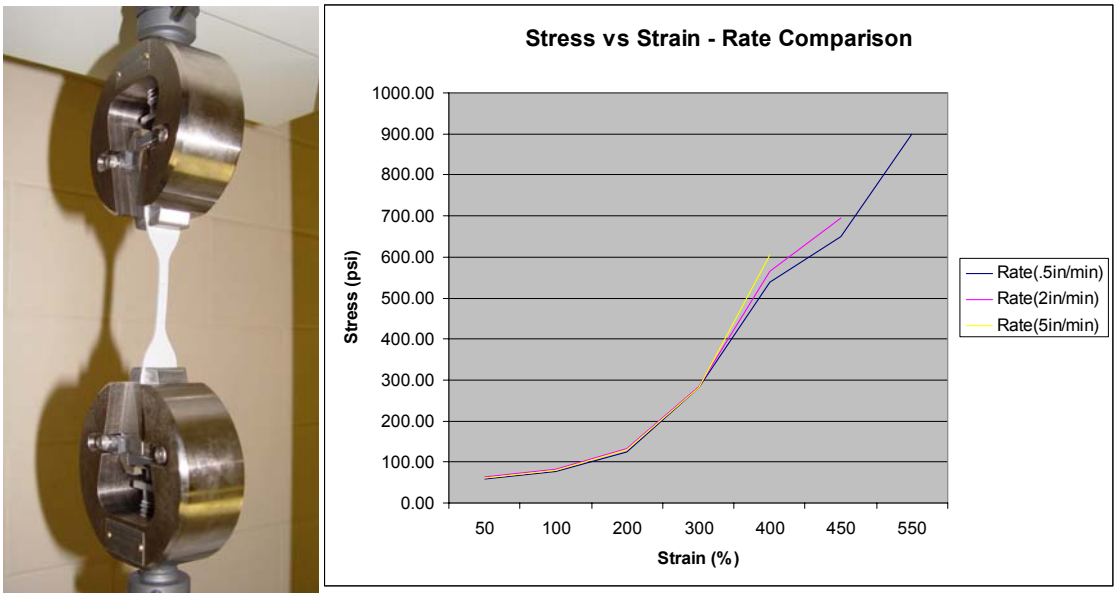

Figure 4.17 Stress vs. Strain Rate Comparisons

4.3 Fiber Testing

The purpose of materials test are to obtain the drapability information of fiber fabrics for modeling of process forming. The materials testing consists of three major tasks that include picture frame shear testing for both dry and resin impregnated fabrics, tensile coupon testing and fabric thickness measurement for use in stress calculations.

The tensile tests and resin impregnated picture frame tests utilize Derakane 441-440 epoxy vinyl-ester resin system. Four biaxial fabrics were tested and include the following:

- Saint-Gobain BTI, Inc., CBX400 (0º, 90º), 400g/m^2, non-crimp carbon fiber
- U.S. Composites, Inc., 10oz x 50" fiberglass cloth, 2-FG-c1050, woven glass fiber
- Cofab A1118 (0º, 90º) BIAXIAL, 626 grams/m2, non-crimp glass fiber
- MI-1012, 5.7 oz/yd2, woven carbon fiber

All testing was conducted by Professor Anthony Pickett at the School of Industrial and Manufacturing Science at Cranfield University, Cranfield, Bedford, MK43 0AL, England.

4.3.1 Picture Frame Test

The picture frame test is used to characterize fabric shear behavior and imposes pure shear within the test specimen. The picture frame test is illustrated in Figure 4.18. A rhomboid deformation cell is extended at diagonally opposing corners at a constant displacement rate of 10 millimeters per minute for dry fabric tests and 200 millimeters per minute for resin impregnated fabric tests. The increased displacement rate is necessary as the resin is manually applied to the specimen. The increased rate allows for shorter test times as to not negate the resin effects on the test results.

Although the resistance to intra-ply shear in dry fabrics is not subject to time dependant behavior [21,22] the resin systems are and as such require a constant shear rate for optimum fabric characterization. As a basis for calibrating simulation input parameters the use of a constant displacement rate is sufficient.

The material specimen is clamped at each edge of the frame with fabric fibers aligned to the frame edges. Misalignment of these fibers results in fiber extension during shear and, due to the relatively high fiber elastic modulus, is the main cause of error and data scatter in the test. A schematic of the picture frame fabric specimen is shown in figure 4.19, indicating the direction

of crosshead displacement. Where required, resin is manually applied to the fabric by brush for simulating the actual forming situation of RIDFT.

Figure 4.18 Picture Frame Test Equipment

The angular shear rate (ø) can be calculated using equation 4.2 [22].

$$\dot{\phi} = \frac{2\dot{D}}{(2L^2 - 2\sqrt{2}LD - D^2)^{1/2}} = \frac{\dot{D}}{L.\sin\theta} \qquad \text{Equation (4.2)}$$

where,

D = frame displacement rate,

θ = internal frame angle and

L = frame length as illustrated.

Figure 4.19 illustrates the schematic of the picture frame test specimen. Three tests are conducted for each of the four fabrics in both dry and resin impregnated states. Analyzed data plots the mean average force data at the required shear angle with error bars calculated using a student T-test. This analysis assumes the data approximates to a normal distribution of unknown variance. The confidence interval for this analysis is 90%.

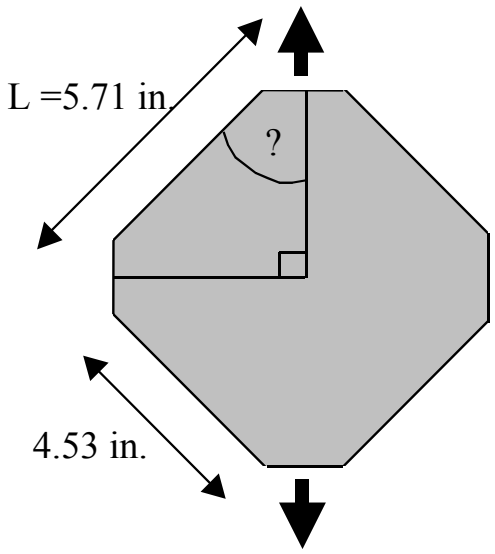

Figure 4.19 Schematic of the Picture Frame Test Specimen

Force verses displacement data is additionally analyzed to produce graphs of shear stress verses shear strain. The shear stress (σ) is calculated as using equation 4.2.

$$\sigma = \frac{F}{L.T} \qquad \text{Equation (4.2)}$$

where,

F = measured force,

L = frame edge length and

T = fabric thickness.

The initial fabric thickness has been used in all calculations for simplicity. Accurate thickness data can be obtained experimentally or alternatively the thickness can be increased as a

function of shear angle under the assumption of volume conservation, increasing by $1/\cos\phi$. This assumption of volume conservation is currently utilized in the material 140 shell element formulation available for composite draping simulation in PAMFORM.

The shear strain is calculated using Equation 4.3 [14].

$$\varepsilon = 0.5.\sin\phi \qquad \text{Equation (4.3)}$$

where, ϕ is the shear angle. In addition to shear data, locking angle data is taken at the onset of out-of-plane deformation within the fabric (i.e. wrinkling) during the picture frame tests. The crosshead displacement of the testing machine is noted at the visual on-set of locking and converted to a shear angle. Measurement accuracy is +/- 0.02 inches.

4.3.2 Tensile Coupon Testing

Tensile coupon testing is used to characterize the in-plane properties of the fabric. Tests are conducted with strain parallel to the fiber orientation. A schematic of the specimen is shown in Figure 4.20. Strain is induced at a constant displacement rate of 2.5 millimeters per minute. The strain rate can therefore be considered quasi-static at $1.67\text{x}10^{-4}\ s^{-1}$. The resin is manually applied to the fabric by brush.

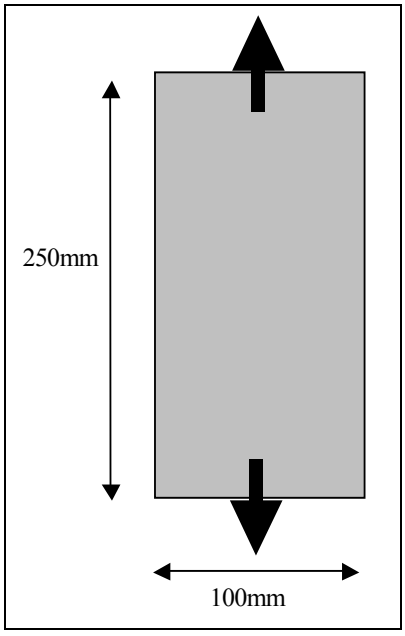

Figure 4.20 Schematic of the Tensile Test Specimen

4.3.3 Fabric Thickness Testing

Fabric thickness is required for use in calculation of the shear stress produced during picture frame tests. A simple technique has been employed to obtain the data, using Venire calipers to measure the thickness of ten stacked, dry fabric sheets. This, in addition to taking the mean average of ten separate readings over the stack, permits a single sheet thickness to be calculated of increased accuracy compared to measurements of a single fabric sheet. Table 4.2 illustrates the results of the fabric thickness measurements.

Table 4.2 Fabric Thickness Measurements

Measuring 10 stacked fabric layers using Vernier callipers				
Fabric type	Glass NCF	Plain weave glass fabric	Plain weave Carbon fabric	Carbon NCF
10 Layer thickness Data (mm)	6.78	2.99	3.28	7.74
	6.45	2.92	3.24	7.64
	6.66	2.97	3.19	7.79
	6.7	2.97	3.27	7.83
	6.65	2.97	3.25	7.89
	6.73	2.93	3.2	7.73
	6.64	2.9	3.26	7.93
	6.65	2.91	3.21	7.84
	6.55	2.91	3.22	7.89
	6.51	2.95	3.21	7.84
10 layer mean average (mm)	6.63	2.94	3.23	7.81
Single layer average thickness (mm)	**0.66**	**0.29**	**0.32**	**0.78**

4.3.4 Results of Picture Frame Locking Angle Measurements

Table 4.3 lists the results of the picture frame locking angle measurements. The method for calculating the locking angle is defined in Equation 2.6. From this table there is an increase in the average shear locking angle when going from dry fabric to resin impregnated fabric. For the woven glass fabric, woven carbon fabric and non-crimp carbon fabric there is an increase of 4.1, 9.5 and 2.1 degrees respectively. However, for the non-crimp glass fabric there was no reported increase in average shear locking angle.

Table 4.3 Picture Frame Locking Angle Measurements

Picture Frame locking angle data Measured at the onset of out-of-plane buckling				
	DRY FABRIC DATA			
Fabric type	Glass NCF	Glass Woven	Carbon Woven	Carbon NCF
Crosshead displacement at locking (mm) (+/- 0.5mm)	73 72 74	70 69.5 69	71.5 72 72	76 75 75.5
Average (mm)	73.0	69.5	71.8	75.5
Average shear locking angle (°)	**57.0**	**52.4**	**55.4**	**60.7**
	RESIN IMPREGNATED FABRIC DATA			
Fabric type	Glass NCF	Glass Woven	Carbon Woven	Carbon NCF
Crosshead displacement at locking (mm) (+/- 0.5mm)	73 73 73	72 73 73	79 78 77	77 76 77.5
Average (mm)	73.0	72.7	78.0	76.8
Average shear locking angle (°)	**57.0**	**56.5**	**64.9**	**62.8**

4.3.5 Results of Picture Frame Testing

Figures 4.21-4.28 illustrate the picture frame test results for the various fabrics. From these figures is seen an increase in force corresponds with an increase in the fabric shear angle. Once the fabric shear angle exceeds 50 degrees, the force begins to increase. This is consistent with the picture frame results for the fabric shear locking angle. Once the locking angle is reached for the fabric tested, a large increase in force occurs corresponding to the post locking shear modulus. This post locking force is called the post locking shear modulus within the simulation model. Table 4.4 lists the results of the picture frame testing used within the RIDFT simulation model.

Table 4.4 Picture Frame Locking Angle Measurements of Resin-Wetted Fabrics

Fiber Property	Carbon non-crimp	Carbon plain weave	Glass non-crimp	Glass plain weave
Shear Modulus (psi)	11.02	15.95	7.397	24.66
Locking Angle	62.8	64.9	57	56.5
Post-Locking Shear Modulus (psi)	11.02	18.13	8.122	92.84

From Table 4.4 the plain weave carbon fiber has the ability to reach a higher locking angle as compared to the other fibers. The non-crimp carbon, non-crimp glass and plain weave glass rank 2nd, 3rd and 4th, respectively in the highest locking angle achieved. However, the plain weave carbon ranks 3rd in the amount of force required to sustain shear with the plain weave glass requiring the most force to sustain shear. The non-crimp fabrics require the least amount of force to sustain shear. The Young's modulus of the fiber is very high in comparison with the forces pulling on the fiber within the RIDFT process and because so the effects of fiber tensile properties are negligible. Therefore, plain weave carbon fabric could be considered the best drapable fabric of the selected four fabrics.

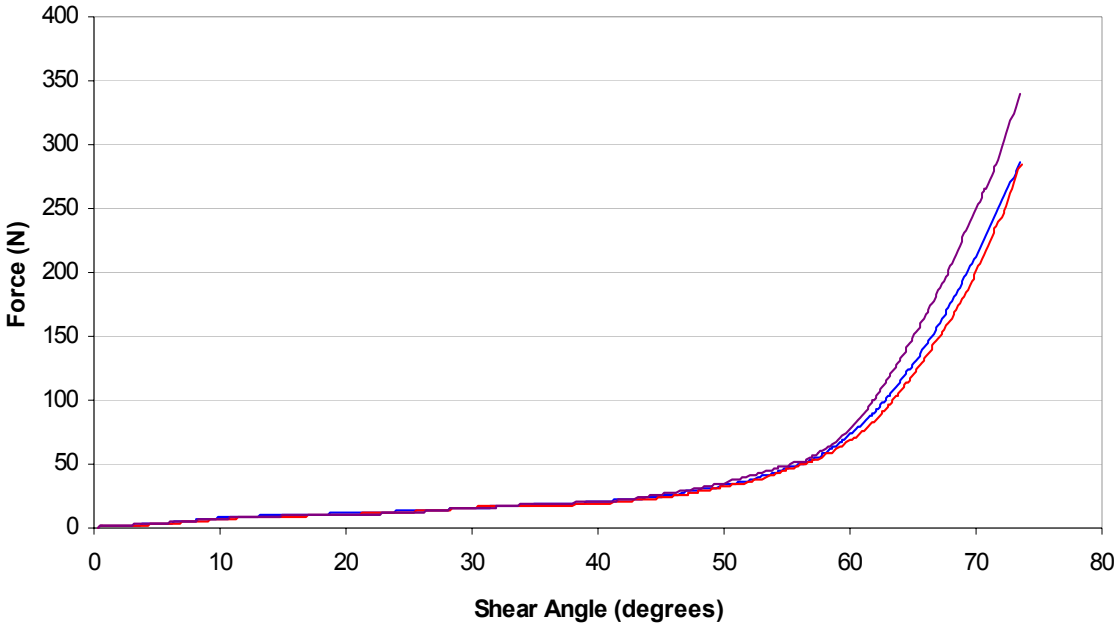

Figure 4.21 Resin Impregnated Non-Crimp Carbon Fabric Picture Frame Results

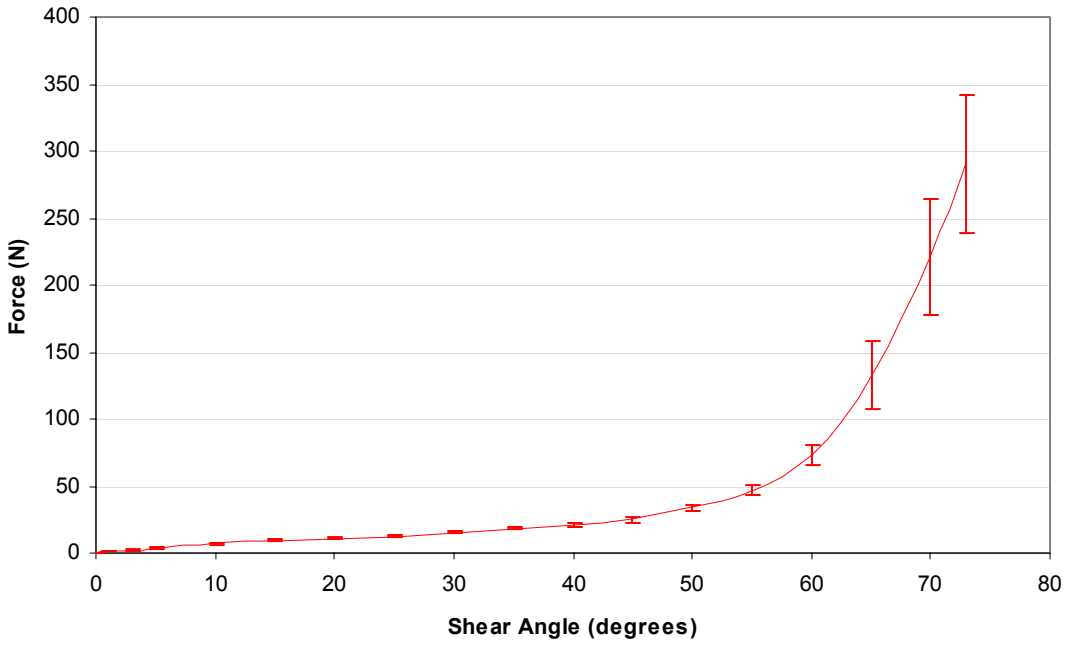

Figure 4.22 Analyzed Resin Impregnated Non-Crimp Carbon Fabric Picture Frame Results

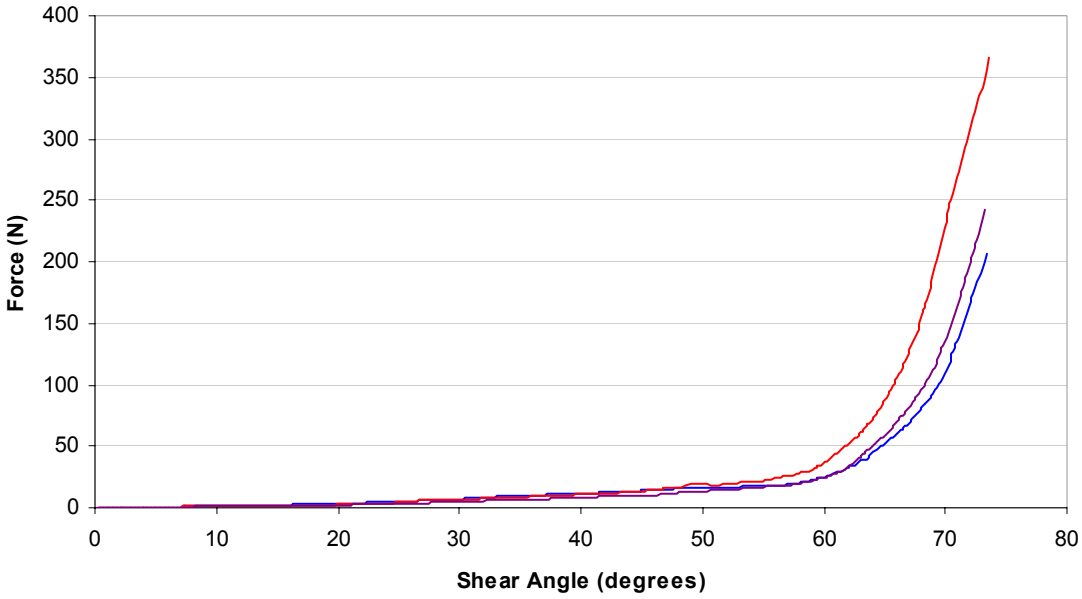

Figure 4.23 Resin Impregnated Plain Weave Carbon Fabric Picture Frame Results

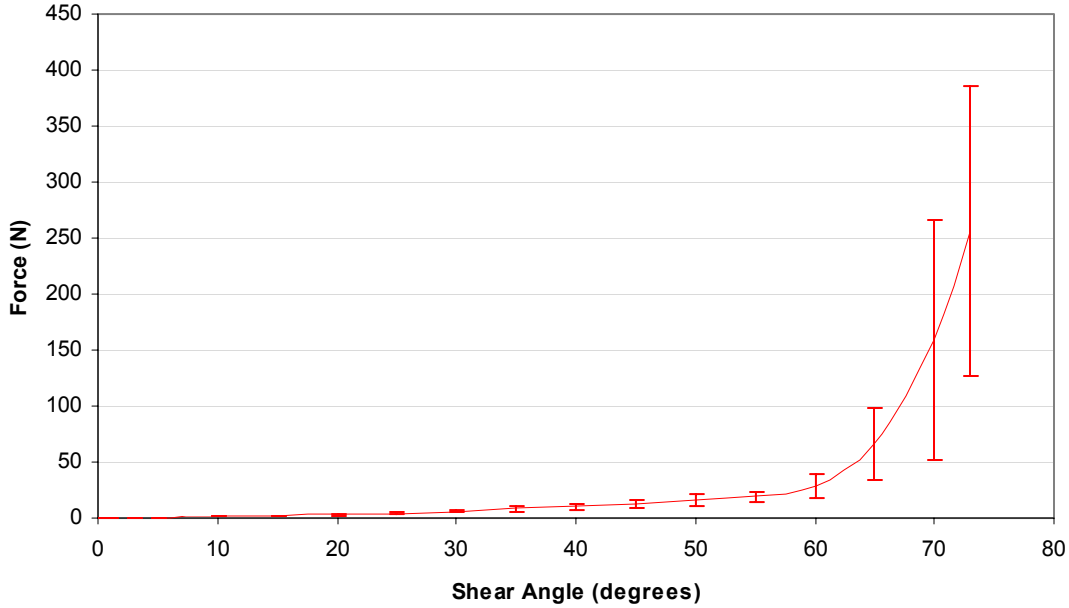

Figure 4.24 Analyzed Resin Impregnated Plain Weave Carbon Fabric Picture Frame Results

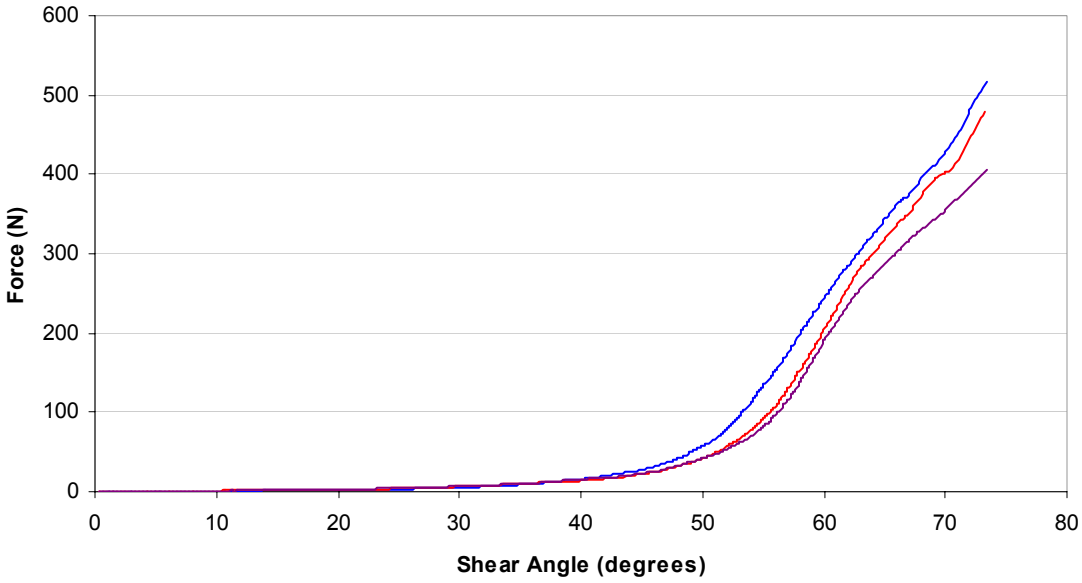

Figure 4.25 Resin Impregnated Non-Crimp Glass Fabric Picture Frame Results

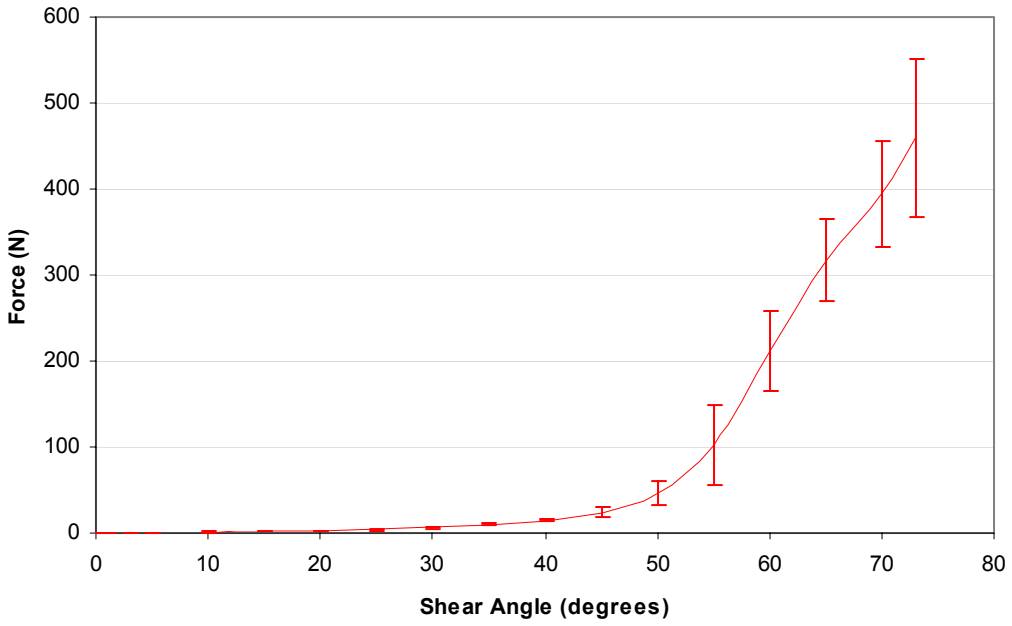

Figure 4.26 Resin Impregnated Non-Crimp Glass Fabric Picture Frame Results

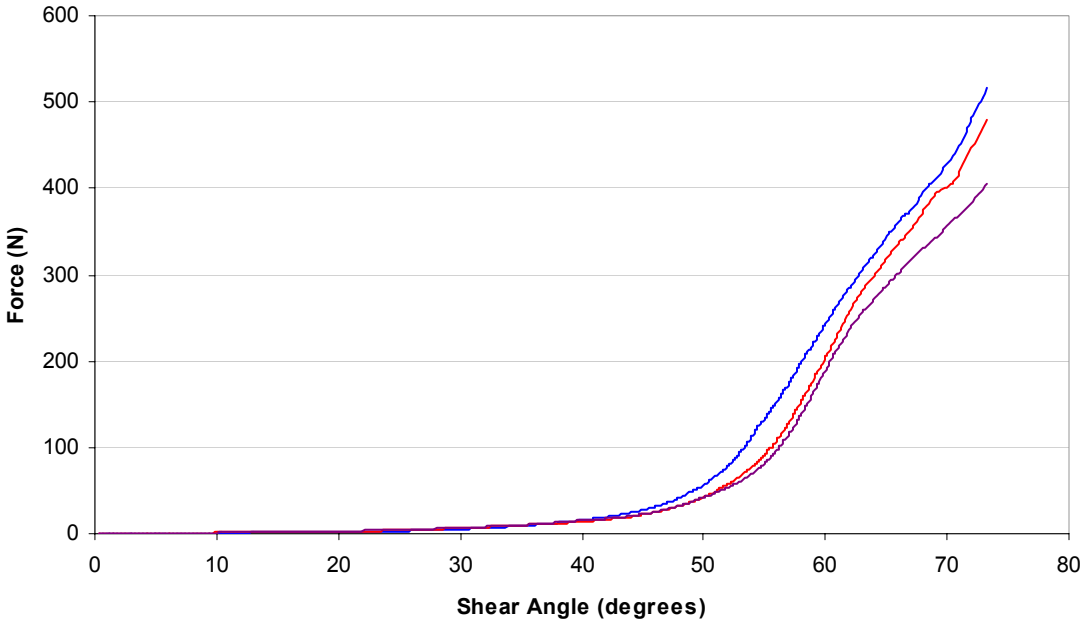

Figure 4.27 Resin Impregnated Plain Weave Glass Fabric Picture Frame Results

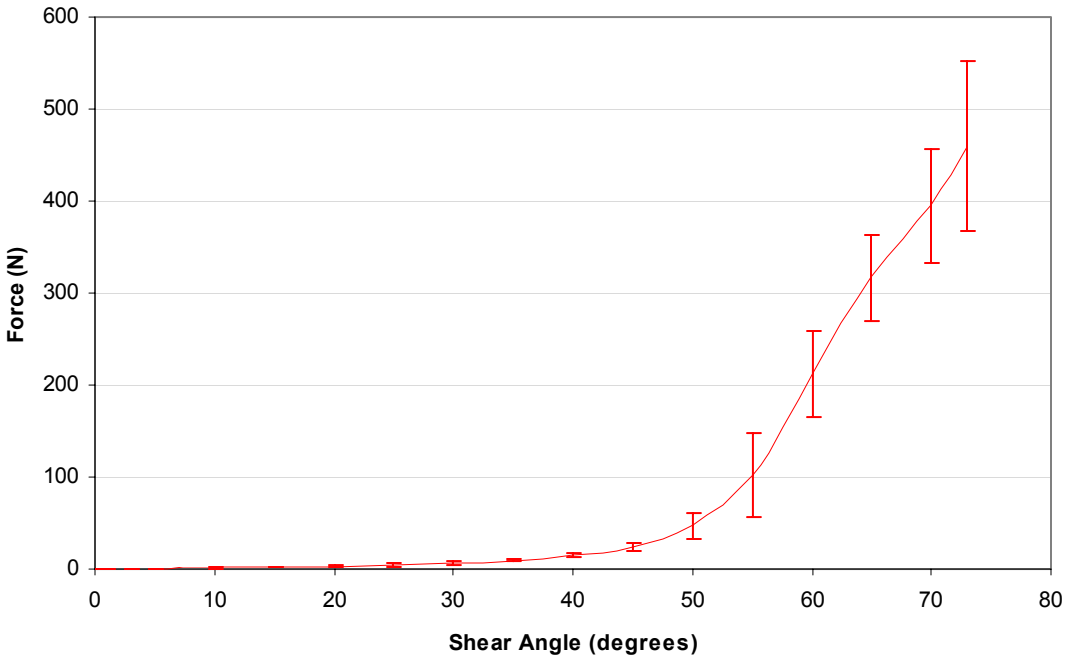

Figure 4.28 Resin Impregnated Plain Weave Glass Fabric Picture Frame Results

4.3.6 Results of Tensile Coupon Testing

Figures 4.29-4.32 illustrate the results for the tensile coupon testing for the four fabrics. Each fabric was tested in both 0 and 90 degrees. It is believed the non-crimp fabrics may show varying results due to fiber stitching for the different directions tested. The non-crimp fabrics were tested with the fiber perpendicular and parallel to the stitching. The results of the tensile tests are used to input the Young's Modulus into the RIDFT simulation model. These results are summarized in Table 4.5.

Table 4.5 Tensile Results of Resin-Wetted Fabrics

Fiber Property	Carbon non-crimp	Carbon plain weave	Glass non-crimp	Glass plain weave
Young's Modulus-LD (psi)	391600	232100	427900	123300
Young's Modulus-TD (psi)	217600	232100	427900	123300

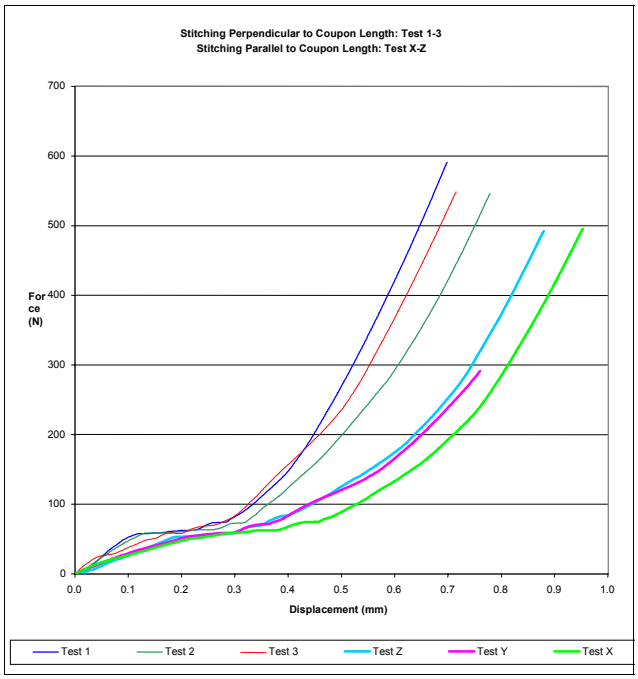

Figure 4.29 Non-Crimp Carbon Fabric Tensile Coupon Results

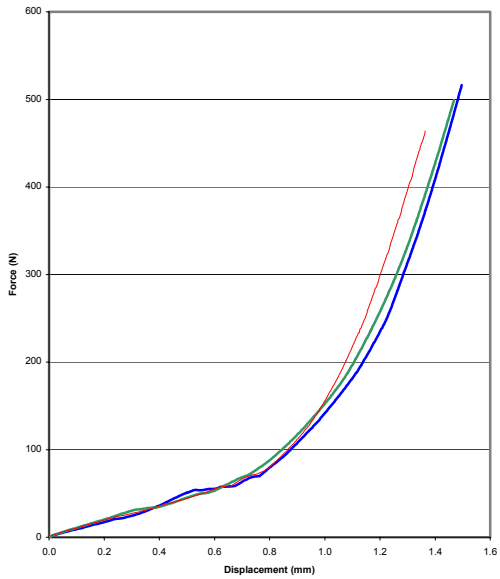

Figure 4.30 Plain Weave Carbon Fabric Tensile Coupon Results

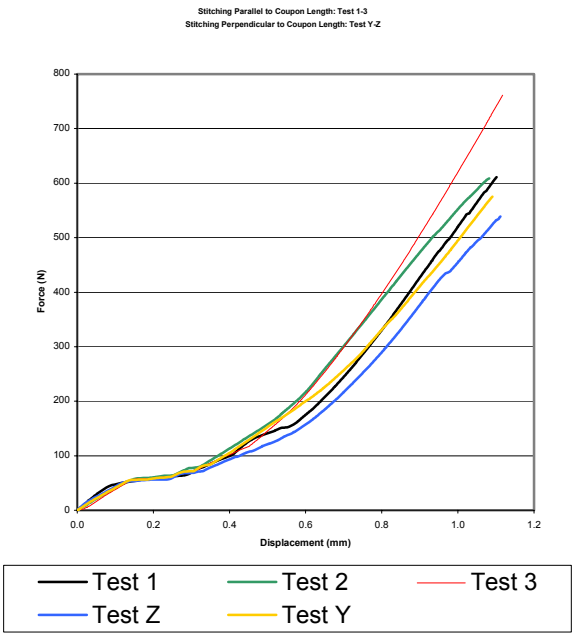

Figure 4.31 Non-Crimp Glass Fabric Tensile Coupon Results

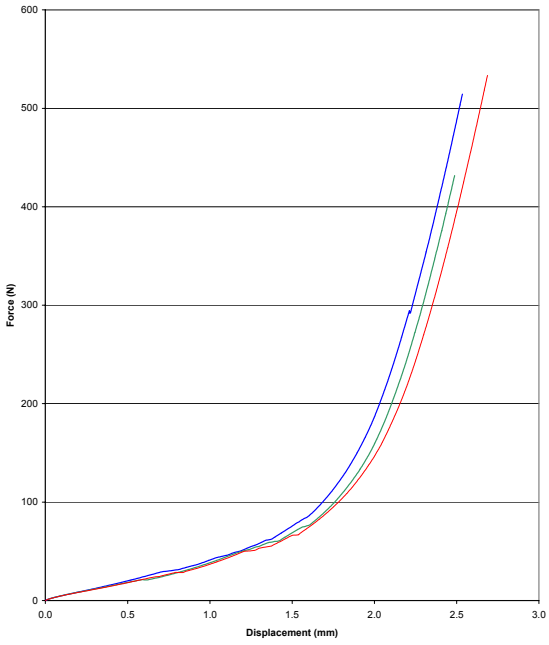

Figure 4.32 Plain Weave Glass Fabric Tensile Coupon Results

CHAPTER 5

DOE ANALYSIS AND SIMULATION OF RIDFT FORMABILITY

5.1 Design of Experiments (DOE) Investigation

Factorial Designs are widely used in experiments involving several factors where it is necessary to study the joint effect of the factors on a response [23]. The objective of this experimentation was to determine how changes within the manufacturing process affected formability and wrinkling of the finished part. These changes include varying part geometry, fiber layers, fiber type and fabric textile structures. Fiber type includes carbon fiber and E-glass fiber while fabric textile structures includes bi-directional woven and bi-directional knitted both (0° & 90°). Part geometries include a half-sphere and rectangular block. These process characteristics will be tested using the RIDFT prototype machine.

It is important to understand how different aspects of the experimentation may affect the outcome of the response variables and this is explained through a cause and effect diagram. Figure 5.1 illustrates the cause and effect diagram for the proposed experiment. We can see from this figure the possible unwanted causes that can affect the response variables of the experimental design.

For the factorial design nomenclature, 2^{4-1}, '4' represents the number of factors for the experiment. The '2' represents the number of levels for the experimentation, high and low. The '1' represents this to be a half-fraction and signified that only $2^{4-1}=8$ of the possible $2^4=16$ experiments are run.

To better understand the runs or design points associated with an experimental design, it can be illustrated geometrically as a cube. Suppose that three factors, A, B, and C, each at 2 levels, are of interest. The design is called a 2^3 factorial design and the eight treatment combinations can now be displayed geometrically as a cube.

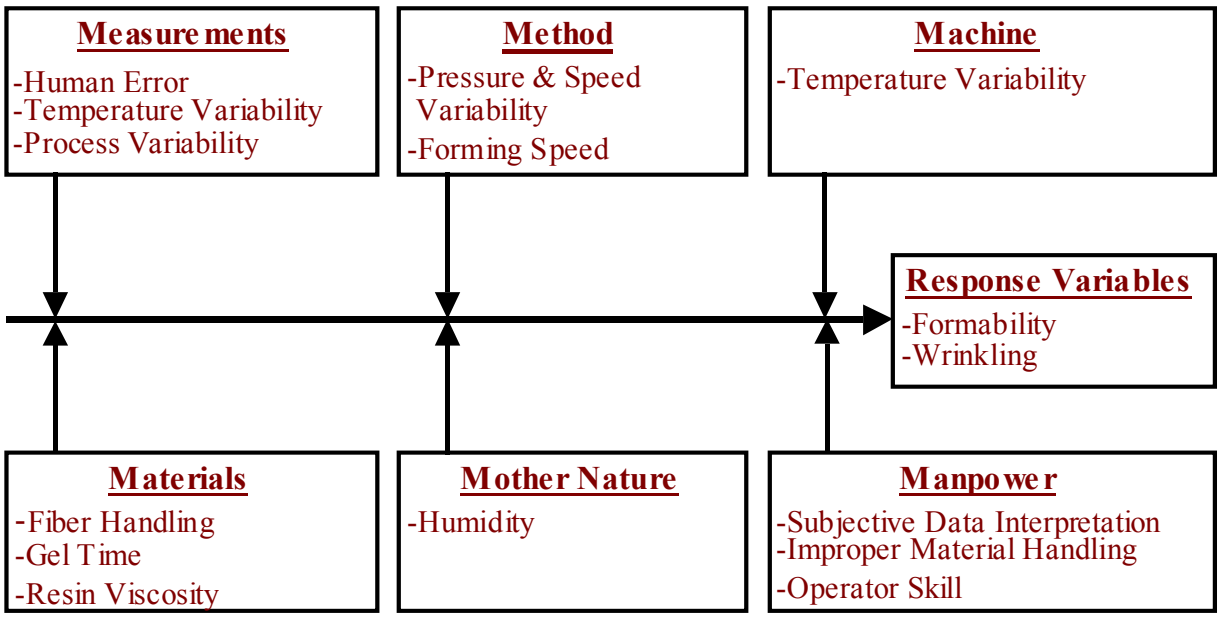

Figure 5.1 Cause and Effect Diagram

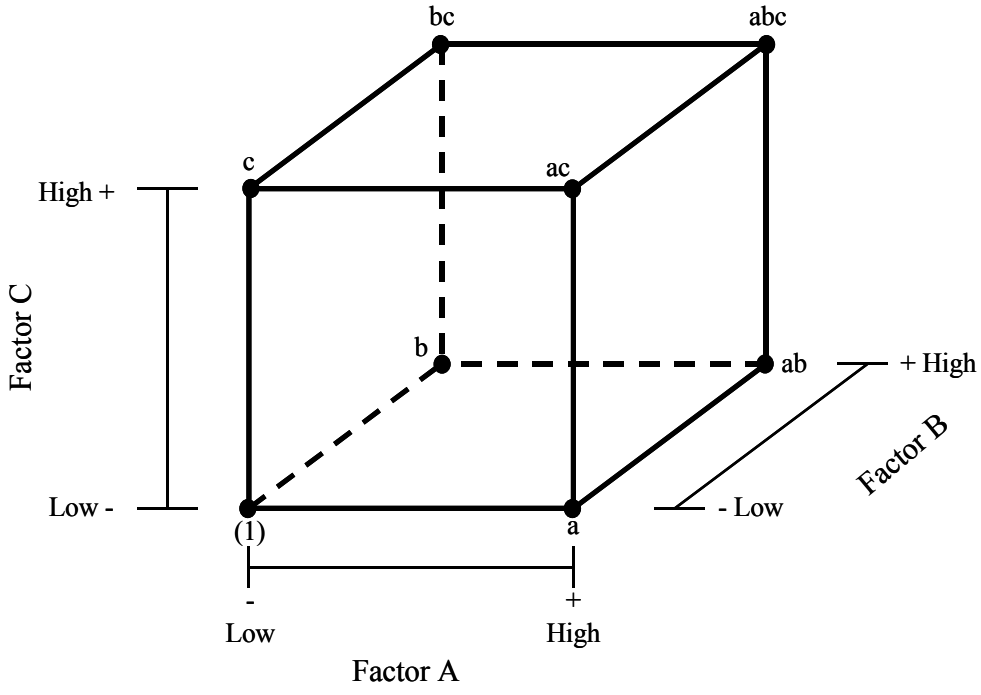

Figure 5.2 Geometric View

Figure 5.2 illustrates the geometric view for a 2^3 factorial design and the eight treatment combinations: a, b, c, ab, ac, abc, bc and 1 [23]. Consider estimating the main effects. First, consider estimating the main effect *A*. The effect of *A* when *B* and *C* are at the low level is [a - (1)]/n, where *n* represents the number of replicates. Similarly, the effect of *A* when *B* is at the high level and *C* is at the low level is [ab – b]/n. The effect of *A* when *C* is at the high level and *B* is at the low level is [ac – c]/n. Finally, the effect of *A* when both *B* and *C* are at the high level is [abc – bc]/n. Thus, the average effect of A is just the average of these four as shown in Equation 5.1 [18].

$$A = (1 / 4n)[a - (1) + ab – b + ac – c + abc - bc] \quad \text{Equation (5.1)}$$

Using the "+ and –" notation to represent the low and high levels of the factors, Table 5.1 illustrates the design matrix for the 2^3 design [23].

Table 5.1 Design Matrix

	Factor		
Run	A	B	C
1	-	-	-
2	+	-	-
3	-	+	-
4	+	+	-
5	-	-	+
6	+	-	+
7	-	+	+
8	+	+	+

To validate the reliability and repeatability of the process, two replicates will be used. For a 2^{4-1} experiment, this brings the total number of experiments to 16. The 2^{4-1} factorial design gives the experiment a resolution of IV. The resolution of the experimentation details the amount of confounding associated with effects of interest with resolution I having the least

resolution and resolution VII providing the best. Resolution IV is a design in which no main effect is aliased with any other main effect or with any two-factor interaction, but two-factor interactions are aliased with each other [23]. Resolution V is a design in which no main effect or two-factor interaction is aliased with any other main effect or two-factor interaction, but two-factor interactions are aliased with three factor-interactions [23]. Resolution IV designs are particularly useful for screening important factors. Often, these designs result in accurate and complete system understanding.

The designed experiments for this research will focus on two separate part geometries to investigate the ability of the RIDFT process to form the parts without wrinkling. These part geometries include half-spheres of different radii and blocks with varying corner radii.

5.2 Half-Sphere on Cylinder

One purpose for this shape investigation is to determine how varying the radius of the sphere affects the ability of the part to form without wrinkling. For this design of experiment (DOE), a 2^{4-1} experiment of resolution IV is used. The other purpose is to investigate how changing fiber layers, fiber type and fabric textile structure may affect the wrinkling of the part. Figure 5.3 illustrates the shape for the half-sphere on a cylinder with varying radii.

For this experimentation, all material below the half-sphere is not of concern for this DOE investigation. The response variable for this DOE investigation is wrinkling and categorized either not wrinkling, 0, or three degrees of wrinkling, 1-3 depending on the type or amount of wrinkling that occurred. Figure 5.4 illustrates a type 0 part with no wrinkles. Wrinkle type 1 was characterized as small wrinkling only occurring on the external of the part. Figure 5.5 illustrates the wrinkling that occurs on the outside of the part. Wrinkle type 2 was characterized as wrinkling occurring on the exterior and interior of the part. Figure 5.6 illustrates the wrinkling that occurs on the inside of the part. Wrinkle type 3 was characterized by the inability of the part to conform to the mold surface and with serious wrinkling of type 2. Figure 5.7 illustrates wrinkle type 3. The fabrics used are the same as described within Chapter 4, Materials Characterization.

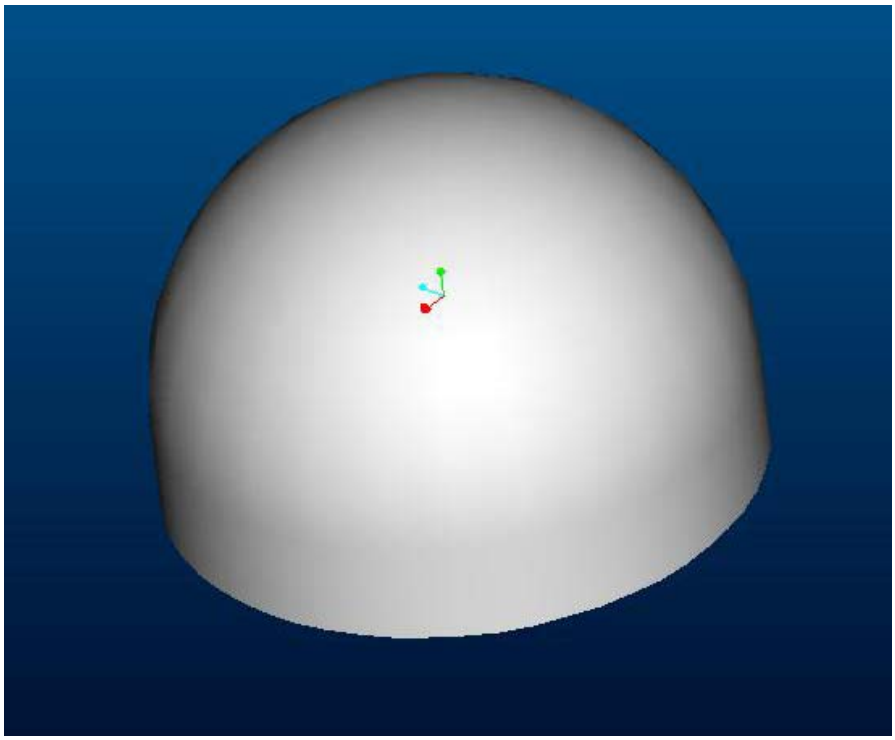

Figure 5.3 Half-Sphere on Cylinder

Figure 5.4 Type 0 No Wrinkle

Figure 5.5 Type 1 Wrinkle

Figure 5.6 Type 2 Wrinkle Inside

Figure 5.7 Type 3 Wrinkle

The response and input variables for this DOE are as follows.

- Input Variables
  - Radius 2 [2 inch, 2.5 inch]
  - Number of Layers 2 [6, 12]
  - Fiber Type 2 [CF, GF]
  - Fabric textile structure 2 [Woven, Knitted]
- Response Variables
  - Wrinkling 4 [No (0), Yes (1-3)]

During the experimental process, parameters were changed between experiments in accordance to the randomized factorial design table created with the use of Design Expert 6. This factorial design and the experimental results are shown in Table5. 2. The randomized test sequence was necessary to prevent the effects of unknown nuisance variables from contaminating the results [23]. Table 5.2 shows seven additional experiments conducted after the initial DOE investigation was complete. These experiments were necessary to gain further resolution of the output results. Resolution IV uses only eight of a possible combination of sixteen experiments. By adding seven additional experiments not previously run, uncertainties within the results are reduced and a total of fifteen out of sixteen combinations of experiments are run and analyzed. Appendix A illustrates all experimental results.

Table 5.2 Data Collection Table – Half-Sphere

	Std	Run	Block	Factor 1 A:Radius Inches	Factor 2 B:# of Layers	Factor 3 C:Fiber Type	Factor 4 D:Fiber Texite Structure	Response 1 Wrinkling NO(0) / Yes(1-3)
	15	1	Block 1	2.50	12.00	CF	Knitted	3
	4	2	Block 1	2.50	6.00	GF	Knitted	0
	1	3	Block 1	2.00	6.00	GF	Woven	1
	13	4	Block 1	2.00	12.00	CF	Woven	1
	5	5	Block 1	2.00	12.00	GF	Knitted	2
	10	6	Block 1	2.00	6.00	CF	Knitted	2
	11	7	Block 1	2.50	6.00	CF	Woven	0
	6	8	Block 1	2.00	12.00	GF	Knitted	2
	12	9	Block 1	2.50	6.00	CF	Woven	0
	14	10	Block 1	2.00	12.00	CF	Woven	1
	9	11	Block 1	2.00	6.00	CF	Knitted	2
	16	12	Block 1	2.50	12.00	CF	Knitted	3
	3	13	Block 1	2.50	6.00	GF	Knitted	0
	2	14	Block 1	2.00	6.00	GF	Woven	1
	8	15	Block 1	2.50	12.00	GF	Woven	1
	7	16	Block 1	2.50	12.00	GF	Woven	1
	20	17	Block 2	2.50	6.00	GF	Woven	0
	17	18	Block 2	2.50	12.00	CF	Woven	0
	22	19	Block 2	2.50	12.00	GF	Knitted	1
	21	20	Block 2	2.00	12.00	GF	Woven	1
	19	21	Block 2	2.00	6.00	CF	Woven	0
	23	22	Block 2	2.00	6.00	GF	Knitted	0
	18	23	Block 2	2.00	12.00	CF	Knitted	3

5.2.1 Data Analysis – Half-Sphere on Cylinder

Several assumptions were made regarding the outcome of this DOE investigation for the initiation of the experimental design. For example, number of fiber layers and radius of the sphere were assumed to have a direct impact on the wrinkling of the manufactured parts with an increase in fiber layers and a decrease in radius corresponding to an increase in the likelihood of wrinkles forming. Factors such as fiber type and fabric textile structure were unknown as to their effects on wrinkling within the experimental investigation. The half normal plot analysis is used to determine what factors are significant for a particular response variable. This plot showed that the absolute value of the term effects (horizontal axis) against a half normal probability scale (vertical axis). Insignificant terms fall on a straight line. Terms that departed

from the line are initially modeled and tested for significance [11]. Figure 5.8 illustrates the half normal plot for wrinkling.

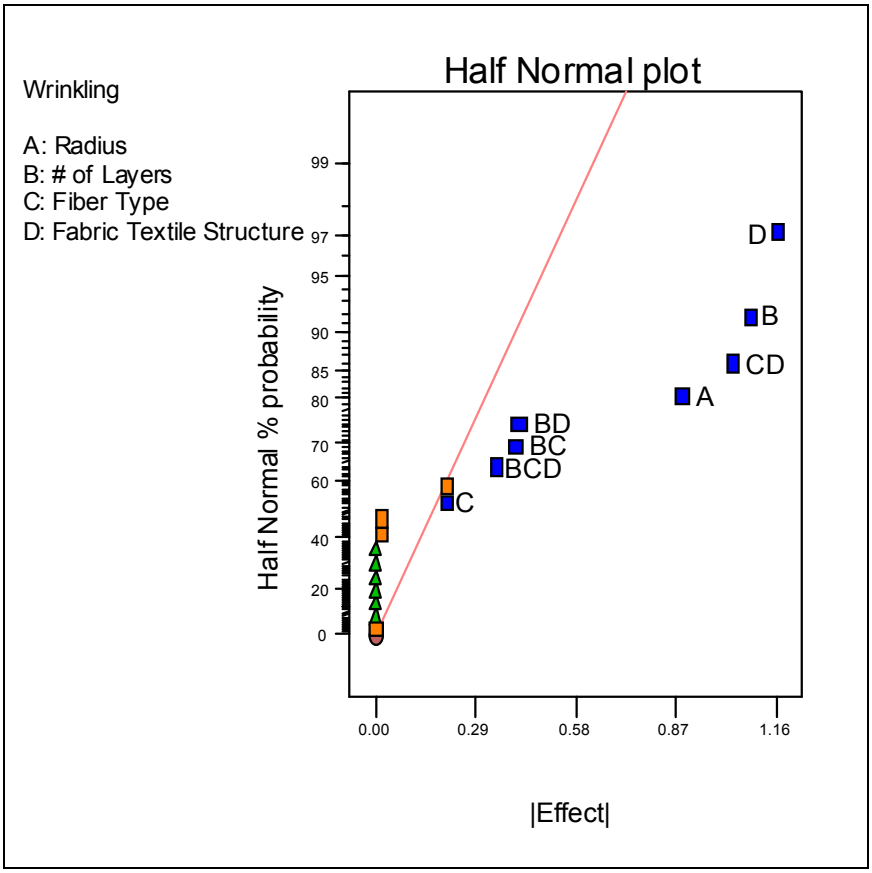

Figure 5.8 Half Normal Plot for Wrinkling

In analyzing the half normal plot for wrinkling, as shown in Figure 5.8, several factors including main effects and their interactions where shown to potentially affect the wrinkling of the part. These interactions were CD (fiber type and fiber textile structure), BD (number of layers and fabric textile structure), BC (number of layers and fiber type) and BCD (number of layers, fiber type and fiber textile structure). Factors A, B, C and D, radius, number of layers fiber type and fabric textile structure respectively, were all shown to potentially affect wrinkling.

This research analyzed the interactions and main effect to show possible aliases. Aliases identify the relationship of a main effect or interaction with other main effects or interactions that carry the same significance. Aliased terms used the same experimental runs, high and low, to calculate the effect estimates. It is unknown which of the aliased terms contributed to the change in the responses [24]. Figure 5.9 shows the alias table for the interactions and main effects shown in the half normal plot of Figure 5.8. An 'M' next to the term represents that to be a main effect as defined in the half normal plot.

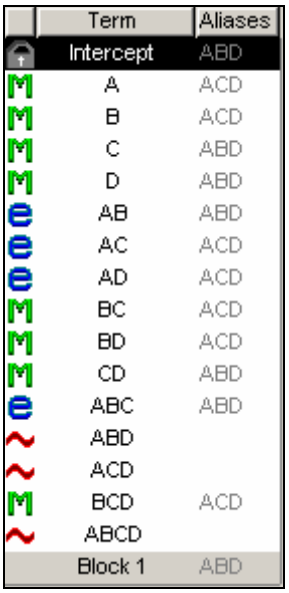

	Term	Aliases
	Intercept	ABD
M	A	ACD
M	B	ACD
M	C	ABD
M	D	ABD
e	AB	ABD
e	AC	ACD
e	AD	ACD
M	BC	ACD
M	BD	ACD
M	CD	ABD
e	ABC	ABD
~	ABD	
~	ACD	
M	BCD	ACD
~	ABCD	
	Block 1	ABD

Figure 5.9 Aliases for Main Effects and Two-Factor Interactions

The next step for the analysis was to evaluate the initial model using ANOVA table for wrinkling, shown in Table 5.3. From this table, a low p-value is shown for the overall model signifying the model to be significant. The p-value used the data to test the hypothesis showing the significance of the factors. A p-value less than 0.05 is generally said to be significant. The table also shows the main effects A (radius), B (number of layers), C (fiber type), D (fabric textile structure), BCD (number of layers, fiber type and fabric textile structure) and CD (fiber type and fabric textile structure) all to be significant with a p-value < 0.05.

Table 5.3 ANOVA

Use your mouse to right click on individual cells for definitions.

Response: Wrinkling

ANOVA for Selected Factorial Model

Analysis of variance table [Partial sum of squares]

Source	Sum of Squares	DF	Mean Square	F Value	Prob > F	
Block	1.61	1	1.61			
Model	23.75	8	2.97	66.79	< 0.0001	significant
A	*1.70*	*1*	*1.70*	*38.26*	*0.0001*	
B	*5.12*	*1*	*5.12*	*115.18*	*< 0.0001*	
C	*0.82*	*1*	*0.82*	*18.43*	*0.0016*	
D	*8.93*	*1*	*8.93*	*200.97*	*< 0.0001*	
BC	*1.32*	*1*	*1.32*	*29.73*	*0.0003*	
BD	*0.82*	*1*	*0.82*	*18.43*	*0.0016*	
CD	*5.12*	*1*	*5.12*	*115.18*	*< 0.0001*	
BCD	*0.39*	*1*	*0.39*	*8.80*	*0.0141*	
Residual	0.44	10	0.044			
Lack of Fit	*0.44*	*4*	*0.11*			
Pure Error	*0.000*	*6*	*0.000*			
Cor Total	25.80	19				

The Model F-value of 66.79 implies the model is significant. There is only a 0.01% chance that a "Model F-Value" this large could occur due to noise.

The next step is to evaluate the effect graphs to better understand how changes with a main effect or interaction affect the wrinkling of the part. Figure 5.10 illustrates the main effect A (radius) and how varying the radius of the sphere from 2.5 inches to 2 inches affects the ability of the part to be formed without wrinkles. As the radius of the hemi-sphere is increased, it is seen the likelihood of a wrinkle decreases. Figure 5.11 illustrates how increasing the fiber layers from 6 to 12 increases the likelihood of wrinkling to occur. It is also illustrated that for woven fabrics, glass fiber has a higher tendency of wrinkling. For knitted fabrics, carbon fiber has a higher tendency of wrinkling.

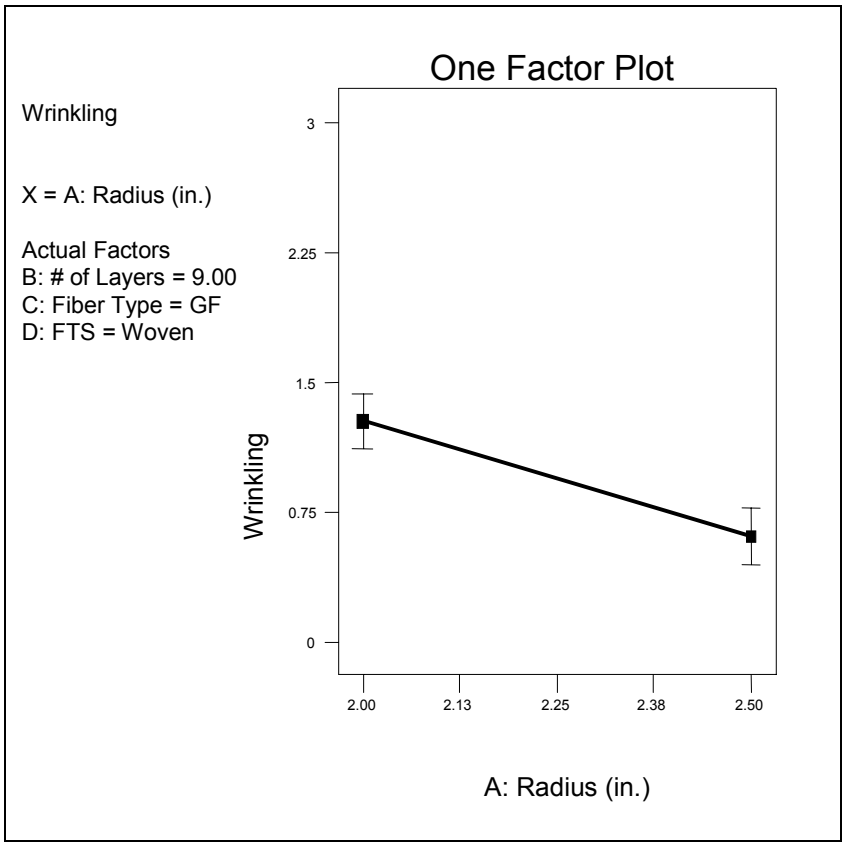

Figure 5.10 Effect Graph of A (Radius)

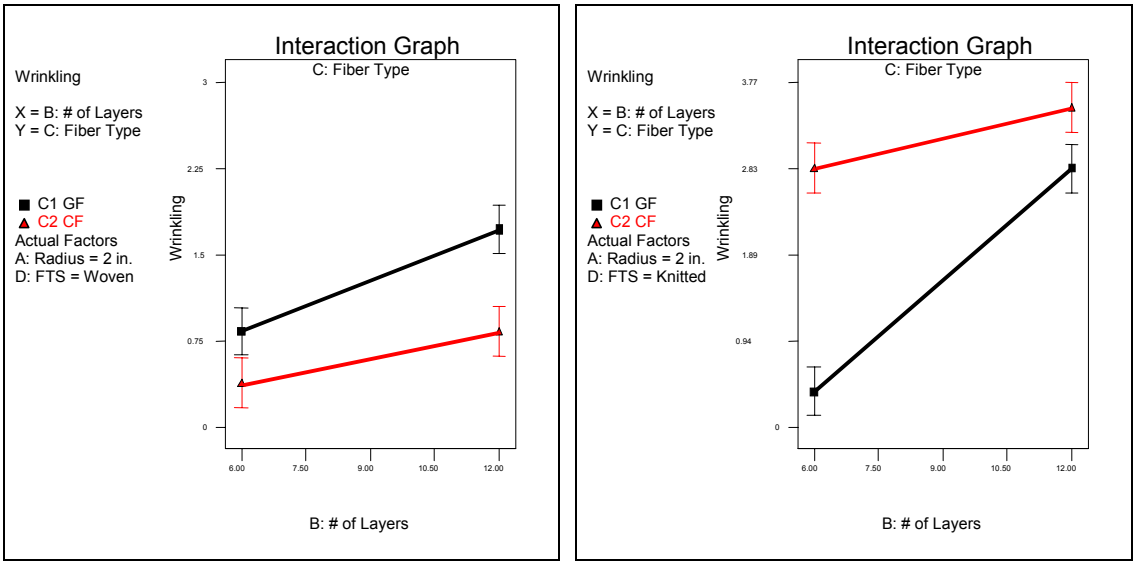

Figure 5.11 Effect Graph of BC (Number of Layers & Fiber Type) Interaction

Figure 5.12 illustrates the CD (fiber type & fabric textile structure) interaction. It is shown the general trend for knitted fiber is an increase in the tendency to wrinkle when going from glass fiber to carbon fiber. It is also shown the general trend for woven fiber is a decrease in the tendency to wrinkle when going from glass fiber to carbon fiber. Figure 5.13 illustrates the 3D surface effect graph of wrinkling as a function of fiber type, fiber textile structure (FTS), number of layers and radius. Wrinkling values may be shown to exceed 3, but the results signify a statistical confidence interval.

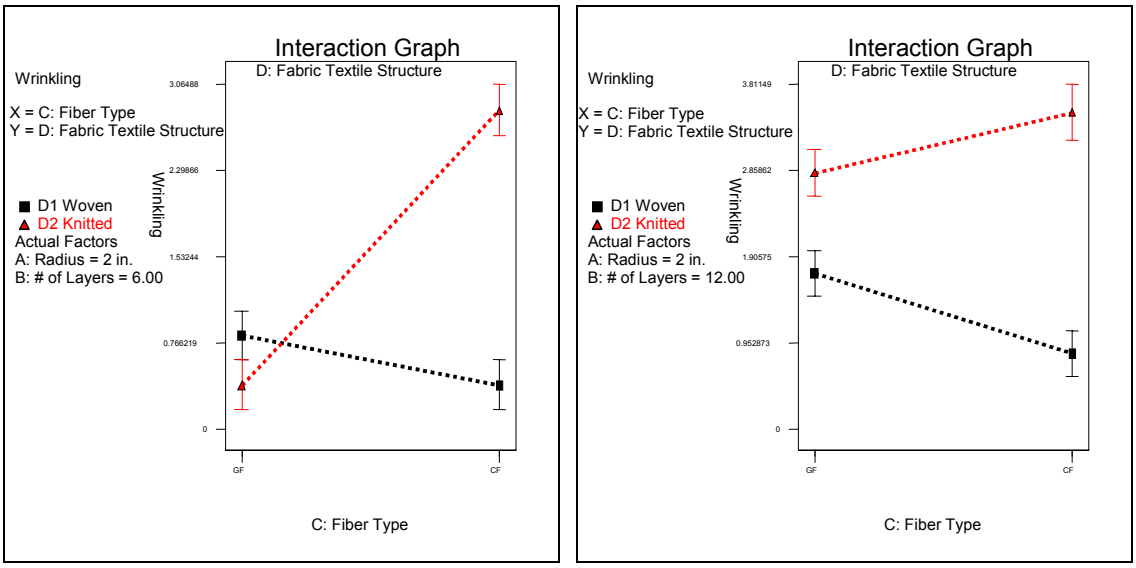

Figure 5.12 Effect Graph of CD (Fabric Type & Fabric Textile Structure) Interaction

5.2.2 Experimental Validation of Prediction Model

The data collected and entered is also used to create a prediction model based on linear regression of all factors and responses. This linear regression equation is used to predict the outcome of future experiments based on the outcome of known experiments. Equation 5.2 shows the regression equation where A, B, C and D are radius, # of layers, fiber type and fabric textile structure, respectively.

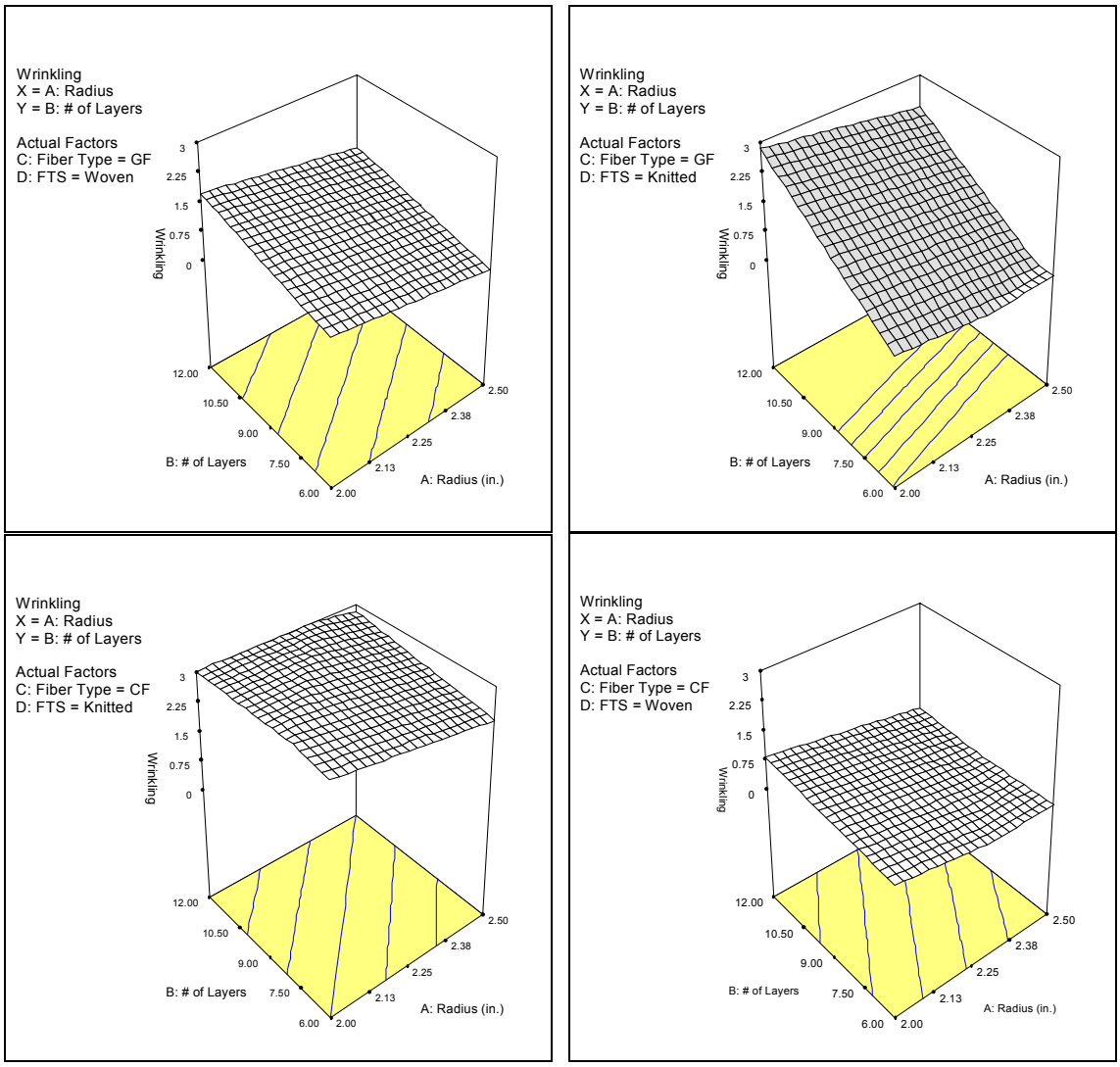

Figure 5.13 3D Response Surface of Wrinkling for the 4 Fabric Types

Wrinkling = +1.38-0.34*A+0.56*B+0.25*C+0.75*D–0.13*A*B-0.28*B*C+0.23*B*D+0.62 *C*D-0.17*B*C*D Equation (5.2)

Using Equation 5.2 the model is now validated for it accuracy. For model validation three additional experiments are run and their outcomes are predicted before the parts are produced. The parts produced along with the predicted and actual wrinkling types are listed below in Table 5.4.

Table 5.4 Experimental Validation of Prediction Model

VALIDATION RUN #1

Factor	Name	Level	Low Level	High Level	Std. Dev.
A	Radius	*2 inches*	2 inches	2.5 inches	0
B	# of Layers	*9*	6	12	0
C	Fiber Type	*CF*	GF	CF	N/A
D	Fiber Layout	*Woven*	Woven	Knitted	N/A

	Prediction	Actual	SE Mean	95% CI low	95% CI high	SE Pred	95% PI low	95% PI high
Wrinkling	*0.585*	*1*	0.075	0.417	0.754	0.172	0.196	0.975

VALIDATION RUN #2

Factor	Name	Level	Low Level	High Level	Std. Dev.
A	Radius	*2 inches*	2 inches	2.5 inches	0
B	# of Layers	*9*	6	12	0
C	Fiber Type	*GF*	GF	CF	N/A
D	Fiber Layout	*Knitted*	Woven	Knitted	N/A

	Prediction	Actual	SE Mean	95% CI low	95% CI high	SE Pred	95% PI low	95% PI high
Wrinkling	*1.601*	*2*	0.083	1.412	1.790	0.176	1.202	2.000

VALIDATION RUN #3

Factor	Name	Level	Low Level	High Level	Std. Dev.
A	Radius	*2.5 inches*	2 inches	2.5 inches	0
B	# of Layers	*9*	6	12	0
C	Fiber Type	*GF*	GF	CF	N/A
D	Fiber Layout	*Knitted*	Woven	Knitted	N/A

	Prediction	Actual	SE Mean	95% CI low	95% CI high	SE Pred	95% PI low	95% PI high
Wrinkling	*0.926*	*1*	0.077	0.751	1.101	0.174	0.534	1.319

From Table 5.4, validation run #1 has a 95 percent prediction interval between 0.196 and 0.975 with an actual experimentation result of 1. Validation run #2 has a 95 percent prediction interval between 1.202 and 2.0 with an actual experimentation result of 2. For validation run #3 the 95 percent prediction interval is between .534 and 1.319 with an actual experimentation result of 1. The results are in good agreement with the 95 percent prediction intervals.

5.2.3 Half-Sphere on Cylinder Summary

The DOE results show the main effect A (radius) and how varying the radius of the sphere from 2.5 inches to 2 inches affects the ability of the part to be formed without wrinkles. This result is understood as the requirements of the fiber to form tight radii are reduced. As the radius of the hemi-sphere is increased, it is seen the likelihood of a wrinkle decreases. Increasing the fiber layers from 6 to 12 increases the likelihood of wrinkling to occur. This can be explained by the increase in interactions that occur between fiber layers. The addition of 6 layers creates an additional 6 contact interfaces where friction forces further resist inter-ply slip.

It is also shown for woven fabrics, glass fabric has a higher tendency of wrinkling over carbon fabric. There are two possible explanations for this finding. The inter-ply friction for carbon-carbon interfaces is much lower than that of glass-glass interfaces. Next, from the picture frame test results, the force required to sustain shear for the woven glass fabric is 24.66 psi while for woven carbon fabric it is 15.95 psi. This clearly shows the woven glass fabric is much easier to sustain shear.

For knitted fabrics, carbon fiber has a higher tendency of wrinkling over glass fiber. It is believed these results are based on fiber architecture. Although it is known the inter-ply forces for carbon-carbon interfaces is lower than that of glass-glass interfaces, the ability to overcome fiber architecture limitations prevails. Although the picture frame results show the non-crimp carbon fabric reaches higher locking angles the force required to sustain shear for the non-crimp carbon fabric is higher; 11.02 psi as compared to 7.397 psi for non-crimp glass fabric. Although not fully understood at this time, it is believe the stitching type plays a roll in the ability of a fiber to form over various shapes.

For the CD (fiber type & fabric textile structure) interaction, it is shown the general trend for knitted fiber is an increase in the tendency to wrinkle when going from glass fiber to carbon fiber. It is also shown the general trend for woven fiber is a decrease in the tendency to wrinkle when going from glass fiber to carbon fiber. From initial friction tests it is shown for carbon fabrics the inter-ply friction coefficients are lower for the woven fabric as compared to the non-crimp carbon fabric.

5.3 Rectangular Block

One purpose for this shape investigation is to determine how varying the corner radii of the rectangular block affects the ability of the part to form without wrinkling. For this DOE, a 2^4 experiment is used. The other purpose is to investigate how changing fiber layers, fiber type and fabric textile structure may affect the wrinkling of the part. Figure 5.14 illustrates the shape for the rectangular block with varying radii.

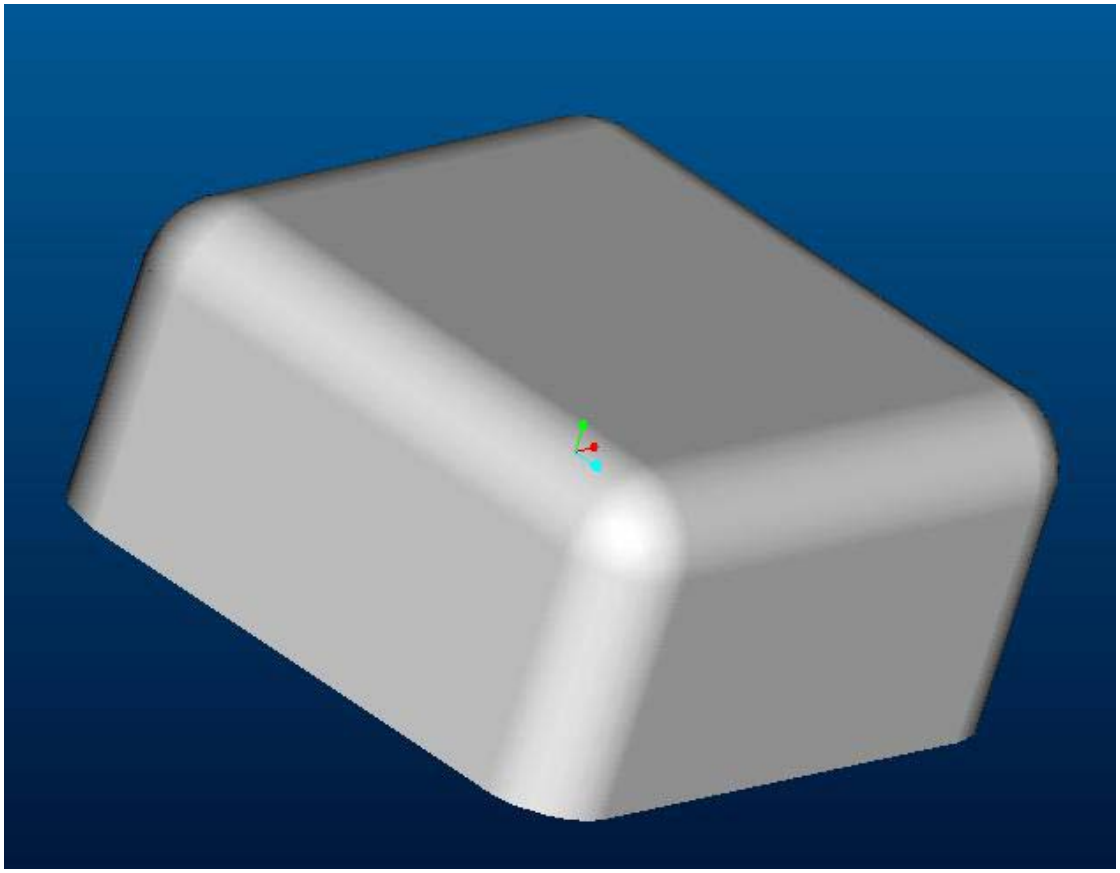

Figure 5.14 Block With Varying Radii

For this experimentation, all material below the half-sphere is not of concern for this DOE investigation. The response variable for this DOE investigation is wrinkling and categorized as either not wrinkling, 0, or three degrees of wrinkling, 1-3 depending on the type of wrinkling that occurred. Figure 5.15 illustrates a type 0 part with no wrinkles. Wrinkle type 1 was characterized as small wrinkling only occurring on the external of the part. Figure 5.16 illustrates the wrinkling that occurs on the outside of the part. Wrinkle type 2 was characterized as wrinkling occurring on the exterior and interior of the part. Figure 5.17 illustrates the wrinkling that occurs on the inside of the part. Wrinkle type 3 was characterized by the inability of the part to conform to the mold surface and with serious wrinkling of type 2. Figure 5.18 illustrates wrinkle type 3.

Figure 5.15 Type 0 No Wrinkle

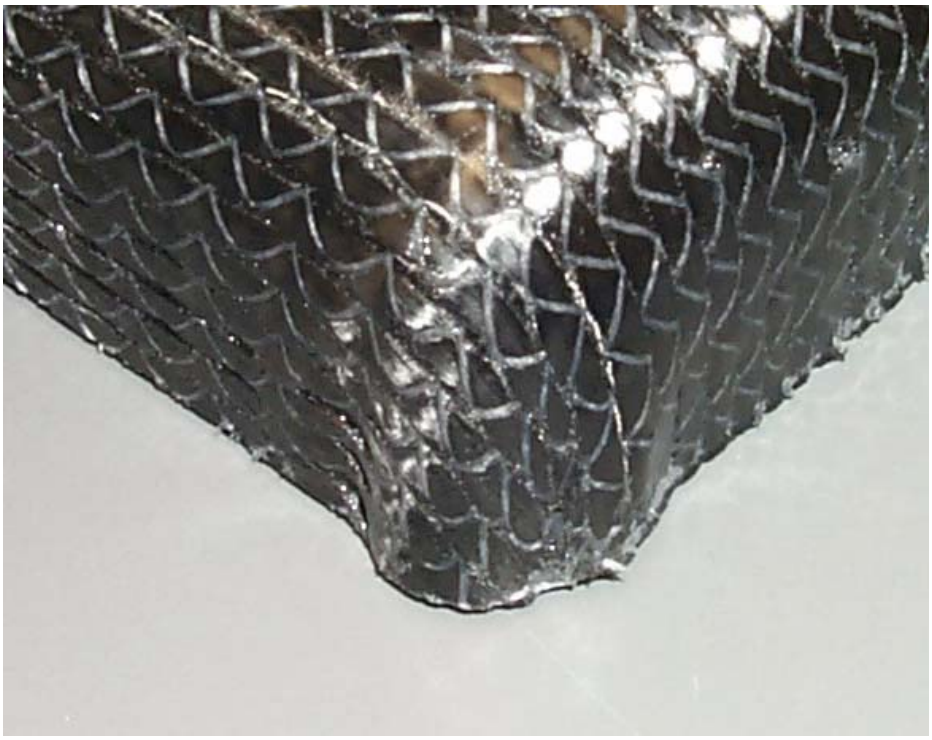

Figure 5.16 Type 1 Wrinkle

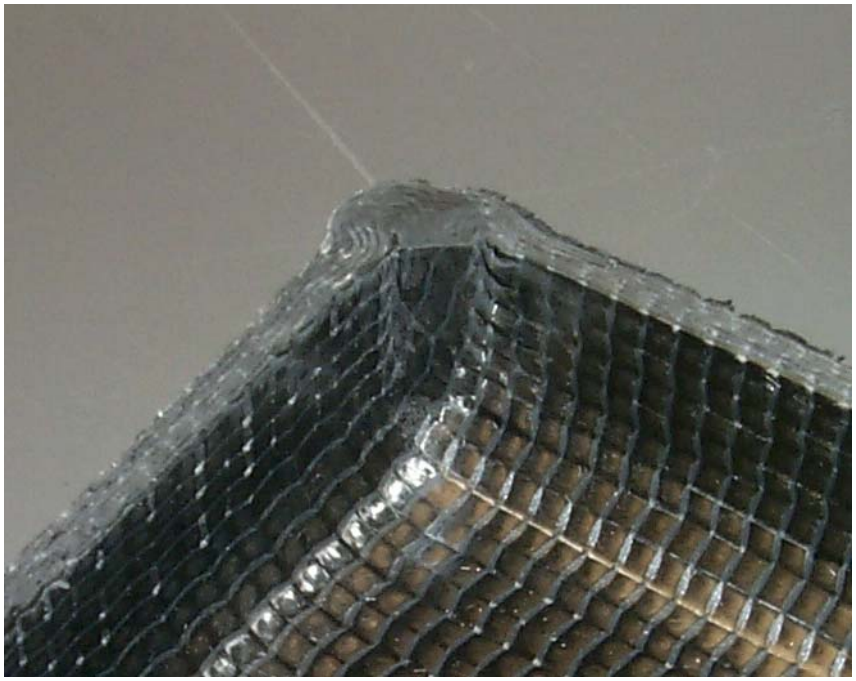

Figure 5.17 Type 2 Wrinkle Inside

Figure 5.18 Type 3 Wrinkle

A thickness ratio is calculated by dividing the average corner thickness by the average side wall thickness and is used as an objective response in the DOE investigation. The sidewall to corner ratio is determined by measuring the thickness of the four sides and creating an average side thickness. The thickness of the four corners are measured and an average corner thickness is calculated. Figure 5.19 illustrates the measurements taken for the corner to sidewall ratio.

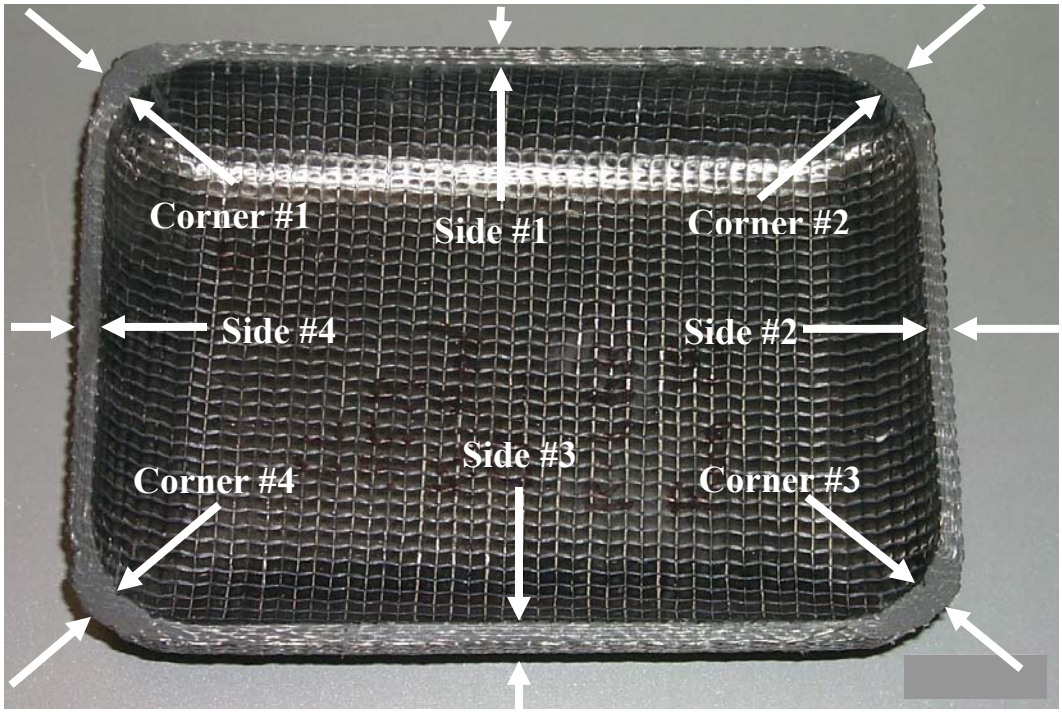

Figure 5.19 Corner to Sidewall Ratio

The response and input variables for this DOE are as follows:

- Input Variables
  - Radius 2 [0.375 inches, 0.75 inches]
  - Number of Layers 2 [3, 6]
  - Fiber Type 2 [CF, GF]
  - Fabric textile structure 2 [Woven, Knitted]
- Response Variables

- Wrinkling 4 [No (0), Yes (1-3)]
- Thickness Ratio Ratio Number

During the experimental process, parameters were changed between experiments in accordance to the randomized factorial design table. This factorial design and the results are shown in Table 5.5. The randomized test sequence was necessary to prevent the effects of unknown nuisance variables from contaminating the results [23]. Table 5.5 shows 4 additional experiments after the initial DOE investigation was complete. These experiments were used to gain further resolution of the pure error for the output results. Appendix B illustrates all experimental run results.

Table 5.5 Data Collection Table – Rectangular Block

	Std	Run	Block	Factor 1 A:Radius Inches	Factor 2 B:# of Layers	Factor 3 C:Fiber Type	Factor 4 D:Fiber Layout	Response 1 Ratio C/S	Response 2 Subjective
	15	1	Block 1	0.38	6.00	CF	Knitted	1.76	3
	3	2	Block 1	0.38	6.00	GF	Woven	2.22	2
	8	3	Block 1	0.75	6.00	CF	Woven	1.9	1
	5	4	Block 1	0.38	3.00	CF	Woven	2.23	0
	9	5	Block 1	0.38	3.00	GF	Knitted	1.88	1
	12	6	Block 1	0.75	6.00	GF	Knitted	1.72	1
	2	7	Block 1	0.75	3.00	GF	Woven	1.78	1
	11	8	Block 1	0.38	6.00	GF	Knitted	1.66	1
	7	9	Block 1	0.38	6.00	CF	Woven	2.29	1
	4	10	Block 1	0.75	6.00	GF	Woven	2.09	2
	14	11	Block 1	0.75	3.00	CF	Knitted	1.94	2
	10	12	Block 1	0.75	3.00	GF	Knitted	1.8	1
	1	13	Block 1	0.38	3.00	GF	Woven	1.67	1
	13	14	Block 1	0.38	3.00	CF	Knitted	1.91	2
	20	15	Block 1	0.75	6.00	CF	Knitted	1.68	2
	6	16	Block 1	0.75	3.00	CF	Woven	1.97	0
	16	17	Block 2	0.75	3.00	CF	Woven	2.02	0
	17	18	Block 2	0.75	6.00	CF	Woven	1.9	1
	18	19	Block 2	0.75	3.00	CF	Knitted	1.67	1
	19	20	Block 2	0.75	6.00	CF	Knitted	1.59	2

5.3.1 Data Analysis – Corner/Sidewall Ratio

Several hypotheses were made regarding the outcome of this DOE investigation for the initiation of the experimental design. For example, number of fiber layers and corner radii of the rectangular block were assumed to have a direct impact on the corner/sidewall ratio of the manufactured part with an increase in fiber layers and a decrease in radii corresponding to an increase in this ratio. Factors such as fiber type and fabric textile structure were unknown as to their effects on corner/sidewall ratio within this experimental investigation.

The half normal plot analysis, as used for the half-sphere DOE investigation, is used to determine which factors are potentially significant for a particular response variable. In analyzing the half normal plot for corner/sidewall ratio, as shown in Figure 5.20, one two-factor interaction, BD (number of layers and fabric textile structure), and one main effect, D (fabric textile structure), where shown to potentially affect the corner/sidewall ratio.

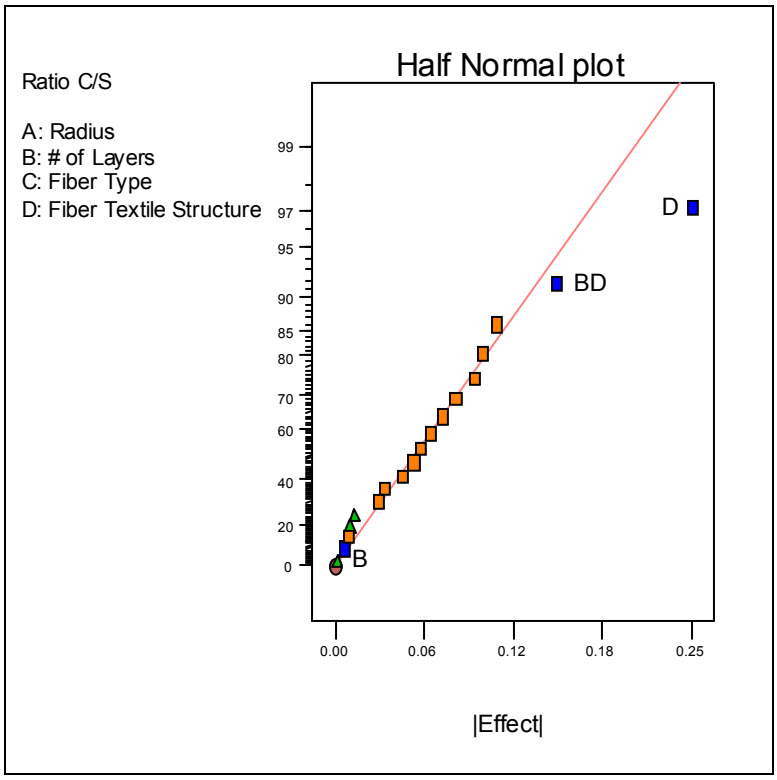

Figure 5.20 Half Normal Plot for Corner/Sidewall Ratio

The next step for the analysis was to evaluate the ANOVA for corner/sidewall ratio. The ANOVA table for the corner/sidewall ratio is shown in Table 5.6. From this table, a low p-value is shown for the model signifying the model to be significant. The P-value used the data to test the hypothesis showing the significance of the factors. A p-value less than 0.05 is generally said to be significant. The table also shows the factor D (fabric textile structures) and the interaction BD (number of layers and fabric textile structure) to be significant with a p-value < .05.

Table 5.6 ANOVA for Corner/Sidewall Ratio

Response: Ratio C/S

ANOVA for Selected Factorial Model

Analysis of variance table [Partial sum of squares]

Source	Sum of Squares	DF	Mean Square	F Value	Prob > F	
Block	0.040	1	0.040			
Model	0.42	3	0.14	6.11	0.0063	significant
B	*1.800E-004*	*1*	*1.800E-004*	*7.890E-003*	*0.9304*	
D	*0.30*	*1*	*0.30*	*13.26*	*0.0024*	
BD	*0.12*	*1*	*0.12*	*5.06*	*0.0399*	
Residual	0.34	15	0.023			
Cor Total	0.80	19				

The Model F-value of 6.11 implies the model is significant. There is only a 0.63% chance that a "Model F-Value" this large could occur due to noise.

The next step is to evaluate the effect graphs to better understand how changes with a particular factor or two-factor interaction affect the corner/sidewall ratio of the part. Figure 5.21 illustrates the BD (number of layers and fabric textile structure) interaction and how varying the number of fiber layers vs. the fiber type affects the corner/sidewall ratio. For the woven fiber, increasing the number of fiber layers from 3-6 increases the corner/sidewall ratio, while for the knitted fiber, increasing the number of fiber layers from 3-6 decreases the corner/sidewall ratio.

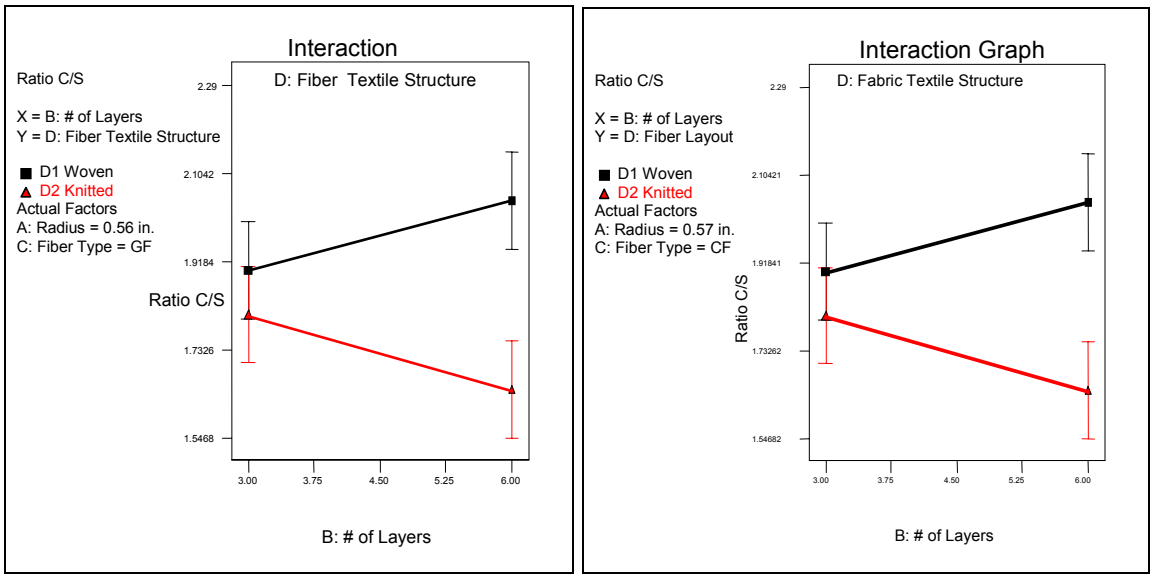

Figure 5.21 BD (Number of Layers and Fabric Textile Structure)

5.3.2 Corner/Sidewall Ratio Summary

The DOE results show the BD (number of layers and fabric textile structure) interaction to be significant. Varying the number of fiber layers vs. the fiber type affects the corner/sidewall ratio. For the woven fiber, increasing the number of fiber layers from 3-6 increases the corner/sidewall ratio, while for the knitted fiber, increasing the number of fiber layers from 3-6 decreases the corner/sidewall ratio. This phenomenon is not completely understood, but a plausible explanation can be given. A prediction equation is given for the corner/sidewall ratio in Equation 5.3.

Corner/Sidewall Ratio = 1.85–3.000E-3*B–0.12*D–0.076*B*D Equation (5.3)

The knitted fabrics are oriented such that the different fiber orientations exist on different fiber planes with one layer of unidirectional fiber stitched on top another layer of unidirectional fiber. However, the woven fiber co-exists in a single plane as they are bound together through weaving. As the woven fabric is formed over the corner as a result of fabric shear, the woven layers begin to stack on top of one another increasing the corner thickness. However, because the non-crimp fibers are already stacked as part of their fabric architectures there is a substantial decrease in the corner thickness. This can also be substantiated by looking at the initial fabric thickness with non-crimp fabrics more than twice as thick as woven fabrics.

5.3.3 Data Analysis – Wrinkling

Several assumptions were made regarding the outcome of this DOE investigation for the initiation of the experimental design. The number of fiber layers and corner radii of the rectangular block were assumed to have a direct impact on the wrinkling of the manufactured part with an increase in fiber layers and a decrease in radii corresponding to an increase in the likelihood of wrinkles forming. Factors such as fiber type and fabric textile structure were unknown as to their effects on wrinkling within the experimental investigation.

In analyzing the half normal plot for wrinkling, as shown in Figure 5.22, two two-factor interactions, BD (number of layers and fabric textile structure) and CD (fiber type and fabric textile structure), and two main effects, B (# of layers) and D (fabric textile structure), where shown to potentially affect wrinkling of the part.

This research analyzed the interaction and main effect to show possible aliases. For the DOE investigation of the rectangular block with varying radii there are no aliases. For a full factorial DOE there are no aliases since all possible combinations of experiments are performed.

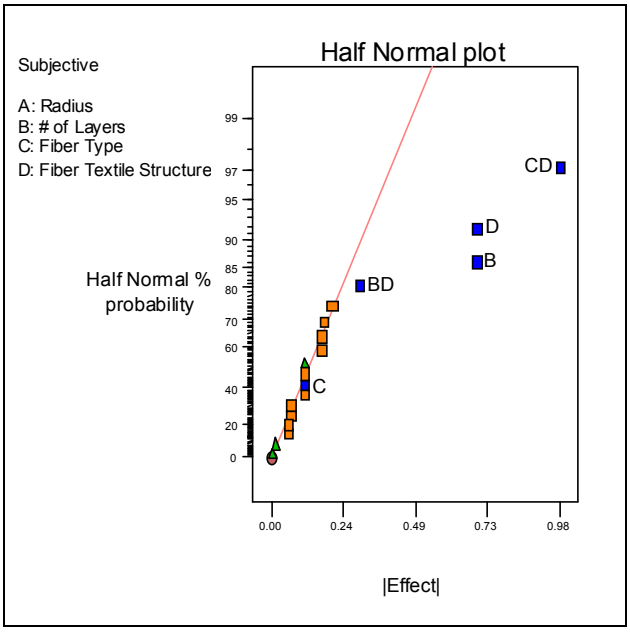

Figure 5.22 Half Normal Plot for Wrinkling

The next step for the analysis was to build the regression model estimating equation for wrinkling. The ANOVA table for wrinkling is illustrated in Table 5.7. From this table, a low p-value is shown for the model signifying the model to be significant. The p-value used the data to test the hypothesis showing the significance of the factors. A p-value less than 0.05 is generally said to be significant. The table also shows the factors B (# of layers), C (fiber type) and D (fabric textile structures) and the interactions BD (number of layers and fabric textile structure) and CD (fiber type and fabric textile structure) to be significant with a p-value < .05.

The next step is to evaluate the effect graphs to better understand how changes with a particular factor or two-factor interaction affect the wrinkling of the part. Figure 5.23 illustrates the BD (number of layers and fabric textile structure) interaction and how varying the number of fiber layers vs. the fiber type affects the wrinkling of the part. From this figure it is shown that for glass fiber, when increasing the fiber layers from three to six, the degree of wrinkling increases with woven fabric having a higher degree of wrinkling. However, for carbon fabric when increasing the fiber layers from three to six the knitted fiber has a higher degree of wrinkling with both knitted and woven increasing in degree of wrinkling.

Table 5.7 ANOVA For Wrinkling

Use your mouse to right click on individual cells for definitions.

Response: Subjective

ANOVA for Selected Factorial Model

Analysis of variance table [Partial sum of squares]

Source	Sum of Squares	DF	Mean Square	F Value	Prob > F	
Block	0.31	1	0.31			
Model	10.21	5	2.04	21.68	< 0.0001	significant
B	*2.45*	*1*	*2.45*	*26.00*	*0.0002*	
C	*0.063*	*1*	*0.063*	*0.66*	*0.4301*	
D	*1.20*	*1*	*1.20*	*12.73*	*0.0034*	
BD	*0.45*	*1*	*0.45*	*4.78*	*0.0478*	
CD	*4.80*	*1*	*4.80*	*50.94*	*< 0.0001*	
Residual	1.23	13	0.094			
Cor Total	11.75	19				

The Model F-value of 21.68 implies the model is significant. There is only a 0.01% chance that a "Model F-Value" this large could occur due to noise.

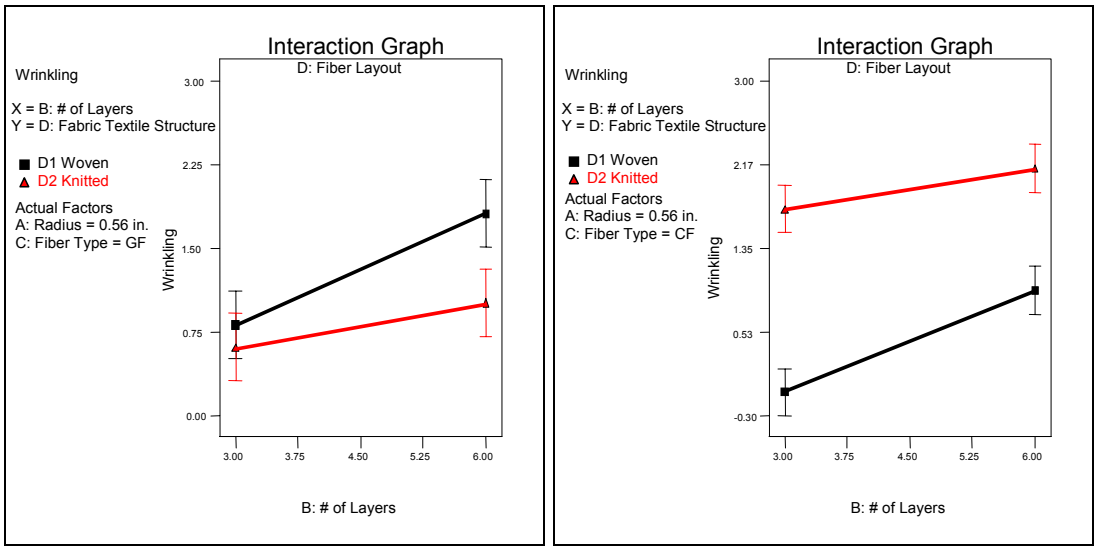

Figure 5.23 BD (Number of Layers and Fabric Textile Structure) Interaction

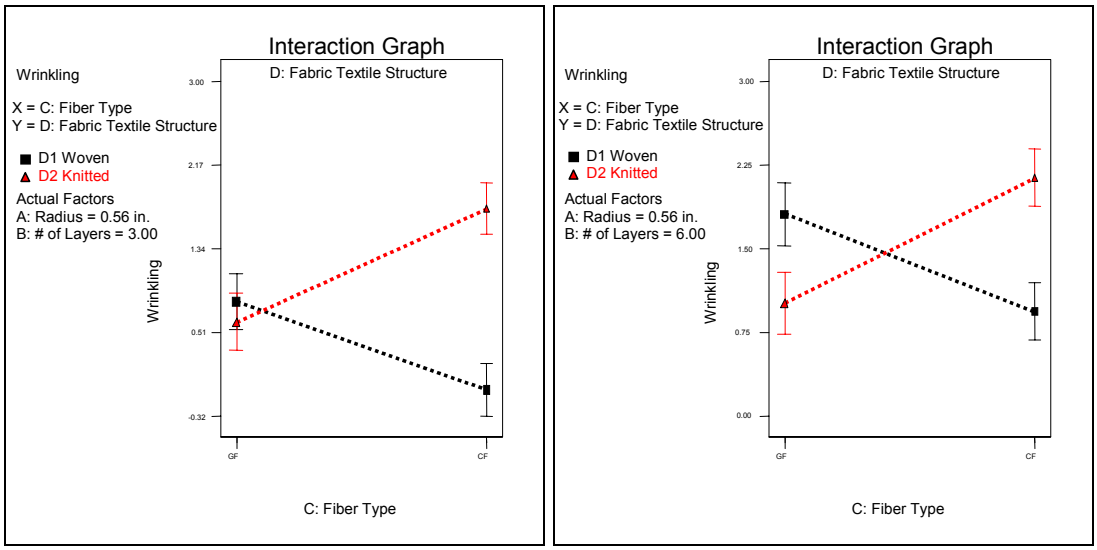

Figure 5.24 CD (Fabric Type and Fabric Textile Structure) Interaction

Figure 5.24 illustrates the CD (fiber type and fabric textile structure) interaction. For three layers of fabric it is shown that glass fabric has the same statistical probability of wrinkling for both woven and knitted. However, for carbon fabric the knitted fabric has a much higher degree of wrinkling. For six layers of fabric it is shown that woven glass fabric has a higher degree of

wrinkling as compared to knitted glass fabric. However, for carbon fabric the knitted fabric has a much higher degree of wrinkling as compared to the woven fabric.

5.3.4 Wrinkling Summary

The BD (number of layers and fabric textile structure) interaction shows that for glass fiber, when increasing the fiber layers from three to six, the degree of wrinkling increases with woven fabric having a higher degree of wrinkling. For carbon fabric when increasing the fiber layers from three to six the knitted fiber has a higher degree of wrinkling with both knitted and woven increasing in degree of wrinkling. This can be explained by the increase in interactions that occur between fiber layers. The addition of 3 layers creates an additional 3 contact interfaces where friction forces further resist inter-ply slip.

The CD (fiber type and fabric textile structure) interaction shows for three layers of fabric, glass fabric has the same statistical probability of wrinkling for both woven and knitted. However, for carbon fabric the knitted fabric has a much higher degree of wrinkling. This can be partially verified by looking at the picture frame tests with woven carbon fabric having a higher locking angle as compared to the non-crimp carbon fabric. For six layers of fabric it is shown that woven glass has a higher degree of wrinkling as compared to knitted glass. This can also be partially verified through the picture frame results as the woven glass fabric requires a much higher force to sustain fabric shear. However, for carbon fabric the knitted fabric has a much higher degree of wrinkling as compared to the woven fabric. From initial friction tests it is shown for woven fabrics the inter-ply friction coefficients are lower as compared to the non-crimp carbon fabric. A prediction equation is given for wrinkling in Equation 5.4.

$$\text{Wrinkling} = 1.13+0.35*B+0.062*C+0.25*D-0.15*B*D+0.50*C*D \qquad \text{Equation (5.4)}$$

5.4 Case Studies of RIDFT Simulation

The intent of the case studies for the RIDFT simulation is to demonstrate the ability of the software to accurately predict drapability of fabric within the RIDFT process. From these studies it will be shown that a good correlation exists between the simulation results and experimental results. The boundary conditions for the model are detailed in section 3.2, Modeling and Simulation of The RIDFT Process and Chapter 4, Material Characterization. The

results obtained are specific to the material properties given and the boundary conditions defined. No external force was applied to the part during forming for the case studies.

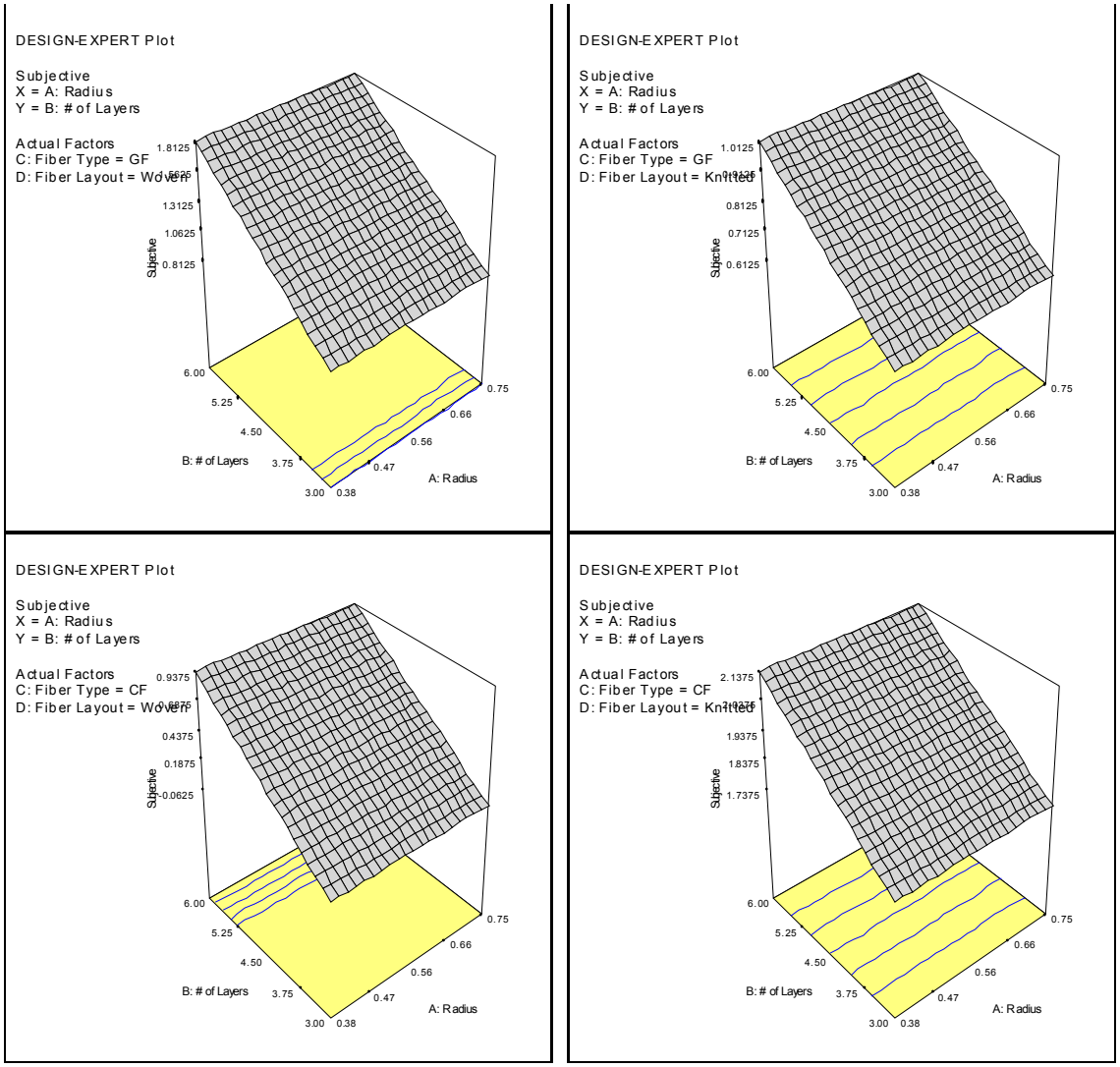

Figure 5.25 Response Surface of Wrinkling for the 4 Fabric Types

The case studies are performed utilizing the RIDFT simulation model. Within the model, the tool and vacuum chamber mesh contain 2191 nodes and 2443 elements. Each silicone mesh contains 3210 nodes and 3074 elements. The standard mesh size of the fiber for the simulations

is 0.25 inches, with each fiber mesh layer containing 593 nodes and 538 elements. The mesh independence case studies utilizes fiber meshes of various sizes. For a fiber mesh size of 0.5 inches, it contains 160 nodes and 132 elements. For a fiber mesh size of 0.125 inches, it contains 2261 nodes and 2152 elements. Finally, for a mesh size of 0.0625 inches, it contains 8825 nodes and 8608 elements.

5.4.1 Mesh Independence

It is important to understand the effects of fiber mesh size on both the computing time required to run a simulation and on the results obtained from that simulation. Four case studies were performed. The specific sizes tested for the fiber meshes were 0.5000 inches, 0.2500 inches, 0.1250 inches and 0.0625 inches. The case studies simulated 3 layers of woven carbon fiber forming over a 4-inch diameter half-sphere as used in the DOE section of this report. Figure 4.26 illustrates the results of the simulation runs for the various fiber mesh sizes.

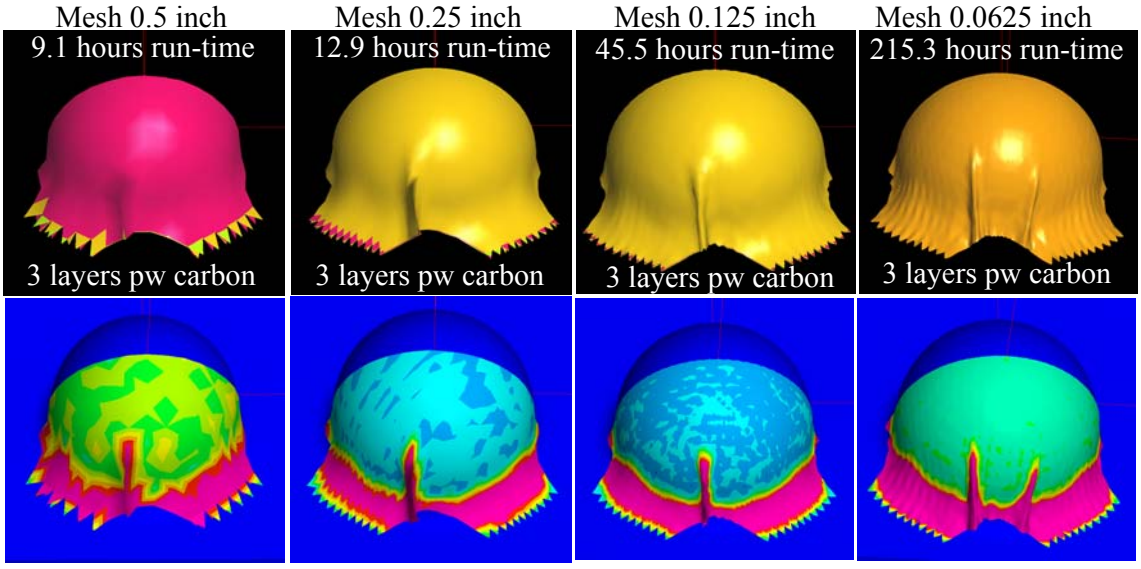

Figure 5.26 Mesh Independence

It is shown that with a decrease in mesh size there is a corresponding increase in computing time. For mesh sizes of 0.5000 inches and 0.2500 inches the computing time difference is 3.8 hours, but from 0.2500inches to 0.125 inches and from 0.125 inches to 0.0625 inches the

computing time difference is 32.6 hours and 169.8 hours, respectively. Also, a decrease in mesh size increases the resolution of the simulation results while the principle wrinkle size and location remains the same. However, with a mesh size of 0.0625 inches a secondary wrinkle has occurred.

5.4.2 Five-Inch Sphere – Plain Weave Carbon Fiber

This simulation case study investigates the ability of the RIDFT simulation model to accurately predict the formability of fabric to form over a half-sphere. More specifically, 1, 3 and 6 layers of plain weave carbon fiber will be formed over a 5-inch sphere both experimentally and using the RIDFT simulation model. Figure 4.27 illustrates the results of the RIDFT simulation model vs. the experimental results.

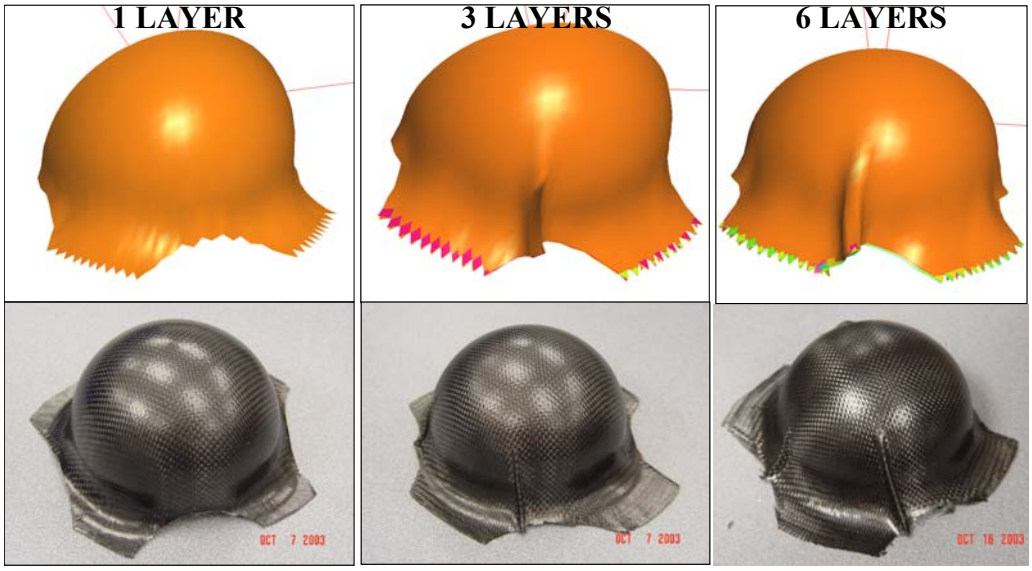

Figure 5.27 Five-Inch Sphere – Plain Weave Carbon Fabric

The RIDFT simulatio model results show the plain weave carbon fiber successfully formed over the half-sphere with no occurrence of wrinkling for 1 layer and a single wrinkle occurring for 3 and 6 layers. The RIDFT simulation results show wrinkling occurred at the same relative

locations on the part for 3 and 6 layers for both the PAMFORM simulation and the experimental results. The PAMFORM simulation results are in agreement with the experimental results.

5.4.3 Five-Inch Sphere – Non-Crimp Glass Fiber

This simulation case study investigates the ability of the PAMFORM software to accurately predict the formability of fabric to form over a half-sphere. More specifically, 1, 3 and 6 layers of non-crimp glass fiber will be formed over a 5-inch sphere both experimentally and using the RIDFT simulation model. Figure 4.28 illustrates the results of the RIDFT simulation vs. the experimental results.

The results show the glass non-crimp fiber successfully formed over the half-sphere with a single wrinkle occurring for 1, 3 and 6 layers. The RIDFT simulation results show wrinkling occurred at the same relative locations on the part for 3 and 6 layers for both the RIDFT simulation and the experimental results. However, the experimental results for 1 layer show no wrinkling, while the simulation results showed a small wrinkle. The RIDFT simulation results are in agreement with the experimental results.

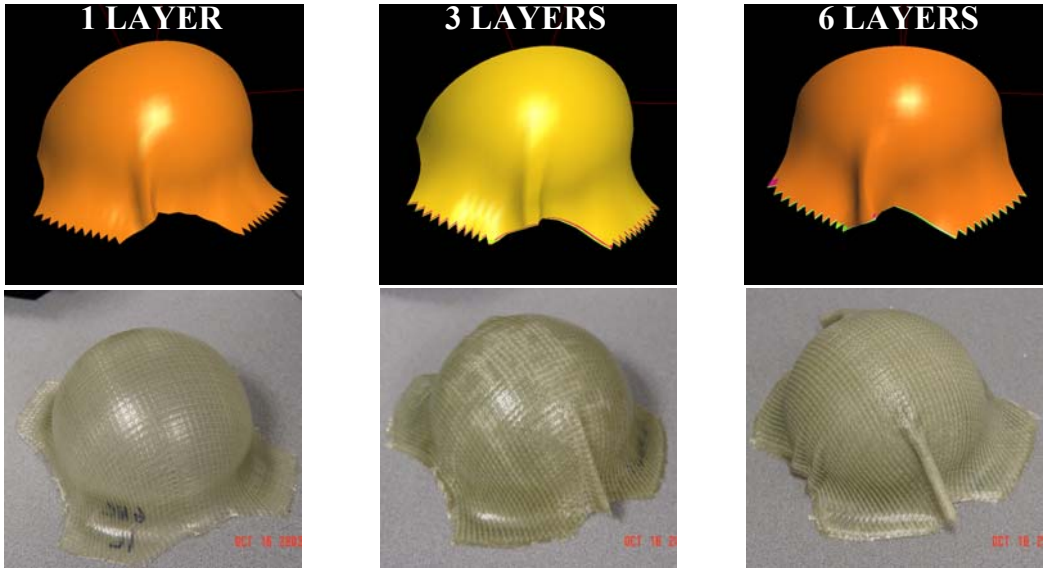

Figure 5.28 Five-Inch Sphere – Non-Crimp Glass Fabric

5.4.4 Resin Content Effects on Formability

It has been noted through experimental investigation the effects of resin content on the formability of the 5-inch half-sphere while using plain weave carbon fiber. With an increase in resin content there is a decrease in the wrinkling of the part. It is suggested the resin acts to reduce inter-ply friction (fiber-to-fiber) and also reduces intra-ply friction, which reduces the force require to create fabric shear.

Four case studies where run within the RIDFT simulatio model to see the effects of reducing inter-ply friction and intra-ply friction (shear force) on wrinkling. A baseline case was run simulating 1 layer of non-crimp glass fiber. From the baseline run a slight wrinkle appears in the center of the part. For the first case study, the fiber-silicone friction was doubled and the results show an increase in the wrinkle created. For the second case study, the shear modulus was increased by 5 psi and the results also show an increase in the wrinkle created. For the third case study the fiber-silicone friction was reduced by half and the results show no wrinkle present. For the final case study, the shear modulus was decreased by 5psi and the results show no wrinkle present. Figure 5.29 illustrates the results of resin content effects on formability within the RIDFT simulation.

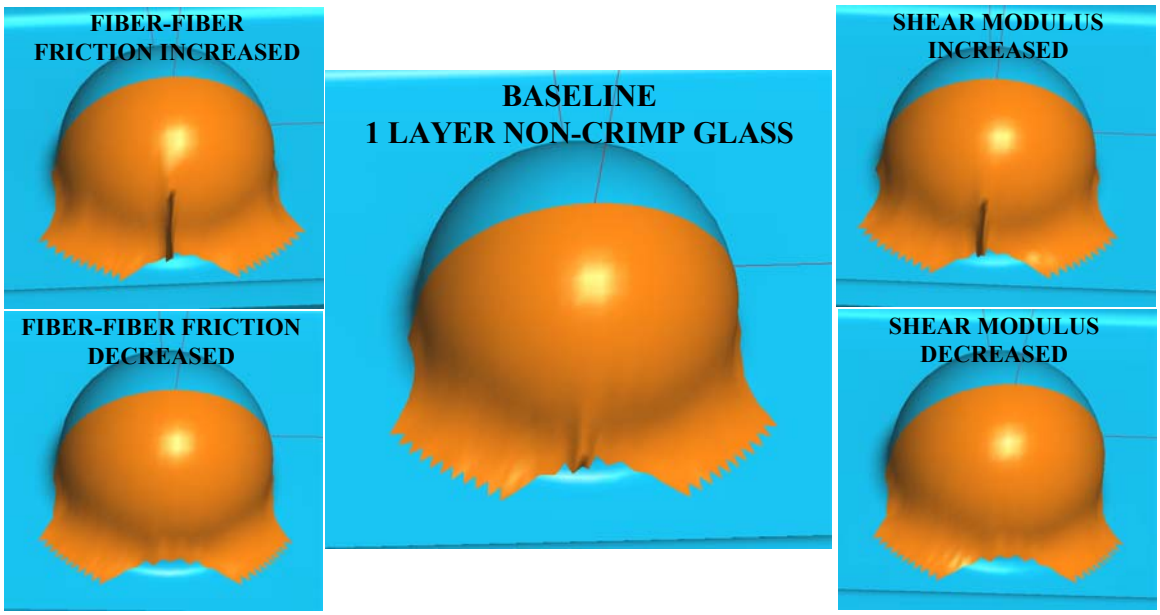

Figure 5.29 Resin Content Effects on Formability

Simulation Case	Coulomb friction coefficient	Results
1	μ (benchmark)	No wrinkle
7	μ x 2	1 wrinkle (Figure 6a)
8	μ x 3	3 wrinkles (Figure 6b)

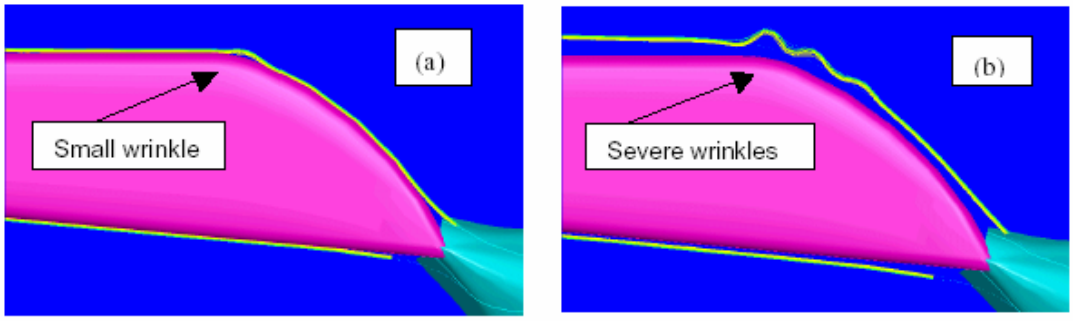

Figure 5.30 Parameter Study on Fabric-To-Fabric Friction [25]

Cartwright and Paton noted the PAMFORM simulations show that the prepreg viscosity is a critical parameter on forming quality with wrinkles developing when the viscosity parameter was increased by 20 to 30 times [25]. Further studies by Cartwright and Paton suggest that successful forming is very sensitive to the inter-ply friction [25]. Figure 5.30 illustrates the effects of friction in inter-ply shearing with a doubling and tripling of the coulomb friction increasing the presence of wrinkles.

5.4.5 Block with 0.75 Inch Radius – Plain Weave Carbon Fiber

This simulation case study investigates the ability of the PAMFORM software to accurately predict the formability of fabric to form over a rectangular block with corner radii of 0.75 inches. More specifically, 1, 3 and 6 layers of plain weave carbon fiber will be formed over a rectangular block both experimentally and using the RIDFT simulation model. Figure 4.31 illustrates the results of the RIDFT simulation vs. the experimental results.

The RIDFT simulation results show the plain weave carbon fiber successfully formed over the rectangular block with the occurrence of wrinkling for 1, 3 and 6 layers. The PAMFORM simulation results show wrinkling occurred at the same locations on the part. This location is on each of the part corners. For this case study, the RIDFT simulation results are in agreement with the experimental results.

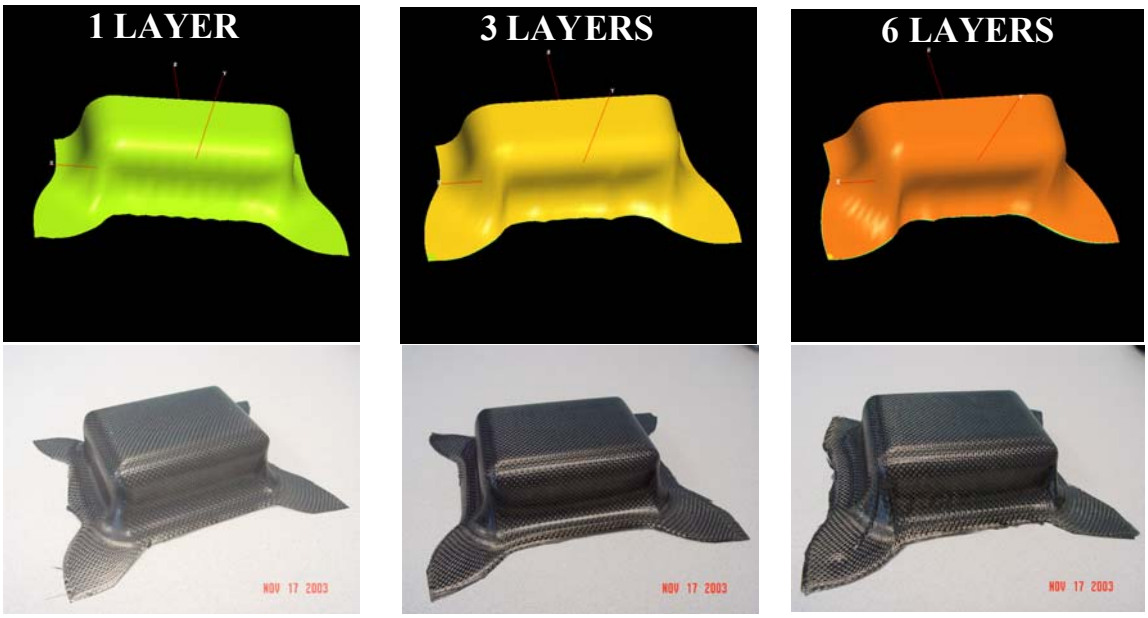

Figure 5.31 Block with 0.75-Inch Radius – Plain Weave Carbon Fabric

5.4.6 Mechanics of Wrinkling

From the case studies performed there has been a great understanding of the mechanics which create wrinkling of the finished part. Several key parameters are associated with a fabrics ability to form with or without wrinkles. The interactions of fiber-to-fiber and fiber-to-silicone as well as the fabric's shear modulus have been shown to directly affect a fibers ability to form without wrinkles for the 5 inch half-sphere case studies of resin content. Other significant factors affecting this ability are the silicone-to-tool friction, which is difficult to overcome. Once the silicone contacts the tool surface it tends to stay in the contact location with minimal sliding, making shearing of the fabric difficult.

The silicone is also shown to affect the forces exerted onto the fabric during forming. The RIDFT vacuum chamber is rectangular in shape with two long sides and two short sides with respect to the tool placement. The lack of extra silicone on the tool short-side gives rise to uneven forces exerted on the fabric by the silicone during forming. This uneven distribution of forces directly affects the fabrics ability to form evenly and thus, contributes to the wrinkling in the 5-inch sphere case studies.

5.4.7 Case Study Conclusions

For the mesh independence case studies performed it is shown the simulation results are largely mesh independent. However, with a decrease in mesh size to 0.0625 inches it is observed that a secondary wrinkle occurs unlike the results for the larger mesh sizes. It is also shown that a decrease in mesh size creates an increase in graphical resolution of the simulation. Decreasing the mesh size is shown to increase simulation time with a simulation time of 215 hours for a mesh size of 0.0625 inches.

It has been noted through experimental investigation and the RIDFT simulation model the effects of resin content on fabric formability. With an increase in resin content there is a decrease in the wrinkling of the part. The resin acts to reduce inter-ply friction (fiber-to-fiber) and also reduces intra-ply friction, which reduces the shear modulus.

The ability of the RIDFT process to form various part geometries has been proven successful in many instances. The forming of resin infused fiber reinforcements from a flat shape into a finished geometry is unique with many deformation mechanics involved. Using PAMFORM's unique capability of composite diaphragm forming, the RIDFT simulation model has been successfully developed. The models include multiple layers of resin-impregnated fiber reinforcements and well-characterized material properties.

The RIDFT simulation model is shown to be a powerful tool for understanding and predicting drapability and fiber deformation. In particular, the complicated interactions of fiber-fiber, fiber-silicone, silicone-tooling and silicone-silicone contacts can be defined based on the process forming mechanics and friction test results. The simulation results are in good agreement with those of the experimental results for the half-sphere and the rectangular block. The research results show PAMFORM is an effective tool for the simulation of the RIDFT process.

CHAPTER 6

RESULTS AND DISCUSSION

6.1 RIDFT Process

In the innovative RIDFT process, resin is infused between two flexible tools through fiber reinforcements in a two-dimensional flat shape. The wetted reinforcements and flexible tooling are then formed over a mold into a specified part shape by use of vacuum. Elements of the technology include means to help distribute the resin within the fiber, methods of mold manipulation, sealing frame design, and computer simulations to predict drapability and fiber deformation.

The RIDFT process combines the precise thickness and finish quality of resin infusion molding for large parts, with the low tool and process cost of vacuum bagging over a male mold. This process has potential for large composite structures.

6.1.1 Industrial RIDFT Machine

The industry grade RIDFT machine was successfully developed with the knowledge gained from a thorough understanding of the RIDFT process, information gathered from the design and use of the initial RIDFT prototype. The RIDFT machine utilizes a large vacuum chamber, reliable and easy operation of vacuum sealing and reducing flexible tooling stretch into the design so that it is suitable for the size of the largest desired part to be made. For the sponsored research, a part dimension no larger than 5 feet (width) x 10 feet (length) x 1 foot (height) was required. The results for the demonstration of the industrial RIDFT machine have yielded good results. Many parts have been successfully produced using the industrial RIDFT machine.

The sealing frame design was a critical aspect of the RIDFT process development. It is important for the sealing frame to maintain vacuum integrity during the process. It is also important for the sealing frame to be quickly and easily used so the process is more robust in

nature. In the research, the sealing frame design has developed over four iterations of sealing frame designs, a design was established that has yielded excellent sealing and clamping characteristics while being quickly and easily used.

Another major contribution in the development of the industrial RIDFT machine is dynamic supporting using compressed air. The potential large size of the fabric used on the large machine requires a means by which its weight can be supported during resin infusion. By pressuring the vacuum cavity before resin infusion the weight of the silicone sheets and fiber can be supported so the assembly remains flat.

In addition to this contribution, another major contribution is the creation of temporary distribution channels. The ability to vacuum infuse large parts is limited by the permeability of the fabric being infused. For the larger RIDFT machine it was crucial to develop a means by which large parts could be resin infused by use of vacuum. The creation of a temporary flow channel on the fabric's surface allows resin to quickly and easily wet the fiber before part forming. The flexibility of the temporary distribution channel also allows for multiple gates and vents to be utilized during resin infusion.

The successful development of the industrial RIDFT machine has lead to a patent and several copyrights. The RIDFT process is currently patent pending, Provisional Patent Application No. 60/326,556 and has several copyrights for the RIDFT simulation model, temporary distribution channel, sealing frame design and mold manipulation device, Tech ID: 03-067, 03-082, 03-083, 03-084, and 03-094.

In this research, both DOE and computer simulation were employed to explore the formability and input factors for RIDFT process forming. The ability of the RIDFT process to form various part geometries has been proven successful in many instances. The forming of resin infused fiber reinforcements from a flat shape into a finished geometry is unique with many deformation mechanics involved.

6.2 Design of Experiments (DOE) Investigation

6.2.1 Half-Sphere on Cylinder (Wrinkling)

The DOE results show the main effect A (radius) and how varying the radius of the sphere from 2.5 inches to 2 inches affects the ability of the part to be formed without wrinkles. This

result is understood as the requirements of the fiber to form tight radii are reduced. As the radius of the hemi-sphere is increased, it is seen the likelihood of a wrinkle decreases. Increasing the fiber layers from 6 to 12 increases the likelihood of wrinkling to occur. This can be explained by the increase in interactions that occur between fiber layers. The addition of 6 layers creates an additional 6 contact interfaces where friction forces further resist inter-ply slip and creates additional material stiffness.

It is also shown for woven fabrics, glass fabric has a higher tendency of wrinkling over carbon fabric. There are two possible explanations for this finding. The inter-ply friction for carbon-carbon interfaces is much lower than that of glass-glass interfaces. Next, from the picture frame test results, the force required to sustain shear for the woven glass fabric is 24.66 psi while for woven carbon fabric it is 15.95 psi. This clearly shows the woven carbon fabric is much easier to sustain shear.

For knitted fabrics, carbon fiber has a higher tendency of wrinkling over glass fiber. It is believed these results are based on fiber architecture. Although it is known the inter-ply forces for carbon-carbon interfaces is lower than that of glass-glass interfaces, the ability to overcome fiber architecture limitations prevails. Although the picture frame results show the non-crimp carbon fabric reaches higher locking angles the force required to sustain shear for the non-crimp carbon fabric is higher; 11.02 psi as compared to 7.397 psi for non-crimp glass fabric. Although not fully understood at this time, it is believe the stitching type plays a roll in the ability of a fiber to form over various shapes.

For the CD (fiber type & fabric textile structure) interaction, it is shown the general trend for knitted fiber is an increase in the tendency to wrinkle when going from glass fiber to carbon fiber. It is also shown the general trend for woven fiber is a decrease in the tendency to wrinkle when going from glass fiber to carbon fiber. From initial friction tests it is shown for resin-impregnated carbon fabrics the inter-ply friction coefficients are lower for the woven fabric as compared to the non-crimp carbon fabric, 0.261 and 0.365, respectively.

6.2.2 Rectangular Block (Corner/Sidewall Ratio)

The DOE results show the BD (number of layers and fabric textile structure) interaction to be significant. Varying the number of fiber layers vs. the fiber type affects the corner/sidewall ratio. For the woven fiber, increasing the number of fiber layers from 3-6 increases the corner/sidewall ratio, while for the knitted fiber, increasing the number of fiber layers from 3-6 decreases the

corner/sidewall ratio. This phenomenon is not completely understood, but a plausible explanation can be given.

The knitted fabrics are oriented such that the different fiber orientations exist on different fiber planes with one layer of unidirectional fiber stitched on top another layer of unidirectional fiber. However, the woven fiber co-exists in a single plane as they are bound together through weaving. As the woven fabric is formed over the corner as a result of fabric shear, the woven layers begin to stack on top of one another increasing the corner thickness. However, because the non-crimp fibers are already stacked as part of their fabric architectures there is a substantial decrease in the corner thickness. This can also be substantiated by looking at the initial fabric thickness with non-crimp fabrics being more than twice as thick as the woven fabrics.

6.2.3 Rectangular Block (Wrinkling)

The BD (number of layers and fabric textile structure) interaction shows that for glass fiber, when increasing the fiber layers from three to six, the degree of wrinkling increases with woven fabric having a higher degree of wrinkling. For carbon fabric when increasing the fiber layers from three to six the knitted fiber has a higher degree of wrinkling with both knitted and woven increasing in degree of wrinkling. This can be explained by the increase in interactions that occur between fiber layers. The addition of 3 layers creates an additional 3 contact interfaces where friction forces further resist inter-ply slip.

The CD (fiber type and fabric textile structure) interaction shows for three layers of fabric, glass fabric has the same statistical probability of wrinkling for both woven and knitted. However, for carbon fabric the knitted fabric has a much higher degree of wrinkling. This can be partially verified by looking at the picture frame tests with woven carbon fabric having a higher locking angle as compared to the non-crimp carbon fabric. For six layers of fabric it is shown that woven glass has a higher degree of wrinkling as compared to knitted glass. This can also be partially verified through the picture frame results as the woven glass fabric requires a much higher force to sustain fabric shear. However, for carbon fabric the knitted fabric has a much higher degree of wrinkling as compared to the woven fabric. From initial friction tests it is shown for woven fabrics the inter-ply friction coefficients are lower as compared to the non-crimp carbon fabric.

6.3 Development and Demonstration of RIDFT Simulation Model

This research is trying to develop the model for the simulation of the RIDFT process using the PAMFORM finite element software from Engineering Systems International. This is being achieved from a review of resin infusion and diaphragm forming processes with an understanding of the governing phenomena's during RIDFT forming. This research will create a working RIDFT simulation model with some validations through experimentation. The key expected results from the simulation include formability and visualization of wrinkles, which all us to predict the problems and influence factors of RIDFT forming.

Several key input parameters will be necessary for the model to determine the output. The drapability of resin-wetted fabrics and silicone rubber membranes have a direct impact on RIDFT forming. There are four distinct interactions during forming. These interactions include fiber-to-silicone, fiber-to-fiber, silicone-to-silicone and silicone-to-tooling. They are all dynamic interactions. In this research there was a need to fully characterize these material properties and interactions in order to accurately model the forming process of RIDFT. Characterization results from Chapter 4 were focused on developing the simulation model of the RIDFT process and conducting the case studies.

For the mesh independence case study performed it is shown the simulation results are largely mesh independent. However, with a decrease in mesh size to 0.0625 inches it is observed that secondary wrinkles occur unlike the results for the larger mesh sizes. It is also shown that a decrease in mesh size creates an increase in graphical resolution of the simulation. Decreasing the mesh size is shown to increase simulation time with a simulation time of 215 hours for a mesh size of 0.0625 inches. Therefore, a desired mesh density of 0.25" is used as it provides sufficient resolution of results while maintaining quick simulation speed.

It has been noted through experimental investigation and RIDFT simulations the effects of resin content on fabric formability. With an increase in resin content there is a decrease in the wrinkling of the part. The resin acts to reduce inter-ply friction (fiber-to-fiber) and also reduces intra-ply friction, which reduces the force require to create fabric shear.

From the case studies performed there has been a great understanding of the mechanics which create wrinkling of the finished part. Several key parameters are associated with a fabrics ability to form with or without wrinkles. The interactions of fiber-to-fiber and fiber-to-silicone

as well as the fabric's shear modulus have been shown to directly affect a fibers ability to form without wrinkles for the 5 inch half-sphere case studies of resin content. Other significant factors affecting this ability are the silicone-to-tool friction, which is difficult to overcome. Once the silicone contacts the tool surface it tends to stay in the contact location with minimal sliding, making shearing of the fabric difficult.

The silicone is also shown to affect the forces exerted onto the fabric during forming. The RIDFT vacuum chamber is rectangular in shape with two long sides and two short sides with respect to the tool placement. The lack of extra silicone on the tool short-side gives rise to uneven forces exerted on the fabric by the silicone during forming. This uneven distribution of forces directly affects the fabrics ability to form evenly and thus, contributes to the wrinkling in the 5-inch sphere case studies.

The ability of the RIDFT process to form various part geometries has been proven successful in many instances. The forming of resin infused fiber reinforcements from a flat shape into a finished geometry is unique with many deformation mechanics involved. Using PAMFORM's unique capability of composite diaphragm forming, RIDFT process simulation models have been successfully developed. The models include multiple layers of resin-impregnated carbon fiber reinforcements and well-characterized material properties.

The simulation revealed the mechanisms and important factors for formability and drapability of the process. It shows that unbalanced shear deformation and locking angle are major reasons for wrinkling. The RIDFT simulation model is shown to be a powerful tool for understanding and predicting drapability and fiber deformation. In particular, the complicated interactions of fiber-fiber, fiber-silicone, silicone-tooling and silicone-silicone contacts can be defined based on the process forming mechanics and friction test results. The simulation results are in good agreement with those of the experimental results. The research results show PAMFORM is an effective tool for the simulation of the RIDFT process.

6.4 Academic Publications

From this research several academic works have been published and presented. These works include the following:

- Thagard, J.R., Okoli, O.I. and Liang, Z., "Resin Infusion between Double Flexible Tooling, Evaluation of Process Parameters," 35th International SAMPE Technical Conference, 2003 [27].
- Thagard, J.R., Liu, Q., Liang, Z., Okoli, O.I. and Wang, H.P., "Simulation of the Resin Infusion Between Double Flexible Tooling Process and Experimental Validation," AmeriPAM Conference, 2003 [28].
- Thagard, J.R., Okoli, O.I., Liang, Z., Wang, H.P. and Zhang, C., "Resin infusion between double flexible tooling: prototype development," *Composites Part A*, 2003 [29].
- Thagard, J.R., Okoli, O.I. and Liang, Z., "Resin Infusion between Double Flexible Tooling, Evaluation of Process Parameters," accepted JRPC, October, 2003 [30].

APPENDIX A

DOE EXPERIMENTAL RESULTS – HALF SPHERE

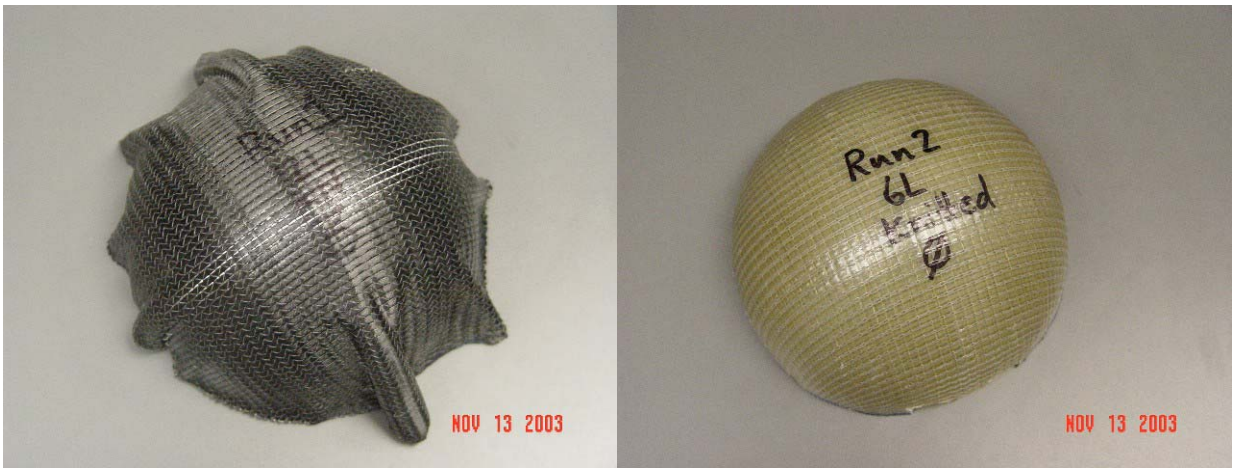

Runs 1 and 2

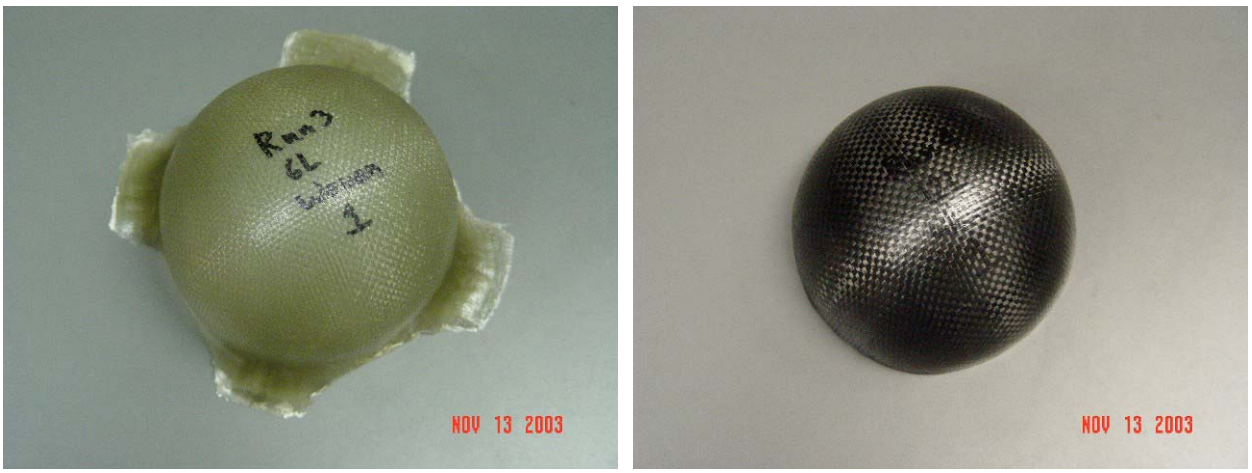

Runs 3 and 4

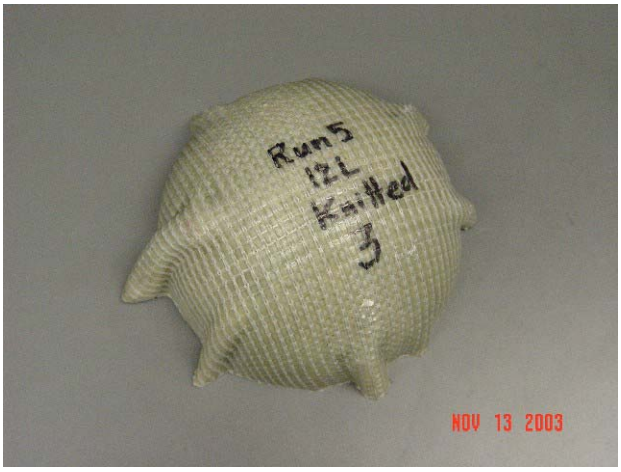

Runs 5 and 6

Runs 7 and 8

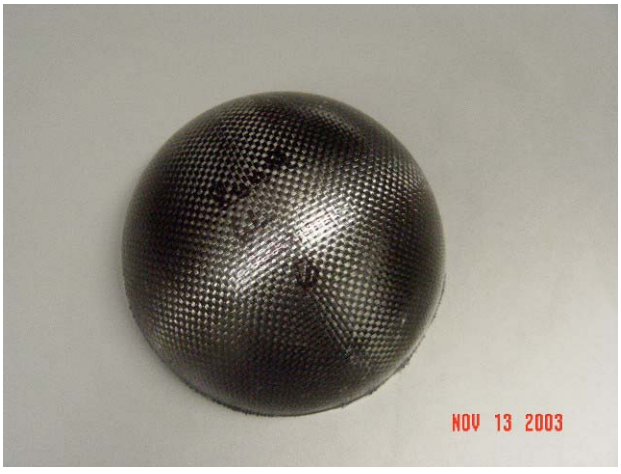

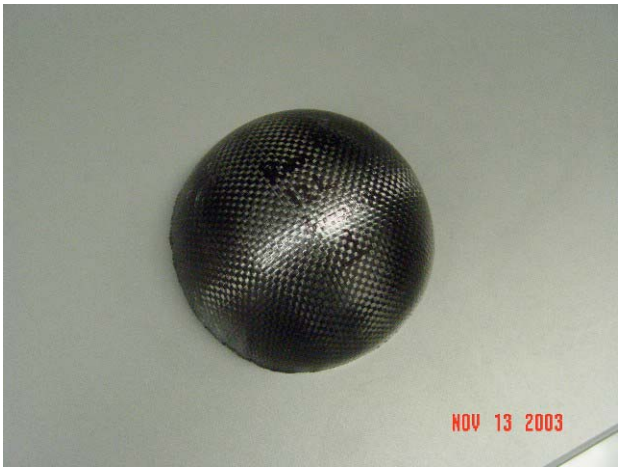

Runs 9 and 10

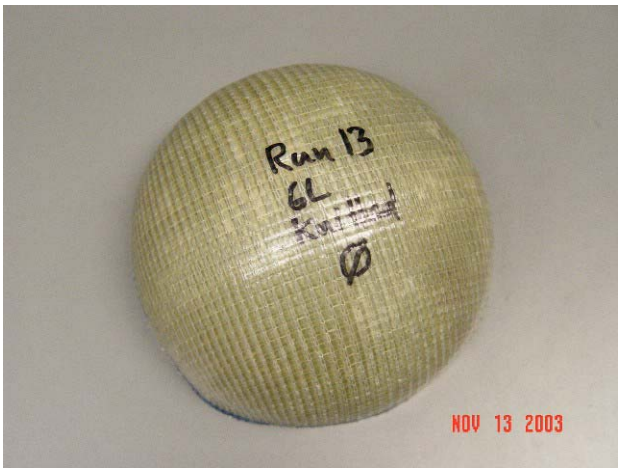

Runs 13 and 14

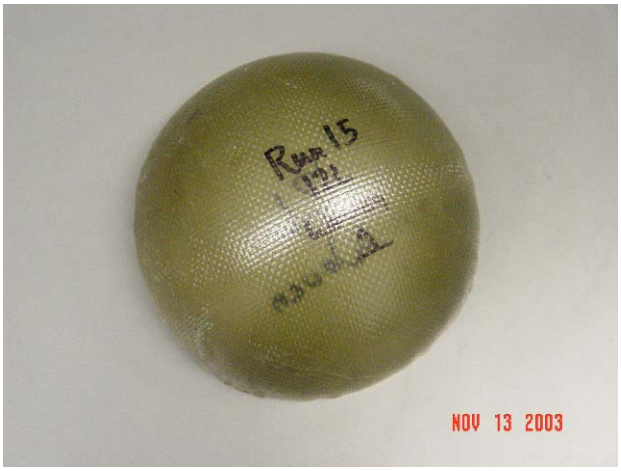

Runs 15 and 16

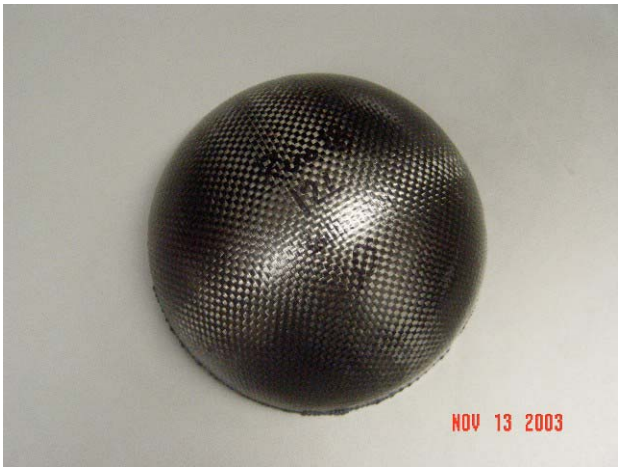

Runs 17 and 18

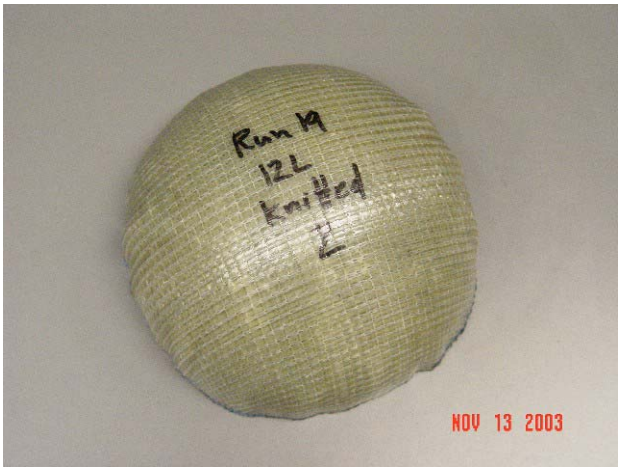

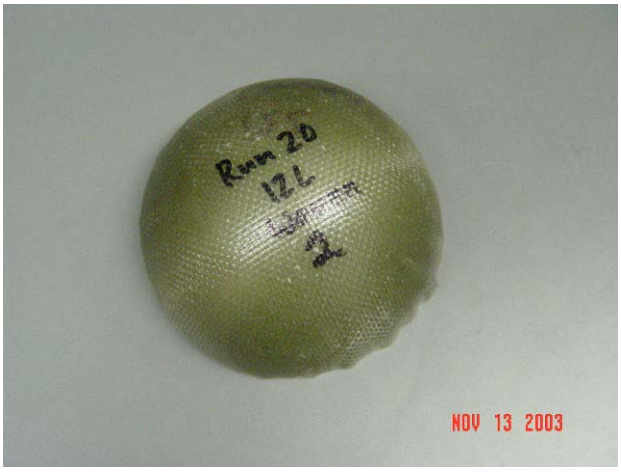

Runs 19 and 20

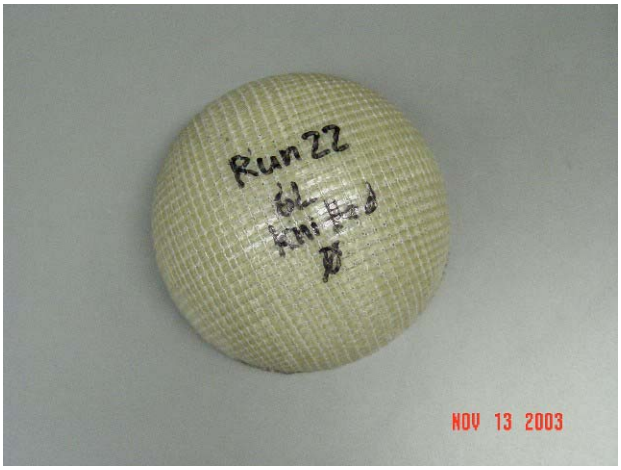

Run 22 and Validation Run 1

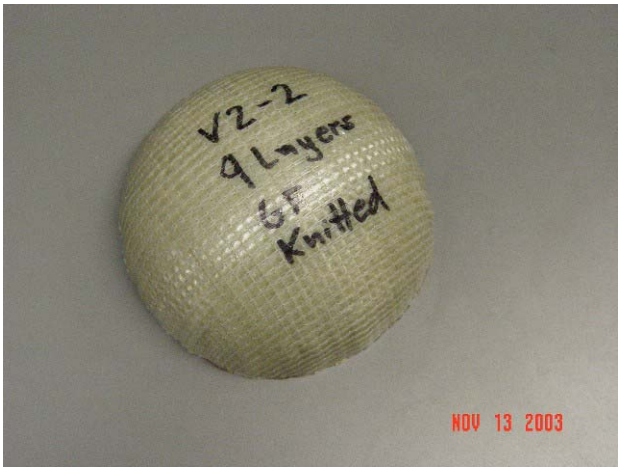

Validation Run 2

APPENDIX B

DOE EXPERIMENTAL RESULTS – RECTANGULAR BLOCK

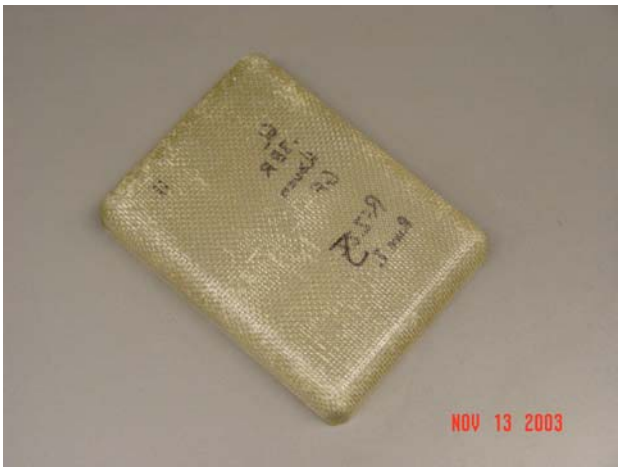

Runs 1 and 2

Runs 3 and 4

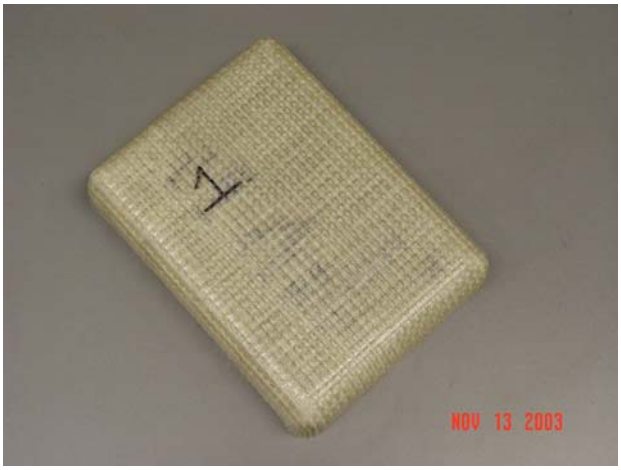

Runs 5 and 6

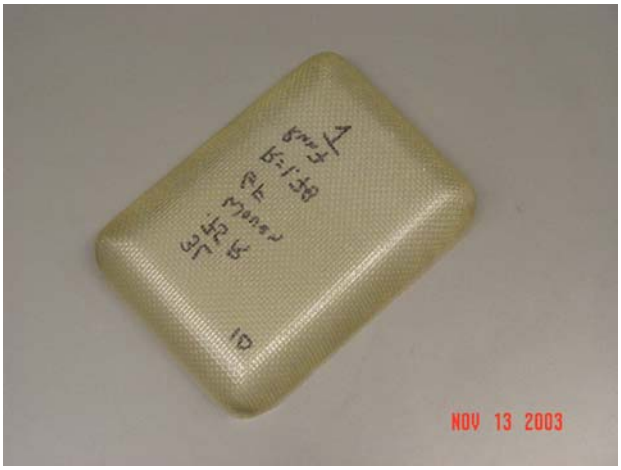

Runs 7 and 8

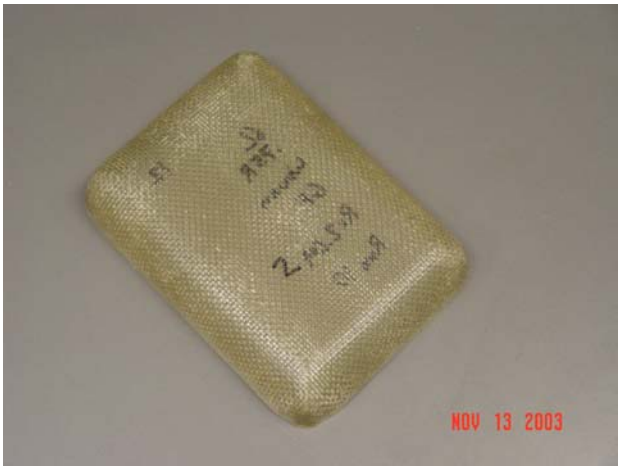

Runs 9 and 10

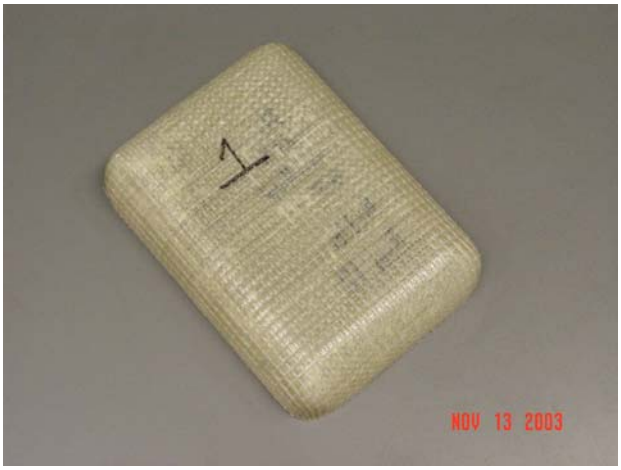

Runs 11 and 12

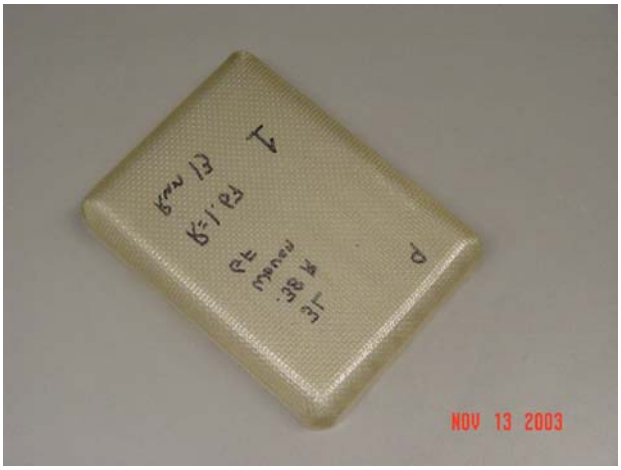

Runs 13 and 14

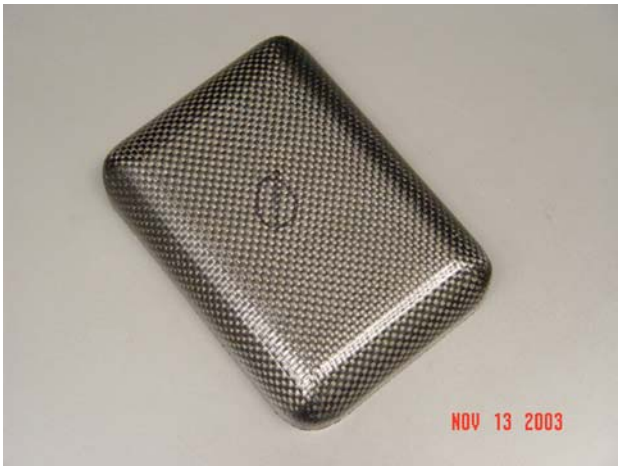

Runs 15 and 16

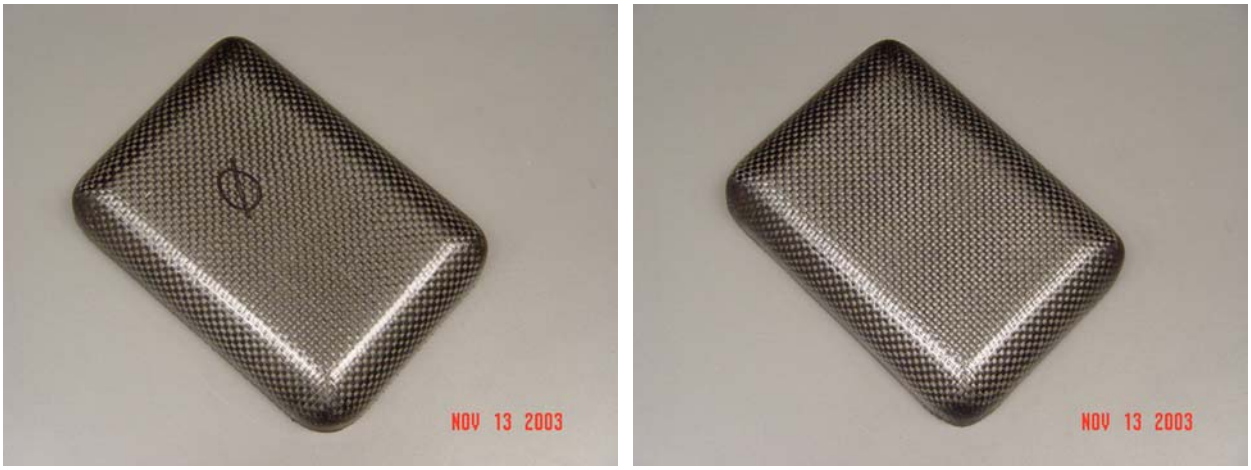

Runs 17 and 18

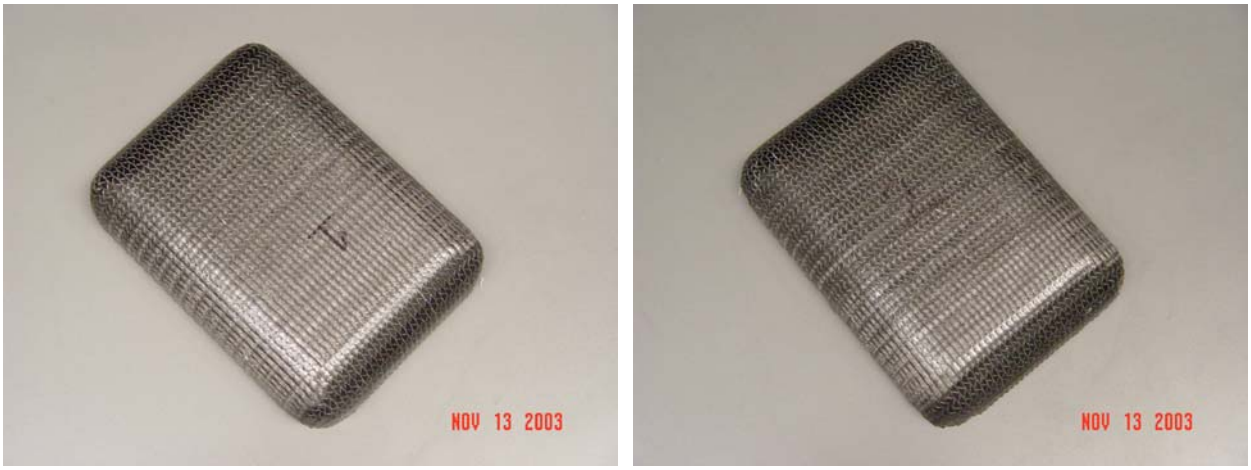

Runs 19 and 20

REFERENCES

[1] Thagard, James, "The Development of the Resin Infusion Between Double Flexible Tooling Process," *Masters Thesis*, Fall 2001.

[2] Williams, C.D., Grove, S.M. and Summerscales, J., "Resin Infusion under Flexible Tooling (RIFT): A Review," *Composites Part A*, 1996, pp. 517-p524.

[3] Williams, C.D., Grove, S.M. and Summerscales, J., "The Compression Response of Fiber-Reinforced Plastic Plates during Manufacturing by the Resin Infusion under Flexible Tooling Method," *Journal of Composites Materials*, Vol. 29, No.3, 1995, pp. 306-316.

[4] Williams, C.D., Grove, S.M. and Summerscales, J., "The Compression Response of Fiber Beds Subjected to Repeated Loading Cycles in the Resin Infusion under Flexible Tooling (RIFT) Manufacturing Process," *Journal of Composites Materials*, Vol. 29, No.3, 1995, pp. 306-316.

[5] Pearce, N. and Summerscales, J., "The Compressibility of a Reinforcement Fabric," *Composites Manufacturing*, 1995, pp.15-21.

[6] Foley, M.F., "The Flexible Resin Transfer Molding (FRTM) Process," *Sampe Journal*, Vol. 28, No. 6, 1992, pp. 15-24.

[7] Sevostianov, I.B., Verijenko, V.E., von Klemperer, C.J. and Chevallereau, B., "Mathematical model of stress formation during vacuum resin infusion process," Composites Part B, 1999, pp. 513-521.

[8] http://biosystems.okstate.edu/darcy/

[9] Sun, X., Li, S. and Lee, J., "Mold Filling Analysis in Vacuum-Assisted Resin Transfer Molding. Part I: SCRIMP Based on a High-Permeable Medium," Polymer Composites, 1998, pp. 807-817.

[10] Rozant, O., Bourban, P.-E. and Manson, J.-A.E., "Drapability of dry textile fabrics for stampable thermoplastic performs," *Composites Part A*, 2000, pp. 1167-1177.

[11] Young, M. and Paton, R., "Diaphragm Forming of Resin Pre-impregnated Woven Carbon Fiber Materials," 33rd International SAMPE Technical Conference, November 5-8, 2001.

[12] Dujardin, E., Ebbesen, T.W., Hiura, H. and Tanigaki, K., "Capillarity and Wetting of Carbon Nanotubes," *Science Vol. 265*, 1994, pp. 1850-1851.

[13] Kurumada, T.O., Harada, K., Kawamata, K., Sato, S. and Hiraoda, T., "Effects Of Burn-off on Thermal Shock Resistances of Nuclear Carbon Materials," *Carbon Vol. 35*, .1997, pp 1157-1165.

[14] ESI Group, Solver Reference Manual for PAMFORM 2002. *PAM-THEORY Manual*, Engineering Systems International, 99 Rue des Solets, Silic 112, 94513 Rungis-Cedex, France.

[15] ESI Training notes, January 2003.

[16] ASTM G115-98 –Standard Guide for Measuring and Reporting Friction Coefficients, 2000.

[17] ASTM D1894-01 –Standard Test Method for Static and Kinetic Coefficients of Friction of Plastic Film and Sheeting, 2000.

[18] ASTM D412-98a(2002)e1 –Standard Test Methods for Vulcanized Rubber and Thermoplastic Elastomers—Tension, 2000.

[19] ASTM D3183-02 –Standard Practice for Rubber—Preparation of Pieces for Test Purposes from Products, 2000.

[20] Persson, B.N.J., "Sliding Friction – Physical Principles and Applications," 2000.

[21] Long A C. An Iterative Draping Simulation Based on Fabric Mechanics. *4th International ESAFORM Conference on Material Forming.* 23-25th April 2001, Belgium, Liege, pp 99-102.

[22] Clifford M J, Long A C. Intra-ply Shear of Textile Composites. *Proceedings of the 8th International Conference on Fibre Reinforced Composites. 13-15 September 2000. United Kingdom, Newcastle upon Tyne.*

[23] Montegomery, D.C., Design and Analysis of Experiments, 5th edition. Wiley, New York, 1997.

[24] Notes from James R. Simpson, Ph.D., Professor, Department of Industrial Engineering, FAMU-FSU College of Engineering, June, 2001.

[25] Yu, X., Cartwright, B.K., Zhang, L., Paton, R. and Mai, Y.-W., "Finite Element Simulations of the Diaphragm Forming Process," 2003.

[26] *Porous Aluminum Mold Technology*, International Mold Steel, Inc., p. 1, 2000.

[27] Thagard, J.R., Okoli, O.I. and Liang, Z., "Resin Infusion between Double Flexible Tooling, Evaluation of Process Parameters," 35th International SAMPE Technical Conference, 2003.

[28] Thagard, J.R., Liu, Q., Liang, Z., Okoli, O.I. and Wang, H.P., "Simulation of the Resin Infusion Between Double Flexible Tooling Process and Experimental Validation," AmeriPAM Conference, 2003.

[29] Thagard, J.R., Okoli, O.I., Liang, Z., Wang, H.P. and Zhang, C., "Resin infusion between double flexible tooling: prototype development," *Composites Part A*, 2003.

[30] Thagard, J.R., Okoli, O.I. and Liang, Z., "Resin Infusion between Double Flexible Tooling, Evaluation of Process Parameters," accepted JRPC, October, 2003.

BIOGRAPHICAL SKETCH

The author is a doctoral student in Industrial Engineering and expecting graduation in December, 2003. He started his graduate work in the Spring of 1996 at the University of Houston, Department of Industrial Engineering before transferring to Florida State University. His main research area is in the field of Composites Engineering.

The author was born November, 1970, to Dr. and Mrs. Norman Thagard. He attended elementary through high school in Friendswood, Texas. He received an Associates of Arts degree from Austin Community College Spring of 1993, a Bachelor's of Science in Industrial Engineering from the University of Houston Fall of 1995 and received his Masters of Science in Industrial & Manufacturing Engineering from Florida State University Fall of 2001. He is married to his wife, Amy, and had his first child, Kaylee, in October, 2000 and his second child, Ethan, in July, 2003.